Radiative B Meson Decays into $K\pi\gamma$ and $K\pi\pi\gamma$ Final States

Dissertation

Department of Physics, Faculty of Science,
Kyoto University

by

Shohei NISHIDA

January 2003

Abstract

The flavor changing neutral current process $b \to s\gamma$ is a sensitive probe to search for physics beyond the Standard Model (SM). In order to measure the inclusive $b \to s\gamma$ branching fraction more precisely, a detailed knowledge of the exclusive final states is required. In addition to the already established $B \to K^*(892)\gamma$ decay, there are several known resonances that can contribute to the final states. These resonant decays can also be used to measure the photon helicity in order to explore some non-SM models, which are not accessible by the measurement of the inclusive rate only.

In this dissertation, a study of radiative B meson decays into the $K^+\pi^-\gamma$ and $K^+\pi^-\pi^+\gamma$ final states is reported. For the $K^+\pi^-\gamma$ final states, signal around $K\pi$ invariant mass $M_{K\pi} = 1.4$ GeV/c^2 is decomposed to $B^0 \to K_2^*(1430)^0\gamma$, $B^0 \to K^*(1410)^0\gamma$ and non-resonant components using an unbinned maximum likelihood fit to M_{bc}, $M_{K\pi}$ and the helicity angle. We find evidence for decays via an intermediate tensor meson state with a branching fraction of

$$\mathcal{B}(B^0 \to K_2^*(1430)^0\gamma) = (1.33 \, {}^{+\,0.48}_{-\,0.45}(\text{stat.}) \, {}^{+\,0.09}_{-\,0.11}(\text{syst.})) \times 10^{-5}.$$

For $B^+ \to K^+\pi^-\pi^+\gamma$, we report the first observation of the mode with the branching fraction of

$$\mathcal{B}(B^+ \to K^+\pi^-\pi^+\gamma) = (2.41 \, {}^{+\,0.50}_{-\,0.47}(\text{stat.}) \, {}^{+\,0.40}_{-\,0.30}(\text{syst.})) \times 10^{-5}.$$

From the $M_{K\pi}$ and $M_{\pi\pi}$ distributions, we find that the $B^+ \to K^{*0}\pi^+\gamma$ and $B^+ \to K^+\rho^0\gamma$ channels dominate in the decay with the $K^+\pi^-\pi^+\gamma$ final states.

The analysis is based on a dataset of 29.4 fb^{-1} recorded by the Belle experiment at the KEKB collider.

Acknowledgement

Contents

List of Figures

List of Tables

Chapter 1

Introduction

The Standard Model (SM) describes the world of the elementary particles. The fundamental particles are spin-1/2 fermions, and the interactions between fermions, which are mediated by spin-1 bosons, are described by a Gauge field theory. The basic fermions are leptons and quarks, and they are classified as listed in Table 1.1. There are three generations of fermions, and each generation has the same feature except for the mass.

Table 1.1: Quarks and leptons.

	Charge	1st generation	2nd generation	3rd generation
Quark	+2/3	u (up)	c (charm)	t (top)
	−1/3	d (down)	s (strange)	b (bottom)
Lepton	0	ν_e (e neutrino)	ν_μ (μ neutrino)	ν_τ (τ neutrino)
	−1	e (electron)	μ (muon)	τ (tau)

The SM treats three kind of interactions between fermions: strong, electromagnetic and weak interactions.[1] Both leptons and quarks interact through the weak interaction which is described as a SU(2) group, and left-handed states of fermions form the SU(2) doublets. On the other hand, only quarks interact through the strong interaction which is described as a SU(3) group. Fermions except neutrinos interact through the U(1) electromagnetic interaction. The SU(2)×U(1) group is spontaneously broken by the Higgs mechanism, resulting in the scalar Higgs boson. It makes W and Z, mediators of the weak interaction, massive, while the mediator of the electroweak interaction γ remains massless. Fermions, which are originally massless under the Gauge theory, also acquire their mass terms, although the fermion masses are left as free parameters.

All the particles except the Higgs boson have been already discovered by experiments. So far, the SM successfully explains the phenomena observed in experiments. However, we also know the SM is not the ultimate theory. One problem of the SM is known as the hierarchy problem. The 1-loop radiative correction of the scaler Higgs mass m_H is quadratically divergent, and it becomes some 15 order of magnitude larger than m_H, although m_H is expected to be in the same order of the W mass. To renormalize this divergence, we need a "fine-tuning" to cancel the correction leaving an electroweak scale mass, which seems unnatural. Therefore, it is considered that a more fundamental theory beyond the SM exists in a higher energy scale.

One way to access the physics beyond the SM experimentally is to study rare decays that are inhibited or suppressed in the SM but may be enhanced in the non-SM physics. Radiative

---

[1] Gravity, the other familiar interaction, is not included in the SM, because there is no successful theory of quantum gravity. The mediator of the gravity is expected to be massless spin-2 boson called graviton.
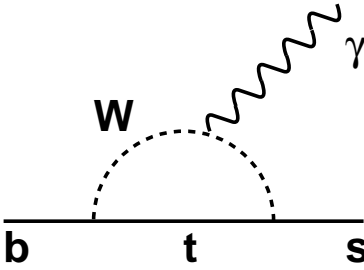
Figure 1.1: Electroweak penguin diagram for the $b \to s\gamma$ process.

B decay, which mainly proceeds through the $b \to s\gamma$ process, is a good candidate for it. This process is a flavor changing neutral current (FCNC) process, and the lowest order diagram in the SM is an one-loop electroweak penguin diagram (Fig. 1.1). Non-SM particles may contribute to the loop and change the inclusive branching fraction of $B \to X_s\gamma$ from that predicted in the SM, where X_s is a hadronic recoil system including an s quark. So far, measurements of the inclusive branching fraction give consistent results with the SM prediction at 10% level. To improve the inclusive measurement, detail knowledge of the final states of $B \to X_s\gamma$ is important.

Another possible contribution of New Physics to the $b \to s\gamma$ process may be seen in the photon helicity. The helicity of photons from $b \to s\gamma$ is left-handed in the SM, but some non-SM models allow right-handed photons. Several methods to measure the photon helicity using radiative B decays through higher kaonic resonances such as $B \to K_1(1400)\gamma$ are proposed [2].

In this dissertation, a study of radiative B decays to $K\pi\gamma$ and $K\pi\pi\gamma$ final states at the Belle experiment is presented. An introduction of the radiative B decays is described in Chapter 2. An overview of the Belle experiment is given in Chapter 3. In Chapter 4, we describe the technique for signal reconstruction and background suppression. Chapter 5 and 6 discuss the analysis of $B^0 \to K^+\pi^-\gamma$ and $B^+ \to K^+\pi^-\pi^+\gamma$, respectively. Finally, we conclude in Chapter 7.

Charge conjugates are implied throughout the dissertation. $K^*(892)$ is often denoted by K^*. In the case that values have two errors, the first and second errors are statistical and systematic, respectively.

Chapter 2

Radiative B Decays into Resonances

We have studied radiative B decays to $K\pi\gamma$ and $K\pi\pi\gamma$ final states, motivated by the following facts.

- Understanding of the final states of the $b \to s\gamma$ process is important for the precise measurement of the inclusive $b \to s\gamma$ branching fraction.

- Measurement of the branching fraction of radiative B decays through higher kaonic resonances tests the models of the theoretical predictions.

- Radiative B decays to the $K\pi\pi\gamma$ final states can be a powerful tool in search for the physics beyond the SM.

2.1 Branching fraction of the inclusive $B \to X_s\gamma$ decay

The theoretical calculation of the inclusive branching fraction of the $b \to s\gamma$ process starts from the low-energy effective Hamiltonian [3]

$$\mathcal{H}^{\text{eff}} = -\frac{4G_F}{\sqrt{2}}|V_{ts}^* V_{tb}| \sum_{i=1}^{8} C_i(\mu)O_i(\mu), \tag{2.1}$$

where G_F is the Fermi coupling constant, and V_{ts} and V_{tb} are Cabibbo-Kobayashi-Maskawa (CKM) matrix elements (Appendix A), $O_i(\mu)$ and $C_i(\mu)$ are local operators and Wilson coefficients, respectively, at the renormalization scale μ that is chosen to be the order of the b quark mass m_b. The amplitude that B meson decays to the final state F can be written as

$$A(B \to F) = \langle F|\mathcal{H}^{\text{eff}}|B\rangle = -\frac{4G_F}{\sqrt{2}}|V_{ts}^* V_{tb}| \sum_{i=1}^{8} C_i(\mu)\langle F|O_i(\mu)|B\rangle. \tag{2.2}$$

Operators relevant to the calculation of $B \to X_s\gamma$ are

$$O_2 = \bar{s}_L\gamma_\mu c_L \bar{c}_L\gamma^\mu b_L, \quad O_7 = \frac{em_b}{16\pi^2}\bar{s}_L\sigma_{\mu\nu}F^{\mu\nu}b_R, \quad O_8 = \frac{g_s m_b}{16\pi^2}\bar{s}_L\sigma_{\mu\nu}G_a^{\mu\nu}t_a b_R, \tag{2.3}$$

where e and g_s are the electromagnetic (EM) and strong coupling constant, respectively, $F^{\mu\nu}$ and $G_a^{\mu\nu}$ are the EM and QCD field strength tensor, and t_a is a color SU(3) generator. The other operators can be neglected.

The decay rate of the $b \to s\gamma$ process is calculated by taking the ratio of the semi-leptonic decay to eliminate strong dependence of m_b:

$$\mathcal{B}(B \to X_s\gamma) = \frac{\Gamma(B \to X_s\gamma)}{\Gamma(B \to X_c e\bar{\nu})} \mathcal{B}(B \to X_c e\bar{\nu}) \tag{2.4}$$

$$= R_{\text{quark}} \mathcal{B}(B \to X_c e\bar{\nu}). \tag{2.5}$$

$\mathcal{B}(B \to X_c e\bar{\nu})$ was measured by ARGUS [4] and CLEO [5], and is averaged to be $(10.2 \pm 0.4)\%$ by PDG [6]. Recently, Belle also obtained a consistent result of $\mathcal{B}(B \to X_c e\bar{\nu}) = (10.90 \pm 0.12 \pm 0.49)\%$ [7].

In the leading order (LO) calculation, R_{quark} is calculated to be

$$R_{\text{quark}} = \frac{6\alpha}{\pi f(z)} \left| \frac{V_{ts}^* V_{tb}}{V_{tc}} \right|^2 |C_7^{(0)\text{eff}}(\mu)|^2. \tag{2.6}$$

Here, $f(z) = 1 - 8z - 8z^3 - z^4 - 12z^2 \ln z$ is the phase space factor with $z = (m_c/m_b)^2$, where m_c is the c quark mass. $C_7^{(0)\text{eff}}(\mu)$ is an effective Wilson coefficient at the renormalization scale $(\mu \sim m_b)$, and can be written as

$$C_7^{(0)\text{eff}}(\mu) = 0.695 C_7^{(0)}(M_W) + 0.085 C_8^{(0)}(M_W) - 0.158 C_2^{(0)}(M_W). \tag{2.7}$$

In the LO, the inclusive $B \to X_s\gamma$ rate is calculated to be $(2.8 \pm 0.8) \times 10^{-4}$ [8], where a large part of the error comes from the choice of μ.

The next-to-leading order (NLO) calculation becomes complicated because it contains the correction to the semi-leptonic decays, the Wilson coefficient and the strong coupling constants. Recent calculation shows [9]

$$\mathcal{B}(B \to X_s\gamma) = (3.57 \pm 0.30) \times 10^{-4}. \tag{2.8}$$

As for the experiment, the $b \to s\gamma$ inclusive branching fraction is measured by CLEO [10], ALEPH [11] and Belle [12] to be

$$\mathcal{B}(B \to X_s\gamma) = (3.21 \pm 0.43 \pm 0.27^{+0.18}_{-0.10}) \times 10^{-4} \qquad \text{(CLEO)}, \tag{2.9}$$

$$= (3.11 \pm 0.80 \pm 0.72) \times 10^{-4} \qquad \text{(ALEPH)}, \tag{2.10}$$

$$= (3.36 \pm 0.53 \pm 0.42^{+0.50}_{-0.42}) \times 10^{-4} \qquad \text{(Belle)}, \tag{2.11}$$

where the third error represents an error from the theory. These results give the present world average of

$$\mathcal{B}(B \to X_s\gamma) = (3.22 \pm 0.40) \times 10^{-4}. \tag{2.12}$$

This is slightly lower than the prediction, but is consistent within errors. Therefore, the measurements make a constraint to non-SM models. To search for a signal of New Physics, both experimental measurements and theoretical predictions must be more precise.

In the experiment at $\Upsilon(4S)$, there are two methods of the analysis, fully inclusive analysis and pseudo-reconstruction analysis, although we cannot distinguish them clearly. In the fully inclusive analysis, we select the high energy photon without reconstructing the hadronic recoil system X_s. This method is relatively independent of the model of the $b \to s\gamma$ decay. However, due to large background from $q\bar{q}$, we subtract the photon energy spectrum for the off-resonance data from that for the on-resonance data, and obtain the photon energy spectrum for the $b \to s\gamma$. So, we need large data sample both for on-resonance and off-resonance data. We also need very reliable Monte Carlo (MC) to describe $B\bar{B}$ decays. Therefore, at least in the Belle experiment, where we have only small amount of off-resonance data compared with the on-resonance data,

Table 2.1: Measured branching fractions of $B \to K^*(892)\gamma$ ($\times 10^{-5}$).

Experiment	$\mathcal{B}(B^0 \to K^*(892)^0\gamma)$	$\mathcal{B}(B^+ \to K^*(892)^+\gamma)$	Ref.
CLEO	$4.55\,^{+\,0.72}_{-\,0.68} \pm 0.34$	$3.76\,^{+\,0.89}_{-\,0.83} \pm 0.28$	[15]
BaBar	$4.23 \pm 0.40 \pm 0.22$	$3.83 \pm 0.62 \pm 0.22$	[16]
Belle	$4.96 \pm 0.67 \pm 0.45$	$3.89 \pm 0.93 \pm 0.41$	[17]

the fully inclusive analysis is not so efficient to measure the inclusive $B \to X_s\gamma$ branching fraction more precisely.

In the pseudo-reconstruction analysis, we reconstruct B mesons from a high energy photon and an X_s system formed from a kaon (K^+ or K^0_S) with pions. This method is powerful to suppress the $q\bar{q}$ background, but introduces some model dependences. We make a selection on the invariant mass of the X_s system (M_{X_s}), and we need a model of the M_{X_s} distribution to estimate the signal efficiency. In addition, since we can reconstruct only some specific modes, we need a model of the hadronization process to estimate the fraction of the X_s system that we reconstruct. So far, most of the model dependence comes from the first one, but it can be reduced by relaxing the M_{X_s} selection. Hence, we have to think about reducing the latter model dependence as far as we rely on the pseudo-reconstruction analysis.[1]

We usually rely on MC such as JETSET [13] to describe the hadronization process, but the $b \to s\gamma$ decays through resonances such as $B \to K^*(892)\gamma$ or $B \to K^*_2(1430)\gamma$ are not taken into account. Compared with the well-established $B \to K^*(892)\gamma$ decay, other resonant decays are not well known. This is one of the motivations of the study for the resonant decays.

2.2 Radiative B decays through kaonic resonances

The first evidence of radiative B decays was found by the CLEO collaboration in 1993 in the $B \to K^*(892)\gamma$ decay mode [14]. The present experimental results of the branching fractions are listed in Table 2.1. From the measured branching fraction (Eq. (2.12)), we know that around 13% of the $b \to s\gamma$ process can be explained by the $B \to K^*(892)\gamma$ decay.

A part of the rest of the $b \to s\gamma$ decays are expected to be radiative B decays through higher kaonic resonances. CLEO found evidence of $B \to K^*_2(1430)\gamma$ [15] with the branching fraction of

$$\mathcal{B}(B \to K^*_2(1430)\gamma) = (1.66\,^{+\,0.59}_{-\,0.53} \pm 0.13) \times 10^{-5}, \tag{2.13}$$

neglecting possible contributions from $B \to K^*(1410)\gamma$ and non-resonant $B \to K\pi\gamma$. Hereafter, higher kaonic resonances are denoted by K_X in this dissertation. Well-known kaonic resonances are listed in Table 2.2. Since most resonances mainly decay to $K\pi$, $K^*\pi$ and $K\rho$, we use the $K\pi\gamma$ and $K\pi\pi\gamma$ final states for the study of $B \to K_X\gamma$ decays.

The estimation of the form factor $\langle K_X | \mathcal{O}_7 | B \rangle$ is essential in the prediction of the branching fraction of $B \to K_X\gamma$ decays. The prediction was first performed by Altomari [18] and later by Ali, Ohl and Mannel [19] and Veseli and Olsson [20]. Their form factor calculations were based on the non-relativistic quark model assuming both initial b and final s quarks are heavy. Recently, Ebert et al. [21] calculated the form factor with the relativistic quark model. Other predictions are also available [22, 23]. The predicted branching fractions are listed in Table 2.3. Measurements of the branching fractions of $B \to K_X\gamma$ provides a test for these theoretical models.

---

[1]In the fully inclusive analysis by CLEO [10], the information from the pseudo-reconstruction technique is used to reduce the $q\bar{q}$ background. In such a case, better understanding of the hadronization process also helps the precise measurement of the inclusive branching fraction of $B \to X_s\gamma$.

Table 2.2: List of kaonic resonances [6]. Mass (M), width (Γ), sub-decay modes and branching fractions are listed.

Resonance	J^P	M [MeV/c^2]	Γ [MeV/c^2]	Sub-decay modes and branching fractions
$K^*(892)^+$	1^-	891.66 ± 0.26	50.8 ± 0.9	$K\pi$ [$\sim$100%]
$K^*(892)^0$		896.10 ± 0.27	50.7 ± 0.6	
$K_1(1270)$	1^+	1273 ± 7	90 ± 20	$K\rho$ [42%], $K_0^*(1430)\pi$ [28%], $K^*(892)\pi$ [16%]
$K_1(1400)$	1^+	1402 ± 7	174 ± 13	$K^*(892)\pi$ [94%], $K\rho$ [3%], $Kf_0(1370)$ [2%]
$K^*(1410)$	1^-	1410 ± 15	232 ± 21	$K^*(892)\pi$ [>40%], $K\pi$ [6.6%]
$K_0^*(1430)$	0^+	1412 ± 6	294 ± 23	$K\pi$ [93%]
$K_2^*(1430)^+$	2^+	1425.6 ± 1.5	98.5 ± 2.7	$K\pi$ [49.9%], $K^*(892)\pi$ [24.7%], $K^*(892)\pi\pi$ [13.4%], $K\rho$ [8.7%], $K\omega$ [2.9%]
$K_2^*(1430)^0$		1432.4 ± 1.3	109 ± 5	
$K_2(1580)$	2^-	—	—	$K^*(892)\pi$
$K_1(1650)$	1^+	1650 ± 50	150 ± 50	$K\pi\pi$, $K\phi$
$K^*(1680)$	1^-	1717 ± 27	322 ± 110	$K\pi$ [38.7%], $K\rho$ [31.4%], $K^*(892)\pi$[29.9%]
$K_2(1770)$	2^-	1773 ± 8	186 ± 14	$K_2^*(1430)\pi$
$K_3^*(1780)$	3^-	1776 ± 7	159 ± 21	$K\rho$ [31%], $K^*(892)\pi$ [20%], $K\pi$ [18.8%]
$K_2(1820)$	2^-	1816 ± 13	276 ± 35	$K_2^*(1430)\pi$, $K^*(892)\pi$, $Kf_2(1270)$, $K\omega$
$K_4^*(2045)$	4^+	2045 ± 9	198 ± 30	$K\pi$ [9.9%], $K^*\pi\pi$ [9%], $K^*\pi\pi\pi$ [7%]

Table 2.3: Predictions for branching fractions of radiative B decays through higher kaonic resonances ($\times 10^{-5}$).

decay mode	Ali-Ohl-Mannel [19]	Veseli-Olsson [20]	Ebert *et al.* [21]
$B \to K^*(892)\gamma$	$1.4 - 4.9$	4.71 ± 1.79	4.5 ± 1.5
$B \to K_1(1270)\gamma$	$1.8 - 4.0$	1.20 ± 0.44	0.45 ± 0.15
$B \to K_1(1400)\gamma$	$2.4 - 5.2$	0.58 ± 0.26	0.78 ± 0.18
$B \to K^*(1410)\gamma$	$2.9 - 4.2$	1.14 ± 0.18	—
$B \to K_2^*(1430)\gamma$	$6.9 - 14.8$	1.73 ± 0.80	1.7 ± 0.6
$B \to K_2(1580)\gamma$	$1.8 - 2.6$	0.46 ± 0.11	—
$B \to K_1(1650)\gamma$	—	0.47 ± 0.16	—
$B \to K^*(1680)\gamma$	$0.4 - 0.6$	0.15 ± 0.04	—
total	$17.6 - 36.4$	10.44 ± 3.78	7.43 ± 2.43

As for the experimental status, there are no evidence for $B \to K_X\gamma$ decays except $B \to K^*(892)\gamma$ and $B \to K_2^*(1430)\gamma$. Present upper limits are set by ARGUS [24, 25] and CLEO [15], as listed in Table 2.4.

2.3 $B \to K_X\gamma$ as a probe to New Physics

In the SM, the s quark in the $b \to s\gamma$ process has the left chirality, because it couples to a W boson as shown in Fig. 1.1. So, the photon emitted in $b \to s\gamma$ is left-handed in the approximation that the s quark mass m_s is negligible. Namely, in radiative B decays, the photon from $\bar{B}^0$ or B^- is almost left-handed, while that from B^0 or B^+ is almost right-handed. However, in some models beyond the SM such as the left-right symmetric model and the unconstraint Minimal Supersymmetric Standard Model, the contribution of right-handed photons can be comparable to

Table 2.4: Experimental upper limits of radiative B decays through higher kaonic resonances. The upper limits for neutral $B^0 \to K_X^0 \gamma$ and charged $B^+ \to K_X^+ \gamma$ are measured by ARGUS [25] assuming $\mathcal{B}(\Upsilon(4S) \to B^0 \bar{B}^0) = 0.45$ and $\mathcal{B}(\Upsilon(4S) \to B^+ B^-) = 0.55$. The numbers shown here are rescaled by PDG [6] with $\mathcal{B}(\Upsilon(4S) \to B^0 \bar{B}^0) = 0.5$.

decay mode	neutral $B^0 \to K_X^0 \gamma$	charged $B^+ \to K_X^+ \gamma$	B^0/B^+ admixture
$B \to K_1(1270)\gamma$	7.0×10^{-3}	7.3×10^{-3}	—
$B \to K_1(1400)\gamma$	4.3×10^{-3}	2.2×10^{-3}	4.1×10^{-4} [24]†
$B \to K^*(1410)\gamma$	—	—	12.7×10^{-5} [15]
$B \to K^*(1680)\gamma$	2.0×10^{-3}	1.9×10^{-3}	—
$B \to K_3^*(1780)\gamma$	1.0×10^{-2}	5.5×10^{-3}	3.0×10^{-3} [24]

$\dagger$ The upper limit given in PDG2002 [6] is wrong. It will be fixed in PDG2003.

left-handed photons without changing the inclusive branching fraction or without producing an asymmetry between B^0 (B^+) and $\bar{B}^0$ (B^-). Therefore, measurements of the photon helicity are sensitive to some non-SM models which are not accessible by the measurement of the branching fraction or the asymmetry in the $b \to s\gamma$ decays.

Several methods have been proposed to measure the photon helicity. The method by Atwood, Gronau and Soni is to search for the mixing-induced CP asymmetry in radiative B decays [26]. The method by Gronau and Pirjol is to form a parity-odd variable in the recoil system in the $B \to K\pi\pi\gamma$ final states [2]. In both methods, radiative B decays through kaonic resonances play an important role.[2]

The mixing-induced CP asymmetry in the B^0-$\bar{B}^0$ system arises when B^0 and $\bar{B}^0$ decays to a common CP eigenstate such as $J/\psi K_S^0$. We can consider the CP asymmetry in the same way for radiative B decays $B \to M^0 \gamma$, where M^0 is either K^{*0} ($\to K_S^0 \pi^0$) or $K_1(1270)^0$ ($\to K_S^0 \rho^0$). However, photons in $B^0 \to M^0 \gamma$ are right-handed, while photons in $\bar{B}^0 \to M^0 \gamma$ are left-handed. This means that B^0 and $\bar{B}^0$ do not decay into the same final state, hence the CP asymmetry does not arise. More exactly, the ratio of right-handed photons in $b \to s\gamma$ decays is order of m_s/m_b in the SM, and the time-dependent CP asymmetry in $B^0 \to M^0 \gamma$ is

$$A(t) \simeq \frac{2m_s}{m_b} \sin(2\phi_1) \sin(\Delta m \Delta t), \tag{2.14}$$

where ϕ_1 is one of the angles of the unitary triangle (Appendix. A), Δm is the mass difference of two mass eigenstates of B^0 and $\bar{B}^0$ system, and Δt is the difference of the decay times of B^0 and $\bar{B}^0$.

On the other hand, if right-handed photons are comparable to left-handed photons in $b \to s\gamma$, both B^0 and $\bar{B}^0$ decay into the same final state. Then, large CP asymmetry can occur. In the left-right symmetric model, the asymmetry can be as large as

$$A(t) \simeq 0.67 \cos(2\phi_1) \sin(\Delta m \Delta t). \tag{2.15}$$

Therefore, a large CP asymmetry in the radiative B decays is a signature of New Physics which allows right-handed photons in $b \to s\gamma$. This is the idea of the former method by Atwood, Gronau and Soni. Experimentally, it is very difficult to determine the vertex of the $K_S^0 \pi^0 \gamma$ final state, so the measurement of the mixing-induced asymmetry in $B^0 \to K^{*0}\gamma$ seems hopeless.

---

[2] Another method is to study an angular distributions in $B \to K^*(\to K\pi)\gamma(\to e^+ e^-)$, where the photon may be virtual [27] or real (conversion to an electron-positron pair) [28].

The measurement may be possible for $B^0 \to K_1(1270)^0\gamma$, where $K_1(1270)^0$ decays to $K_S^0\rho^0$ ($\rho^0 \to \pi^+\pi^-$).

The latter method by Gronau and Pirjol utilizes the decay $B \to K_1(1400)\gamma$ in which $K_1(1400)$ decays through the decay chain

$$K_1(1400)^0 \to \begin{Bmatrix} K^{*+}\pi^- \\ K^{*0}\pi^0 \\ \rho^- K^+ \end{Bmatrix} \to K^+\pi^-\pi^0, \qquad K_1(1400)^+ \to \begin{Bmatrix} K^{*+}\pi^0 \\ K^{*0}\pi^+ \\ \rho^+ K^0 \end{Bmatrix} \to K^0\pi^+\pi^0 \qquad (2.16)$$

in order to measure the photon helicity. The photon helicity is odd under parity. Because we measure only the momenta of photons and decay products of the kaonic resonance, we cannot form a parity-odd variable from them if the resonance decays into two bodies. In the case the resonance decays into three bodies, we can define a parity-odd variable like $\vec{p}_\gamma \cdot (\vec{p}_1 \times \vec{p}_2)$ from the decay products, where $\vec{p}_\gamma$, $\vec{p}_1$, $\vec{p}_2$ are the momenta of γ and two pions, respectively. Indeed, to access the photon helicity information, a variable $\cos\tilde{\theta}$ calculated in the $K_1(1400)$ rest frame is defined as

$$\cos\tilde{\theta} = -\,\mathrm{sgn}(s_{13} - s_{23})\frac{\vec{p}_\gamma \cdot (\vec{p}_1 \times \vec{p}_2)}{|\vec{p}_\gamma||\vec{p}_1 \times \vec{p}_2|}, \qquad (2.17)$$

where s_{13} (s_{23}) is the invariant mass of K and π^- (π^0) system. Then, the decay follows

$$\frac{d\Gamma}{d\cos\tilde{\theta}} \propto 1 + \cos^2\tilde{\theta} + 4\lambda_\gamma R_1 \cos\tilde{\theta}, \qquad (2.18)$$

where λ_γ is the photon helicity and R_1 is a parameter which depends on the fraction and relative phase of D-wave and S-wave in $K_1(1400)$ and is calculated to be $R_1 = 0.22\pm0.03$. By integrating the equation in the region $\cos\tilde{\theta} > 0$ and $\cos\tilde{\theta} < 0$, we obtain a formula on an up-down asymmetry A_{UD},

$$A_{\mathrm{UD}} \equiv \frac{N(\cos\tilde{\theta} > 0) - N(\cos\tilde{\theta} < 0)}{N(\cos\tilde{\theta} > 0) + N(\cos\tilde{\theta} < 0)} = \frac{3}{2}R_1\lambda_\gamma. \qquad (2.19)$$

We can measure the photon helicity by measuring A_{UD}.

However, the situation is more complicated if we consider other kaonic resonances. In the mass region $1.3~\mathrm{GeV}/c^2 < M_{K\pi\pi} < 1.5~\mathrm{GeV}/c^2$, not only $K_1(1400)$ but $K^*(1410)$ and $K_2^*(1430)$ contribute. In principle, the photon helicity can be still obtained if the amplitudes of $B \to K_1(1400)\gamma$, $B \to K^*(1410)\gamma$ and $B \to K_2^*(1430)\gamma$ are known, although complete extraction of the photon helicity may not be easy in the experimental view. Nevertheless, the measurement of A_{UD} may still be helpful, because an asymmetry should be observed unless the $B \to K_1(1400)\gamma$ decay is very small.

These measurements require more B mesons than those provided by the Belle experiment in a few years, and should be studied in higher luminosity B factories. To estimate the feasibility of these methods, we need to know the resonant structures of $B \to K_X\gamma$ decays. The final states necessary to these methods are $K_S^0\pi^+\pi^-\gamma$ and $K^+\pi^-\pi^0\gamma$, but, as a first step, we search for the $B^+ \to K^+\pi^-\pi^+\gamma$ decay in this study.

Chapter 3

The Belle Experiment

3.1 Overview of the Belle experiment

Since the first observation of the CP violation in the K^0 system in 1964 [29], a large amount of theoretical works have been pursued to understand the phenomenon. According to a model proposed by Kobayashi and Maskawa in 1973 [30], which we now consider to be valid, a complex phase that remains in the quark-mixing matrix can violate the CP symmetry within the framework of the SM, if quarks have three generations. The matrix is now called Cabibbo-Kobayashi-Maskawa (CKM) matrix. Measurement of the matrix elements is essential to the understanding of the CP violation.

In 1980, Carter, Bigi and Sanda pointed out the possibility of sizable CP violation in the certain modes of B decays [31]. Among these, the most promising decay mode is the $B^0(\bar{B}^0) \to J/\psi K_S^0$, which allows us to measure the angle ϕ_1 of the unitarity triangle (Appendix A). The time dependent asymmetry of the decay can be expressed as

$$A(\Delta t) = \frac{\Gamma(B^0 \to J/\psi K_S^0; \Delta t) - \Gamma(\bar{B}^0 \to J/\psi K_S^0; \Delta t)}{\Gamma(B^0 \to J/\psi K_S^0; \Delta t) + \Gamma(\bar{B}^0 \to J/\psi K_S^0; \Delta t)} = \sin 2\phi_1 \sin(\Delta m \Delta t). \qquad (3.1)$$

where Δm is the mass difference of two mass eigenstates of B^0 and $\bar{B}^0$ system, and Δt is the difference of the decay time for the B^0 and $\bar{B}^0$ decays.

So as to observe the CP violation in B decays, to determine the CKM matrix elements and to study various B physics, the Belle experiment started at KEK (High Energy Accelerator Research Organization)[1] in 1994. The experimental apparatus consists of the KEKB [32, 33] collider and the Belle detector [34–36]. KEKB is an asymmetric energy e^+e^- collider with $E_- = 8$ GeV and $E_+ = 3.5$ GeV, where E_+ and E_- is the energy of electron and positron beams, respectively. The center-of-mass (CM) energy $\sqrt{s}$ is

$$\sqrt{s} = \sqrt{4E_-E_+} = 10.58 \text{ GeV}, \qquad (3.2)$$

which is equal to the mass of $\Upsilon(4S)$, which mainly decays to $B^0\bar{B}^0$ or B^+B^-. Since the energy is asymmetric, the B meson pairs are created with a Lorentz boost factor of

$$\beta\gamma = \frac{E_- - E_+}{\sqrt{s}} = 0.425. \qquad (3.3)$$

Because B meson pairs are produced almost at rest in the $\Upsilon(4S)$ rest frame, Δt of Eq. (3.1) can be determined by measuring the distance of the decay vertices (Δz) of the two B mesons from the relation $\Delta z \simeq c\beta\gamma\Delta t$. The average flight length of B mesons is about 200 μm.

---

[1]Tsukuba-city, Japan.

Table 3.1: *B*-factories in the world. The starting year of CESR listed here is the year CLEO II is installed.

Institute	Accelerator	Type	Detector	Year
Cornell	CESR	e^+e^- sym.	CLEO II,III [37]	1995 – 2001
SLAC	PEP-II	e^+e^- asym.	BABAR [38]	1999 –
KEK	KEK-B	e^+e^- asym.	Belle [39]	1999 –
DESY	HERA	fixed (p + wire)	HERA-B [40]	2000 –
FNAL	Tevatron	$p\bar{p}$	BTeV [41]	2007 –
CERN	LHC	pp	LHCb [42]	2007 –

Table 3.2: Masses and widths of Υ mesons [6].

Meson	Mass (MeV/c^2)	Total width (MeV/c^2)
$\Upsilon(1S)$	9460.30 ± 0.26	0.0525 ± 0.0018
$\Upsilon(2S)$	10023.26 ± 0.31	0.044 ± 0.007
$\Upsilon(3S)$	10355.2 ± 0.5	0.0263 ± 0.0035
$\Upsilon(4S)$ or $\Upsilon(10580)$	10580.0 ± 3.5	14 ± 5
$\Upsilon(10865)$ [$\Upsilon(5S)$]	10865 ± 8	110 ± 13
$\Upsilon(11020)$ [$\Upsilon(6S)$]	11019 ± 8	79 ± 16

Since the branching fractions of the B decays which are useful for the study of the *CP* violation are small ($\lesssim 10^{-4}$), around 10^8 of B mesons are necessary. The design luminosity of KEKB is 1×10^{34} cm^{-2}s^{-1}, which corresponds to 10^8 B mesons per year. Owing to the enormous number of B mesons to be produced, KEKB is often called a B-factory.

Table 3.1 lists the B-factory experiments in the world. CESR is a symmetric e^+e^- collider, which made a large contribution to the B physics over twenty years, but completed the operation at $\Upsilon(4S)$ in June 2001. The BABAR experiment with an asymmetric e^+e^- collider PEP-II, is the good competitor of the Belle experiment. BTeV and LHCb are future experiments at hadron colliders, which can produce a far larger number of B mesons including B_s and other higher B mesons.

3.2 $\Upsilon(4S)$

The Υ mesons are bound states of $b\bar{b}$ with $J^{PC} = 1^{--}$. After the first observation of $\Upsilon(1S)$ in the proton-nucleus collision by the CFS collaboration in 1977 [43], Υ mesons were confirmed by experiments at CESR and DORIS.[2] Figure 3.1 shows the total e^+e^- annihilation cross section as a function of the CM energy in the region of Υ resonances measured by CLEO. The masses and widths of the resonances are listed in Table 3.2. The widths for the three lighter resonances are very small owing to the OZI (Okubo-Zweig-Iizuka) suppression of hadronic decays.

The mass of $\Upsilon(4S)$ is just above the threshold of $B\bar{B}$ production. The width of $\Upsilon(4S)$ is far larger than $\Upsilon(1S)$, $\Upsilon(2S)$ and $\Upsilon(3S)$. The cross section of the $\Upsilon(4S)$ production at the $\Upsilon(4S)$ peak position is about 1/3 of that of $q\bar{q}$ ($q = u$, d, s, c) production, which is often referred as "continuum". So, although KEKB is operated at the $\Upsilon(4S)$ resonance to produce $B\bar{B}$ pairs, it produces three times more $q\bar{q}$ events that contribute as background to the B physics. In order

---

[2]An e^+e^- collider at DESY.
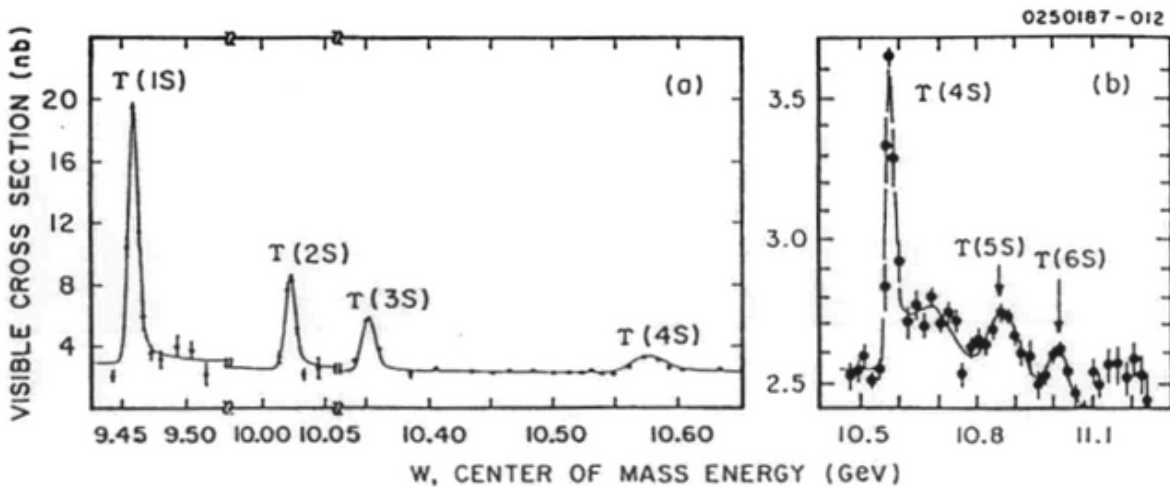
Figure 3.1: e^+e^- total cross section measured by CLEO. The energy regions (a) $\Upsilon(1S)$ through $\Upsilon(4S)$ (b) $\Upsilon(4S)$ through $\Upsilon(6S)$ are shown. Widths of $\Upsilon(1S)$, $\Upsilon(2S)$ and $\Upsilon(3S)$ are dominated by the beam energy resolution. A small bump between $\Upsilon(4S)$ and $\Upsilon(5S)$ is not clarified.

to study the $q\bar{q}$ contribution, KEKB is also operated at 60 MeV below the $\Upsilon(4S)$ resonance.[3] The operations at the $\Upsilon(4S)$ resonance and 60 MeV below are referred as "on-resonance" and "off-resonance", respectively. Around 10% of data taken by Belle are off-resonance data.

The branching fraction of $\Upsilon(4S)$ to $B\bar{B}$ pairs is more than 96% according to a measurement by CLEO [5], and no other decay channel of $\Upsilon(4S)$ is known. The ratio of the branching fraction of $\Upsilon(4S)$ to $B^0\bar{B}^0$ and B^+B^- has also been measured by CLEO [44] to be

$$\frac{\mathcal{B}(\Upsilon(4S) \to B^+B^-)}{\mathcal{B}(\Upsilon(4S) \to B^0\bar{B}^0)} = 1.04 \pm 0.07 \pm 0.04, \tag{3.4}$$

which is consistent with equal production rate for charged and neutral pairs. In this study, we follow the PDG convention which assumes an equal production rate for $B^0\bar{B}^0$ and B^+B^- at $\Upsilon(4S)$ [6].

3.3 History of the Belle experiment

The construction of KEKB and Belle was completed in 1998. After a half year of KEKB commissioning, the Belle detector was installed onto the beam line in May 1999. The physics run started in June 1999.

Physics runs are divided into several sets of "experiments". The period and accumulated luminosity for each experiment are listed in Table 3.3. The history of the luminosity of KEKB is shown in Fig. 3.2, where we can see drastic improvement of KEKB. In Octorber 2002, KEKB achieved the world luminosity record of the peak luminosity of 8.26×10^{33} cm^{-2}s^{-1} and the total integrated luminosity of 100 fb^{-1}.

3.4 KEKB

The configuration of the KEKB storage ring is illustrated in Fig. 3.3. Since the energy of e^+ and e^- beams are different, two separate rings are necessary. The ring for 8 GeV electron is called

---

[3]There are also "energy scan" runs to look for the $\Upsilon(4S)$ resonance peak.

Table 3.3: Experiment numbers (ExpNo). Period and integrated luminosity are also listed. The integrated luminosity listed here gives slightly different value from the official value (101.67 fb^{-1} in total) because of the difference of the analysis library.

ExpNo	Period (year/month/day)	Integrated luminosity (fb^{-1})			
		On resonance	Continuum	Energy scan	Total
3	99/06/02 − 99/07/23	0.016	0.002	0.009	0.027
5	99/10/24 − 99/12/16	0.241	0.019	—	0.260
7	00/01/14 − 00/07/23	5.860	0.589	0.084	6.534
9	00/10/13 − 00/12/28	4.380	—	—	4.380
11	01/01/20 − 01/04/16	8.322	1.216	0.124	9.663
13	01/04/22 − 01/07/16	10.817	1.209	0.065	12.090
15	01/10/06 − 01/12/25	12.840	1.412	—	14.251
17	02/01/18 − 02/03/13	12.022	0.848	—	12.869
19	02/03/15 − 02/07/01	25.483	3.645	—	29.128
21	02/09/09 − 02/10/02	4.340	—	—	4.340
23	02/10/04 − 02/10/31	6.253	1.433	—	7.685
Total		90.574	10.373	0.283	101.230
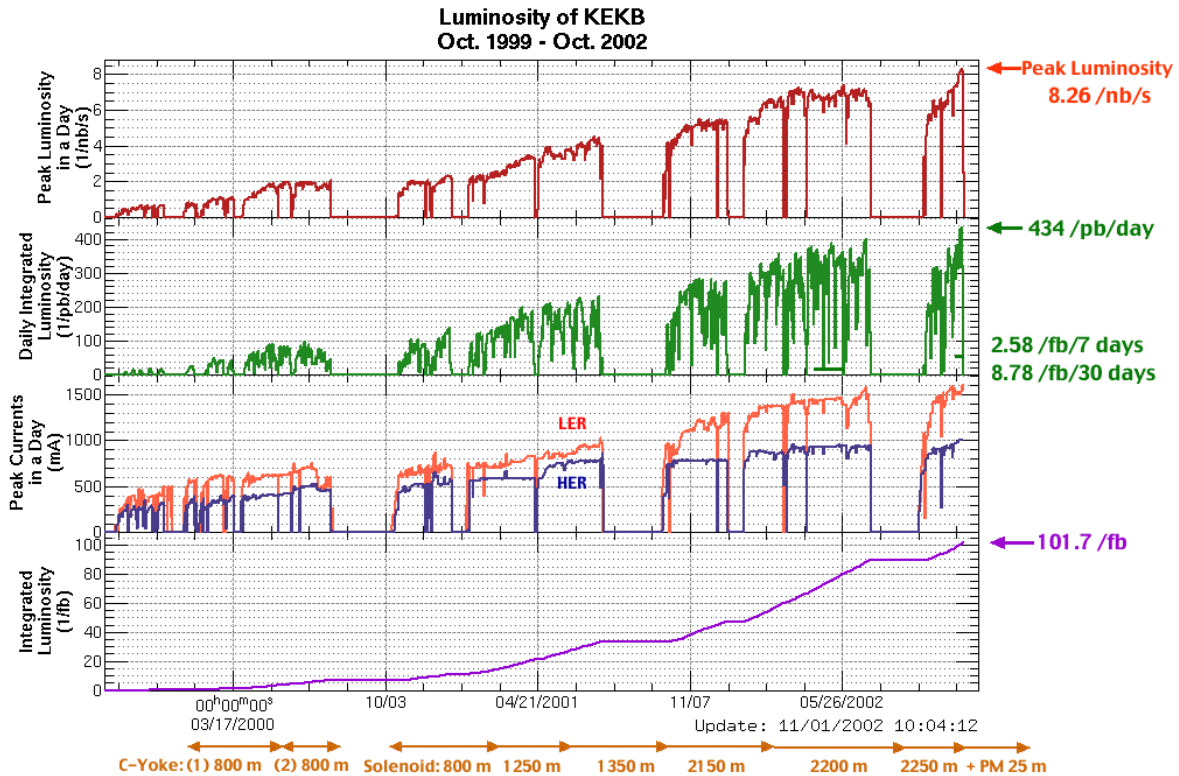
Figure 3.2: History of the luminosity of KEKB.
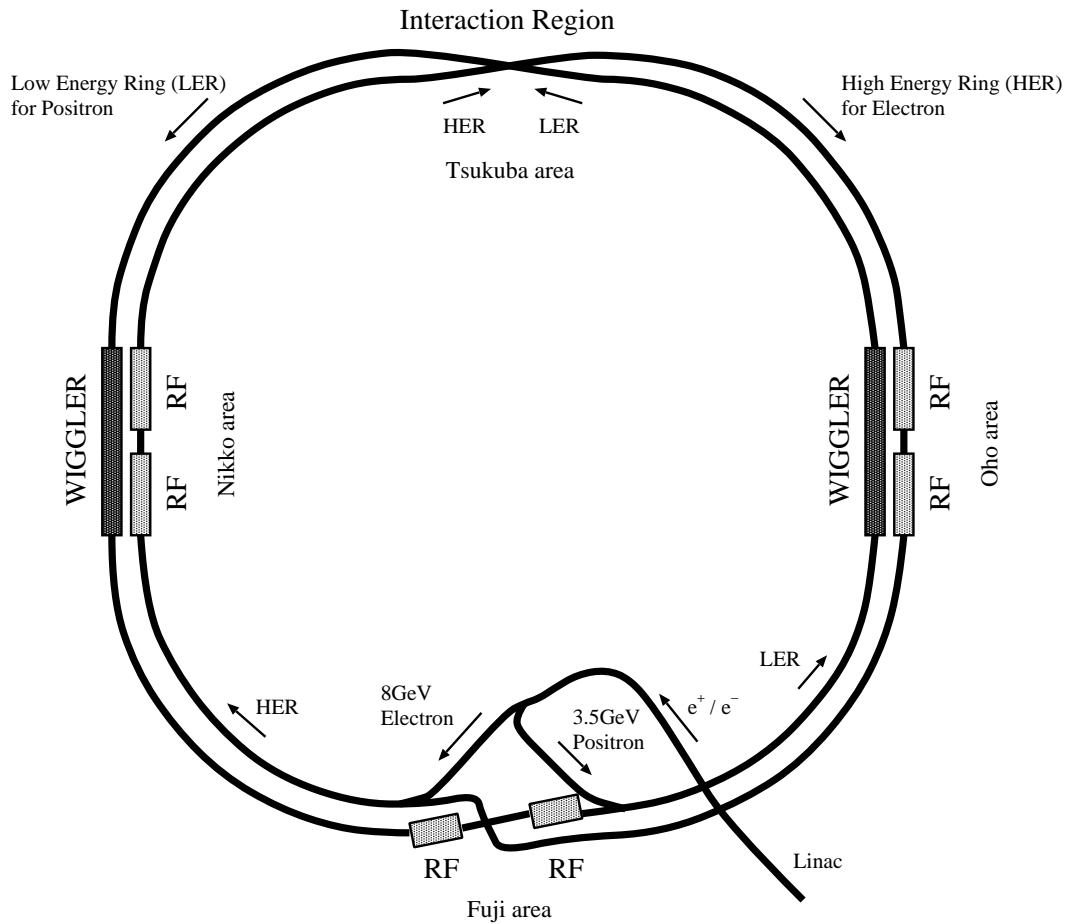
Figure 3.3: KEKB ring.

high energy ring (HER), and that for 3.5 GeV positron is called low energy ring (LER). The HER and LER were constructed side by side in the tunnel used for TRISTAN. Each ring has straight sections in the Fuji, Nikko, Tsukuba and Oho area. They are crossed in the only interaction point (IP) in the Tsukuba area, where the Belle detector is placed. At the IP, electrons and positrons collide with a finite crossing angle of ± 11 mrad. The straight section in the Fuji area is used to inject 8 GeV electron and 3.5 GeV positron beams from the linac. The circumference of the ring is 3016 m. In order to make the circumferences of the two rings precisely equal, a cross-over of the two rings is built in the Fuji area.

In order to compensate the energy loss of the beams due to radiations, two kinds of RF cavities, normal conductivity cavities called ARES[4] and superconducting cavities (SCC), are installed [45]. The RF frequency is 508.887 MHz, which is almost the same as that for TRISTAN to reuse the RF components. The LER is equipped with 16 ARES cavities[5] in the Fuji area, while the HER has 10 ARES cavities in the Oho area and 8 SCCs in the Nikko area. In the Oho and Nikko area, wigglers are installed to the LER in order to reduce the longitudinal damping time of the LER.

The basic machine parameters of KEKB were determined so that the luminosity reaches

---

[4]Accelerator Resonantly coupled with Energy Storage.

[5]Four ARESs are not installed as of summer 2002.

1×10^{34} cm^{-2}s^{-1}. The luminosity L can be written as

$$L = \frac{N_+ N_- f}{4\pi \sigma_x^* \sigma_y^*},\tag{3.5}$$

where N is the number of the particles per bunch, f is the collision rate, σ_x^* (σ_y^*) is the horizontal (vertical) beam size at the IP, and the suffixes $\pm$ indicate positron and electron beam, respectively. There is another formula for the beam-beam tune shift parameter

$$\xi_{y\pm} = \frac{r_e N_\mp \beta_{y\pm}^* f}{2\pi \gamma_\pm \sigma_y^* (\sigma_x^* + \sigma_y^*)},\tag{3.6}$$

where ξ_y is the vertical beam-beam tune shift parameter, r_e is the classical electron radius, β_y^* is the vertical β function at the IP, and γ is the Lorentz boost parameter. The two formulae derive the relation

$$L = \frac{1}{2er_e}\xi_y \left(\frac{\gamma I}{\beta_y^*}\right)_\pm = (2.2 \times 10^{-34})\xi_y \left(\frac{IE}{\beta_y^*}\right)_\pm,\tag{3.7}$$

where e is the elementary electric charge, I is the beam current, and E is the beam energy. The units of L, I, E and β_y^* are given in cm^{-2}s^{-1}, A, GeV and cm, respectively. Here, we require flat beams ($\sigma_x^* \gg \sigma_y^*$) because the design at the IP would be difficult for round beams ($\sigma_x^* \cong \sigma_y^*$). We also assume that σ_x^*, σ_y^*, β_y^* and ξ_y^* are same for both the beams, because unequal parameters cause incomplete overlap of both the beams during collision. This assumption requires $I_+ E_+ = I_- E_-$, so the LER current is higher than the HER current. We should make ξ_y larger and β_y^* smaller in order to achieve higher luminosity. The ξ_y was set to around 0.05 empirically. The β_y^* is related to the design of the IP, but is also limited by the relation $\beta_y^*/\sigma_z \geq 1$, where σ_z is the bunch length. We chose $\beta_y^* = 1$ cm and $\sigma_z = 0.4$ cm. Thus, the design beam currents of the HER and LER were determined to be $I_- = 1.1$ A and $I_+ = 2.6$ A. The design parameters of KEKB are listed in Table 3.4.

Table 3.5 gives the best machine parameters corresponding to the highest peak luminosity. The parameters that are presently used for the KEKB operation are partially different from the designed ones as a result of the attempts to increase the luminosity [46]. One of the problems is the blowup effect of the LER beam. The LER beam suffers from the instability due to the electron cloud in the beam pipe, which has been limited the maximum LER current. In order to suppress this effect, solenoids with 50 G were wound in the LER over more than 2 km, which improved the situation drastically. However, the effect of the remaining electrons still limits the LER beam current. The HER current tends to be raised as far as the luminosity increases. Therefore, the balance of the LER and HER current is far from the relation $I_+ E_+ = I_- E_-$ assumed in the design.

Another problem is related to the bunch spacing. In the original plan, the bunch spacing is 0.59 m (2 ns), which means every bucket is filled by the beam.[6] However, we choose the bunch spacing of 4 buckets (8 ns), and instead the beam currents per bunch are higher than those in the design. So far, shorter bunch spacing causes low luminosity, but the reason is not well understood.

Other parameters are also varied from the design values. For example, vertical tunes ν_y of the LER and HER were changed from a value just above integer (0.08) to a value above half integer $(0.50 - 0.60)$ in 2001, which made the machine much more stable. The vertical beta functions β_y^* were squeezed down to below 1 cm. These changes contribute to the improvement of the luminosity.

---

[6]This is the reason that the finite crossing angle collision scheme was adopted.

Table 3.4: Design parameters of KEKB.

Ring		LER	HER	Unit
Particles		e^+	e^-	
Energy	E	3.5	8.0	GeV
Circumference	C	3016.26		m
Luminosity	L	1×10^{34}		cm^{-2}s^{-1}
Crossing angle	θ_x	± 11		mrad
Tune shift	ξ_x/ξ_y	0.039/0.052		
Beta function at the IP	β_x^*/β_y^*	33/1		cm
Beam current	I	2.6	1.1	A
Natural bunch length	σ_z	0.4		cm
Energy spread	σ_E/E	7.1×10^{-4}	6.7×10^{-4}	
Number of bunches		~ 5000		
Bunch spacing	s_B	0.59		m
Particles/bunch		3.3×10^{10}	1.4×10^{10}	
Emittance	$\varepsilon_x/\varepsilon_y$	18/0.36		nm
Synchrotron tune	ν_s	$0.01 \sim 0.02$		
Betatron tune	ν_x/ν_y	45.52/45.08	47.52/43.08	
Momentum compaction factor	α_p	$1 \times 10^{-4} \sim 2 \times 10^{-4}$		
Energy loss/turn	U_0	$0.81^\dagger/1.5^\ddagger$	4.8	MeV
Total RF voltage	V_c	$5 \sim 10$	$10 \sim 20$	MV
RF frequency	f_{RF}	508.887		MHz
Harmonic number	h	5120		
Longitudinal damping time	τ_ε	$43^\dagger/23^\ddagger$	23	ms
Total beam power	P_b	$2.7^\dagger/4.5^\ddagger$	4.0	MW
Radiation power	P_{SR}	$2.1^\dagger/4.0^\ddagger$	3.8	MW
HOM power	P_{HOM}	0.57	0.15	MW
Bending radius	ρ	16.3	104.5	m
Length of bending magnet	L_b	0.915	5.86	m

$\dagger$ without wigglers $\ddagger$ with wigglers

Table 3.5: Measured KEKB parameters. Parameters on Oct. 29 2002, the day KEKB recorded its highest peak luminosity, are listed.

Ring		LER	HER	Unit
Peak Luminosity	L	8.3×10^{33}		cm^{-2}s^{-1}
Tune shift	ξ_x/ξ_y	0.088/0.053	0.080/0.045	
Beta function at the IP	β_x^*/β_y^*	59/0.6	63/0.7	cm
Beam current	I	1450	950	A
Number of bunches		1184		
Bunch spacing	s_B	2.4		m
Horizontal emittance	ε_y	18	24	nm
Synchrotron tune	ν_s	-0.024	-0.021	
Betatron tune	ν_x/ν_y	45.51/43.55	44.51/41.58	
Total RF voltage	V_c	7.2	13.0	MV
Beam lifetime		70@1450	200@950	min@mA
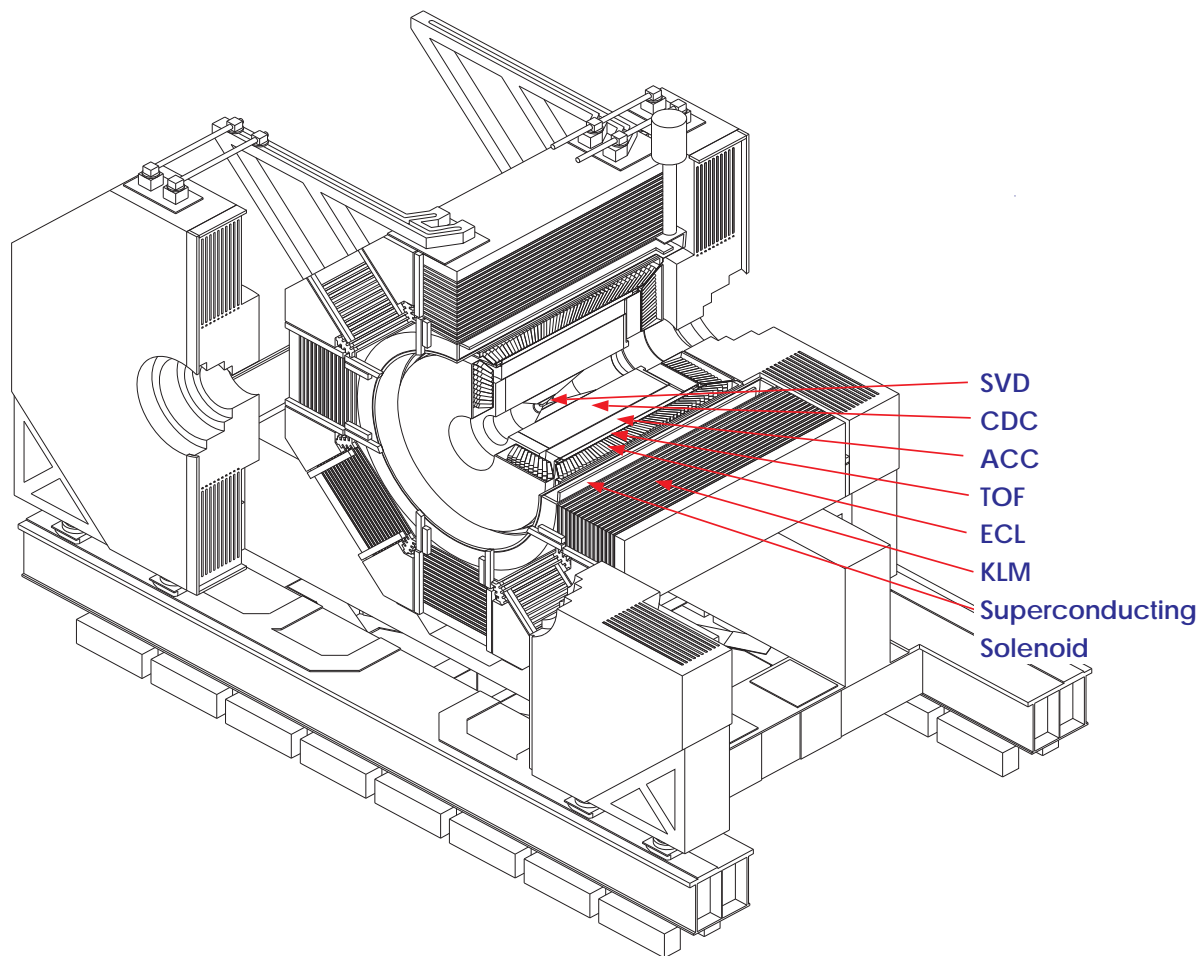
Figure 3.4: Belle detector.

3.5 Belle detector

3.5.1 Overview of the Belle detector

Figures 3.4 and 3.5 illustrate the Belle detector. The Belle detector consists of a three-layer silicon vertex detector (SVD) [47], a 50-layer central drift chamber (CDC) [48], an array of aerogel Cherenkov counters (ACC) [49], time-of-flight scintillation counters (TOF) [50], an electromagnetic calorimeter of CsI(Tl) crystals (ECL) located inside a superconducting solenoid coil that provides a 1.5 T magnetic field, an instrumented iron flux-return for K_L/μ detection (KLM) outside the coil, and an extreme forward calorimeter (EFC) placed near the beam line.

The standard coordinate system in Belle is defined as

- x : outward to the KEKB ring (horizontal),

- y : upward (vertical),

- z : opposite direction of the positron beam axis.

(R, θ, ϕ) and (r, ϕ, z) are expressions in the polar and cylindrical coordinate. That is, θ is the polar angle measured from the z axis, ϕ is the azimuthal angle around the z axis measured from the x axis, and $r = \sqrt{x^2 + y^2}$.
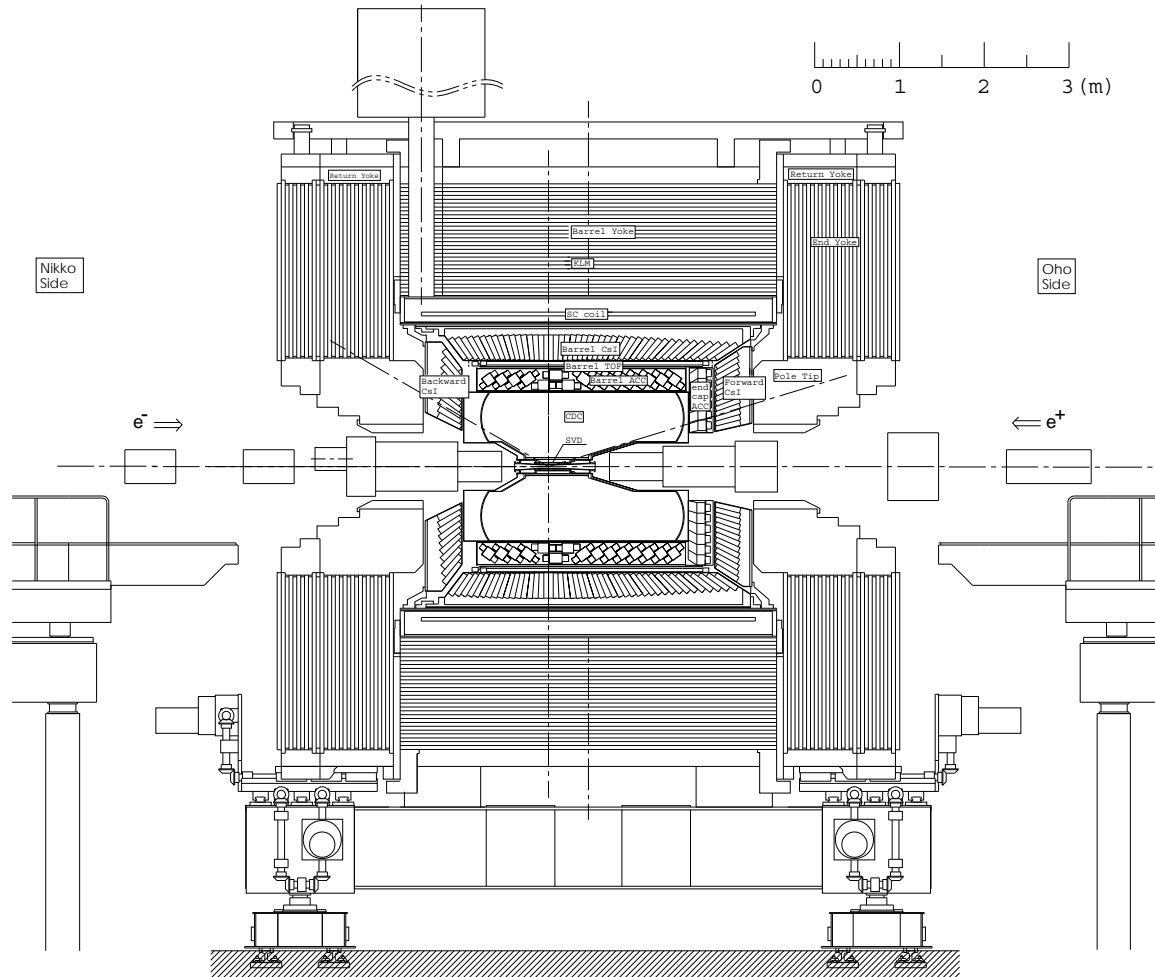
Figure 3.5: Side view of the Belle detector.

The performance of the detector is summarized in Table 3.6. The beam pipe in the interaction region (IR) is made of a double-wall beryllium (Be) cylinder with an inner radius of 20 mm. The two walls are 0.5 mm thick. A 2.5 mm gap between them is used for the cooling by He gas. The superconducting solenoid provides a magnetic field of 1.5 T in a cylindrical volume of 1.7 m in radius and 4.4 m in length with a nominal current of 4400 A. The Belle detector is aligned with the z axis. Namely, the direction of the solenoid field is in parallel to the positron beam. This is because lower-momentum beam particles would suffer more bending in the solenoid field if they were off-axis.

A brief description on each sub-detector is given in the following sections.

3.5.2   Silicon vertex detector (SVD)

Figure 3.6 illustrates the end and side views of the SVD. The SVD has three layers of double-sided silicon strip detectors (DSSD), and covers the region $23° < \theta < 139°$. As shown in the end view of the figure, the three layers consist of 8, 10 and 14 ladders, respectively for the inner, middle and outer layers, around the beam axis. One ladder is made of two half-ladders, and one half-ladder contains one or two DSSDs which is supported by boron-nitride (BN) ribs sandwiched with carbon-fiber reinforced plastic (CFRP). In total, there are 32 ladders and 102

Table 3.6: Summary of the parameters of the Belle detector. The performance is based on the measurement at a beam-test or a physics run.

Detector	Type	Configuration	Readout	Performance
Beam pipe	Beryllium double-wall	Cylindrical, $r = 20$ mm $0.5/2.5/0.5$ mm = Be/He/Be		He gas cooled
SVD	Double-sided Si strip	Chip size: 57.5×33.5 mm^2 Strip pitch: $25(\text{p})/50(\text{n})$ μm 3 layers: 8/10/14 ladders	81920 (ϕ: 65280) (z: 65280)	$\sigma_{\Delta z} \sim 80$ μm (MC)
CDC	Small cell drift chamber	Anode: 50 layers Cathode: 3 layers $r = 8.3 - 86.3$ cm -77 cm $\leq z \leq 160$ cm	Anode 8400 Cathode 1792	$\sigma_{r\phi} = 130$ μm $\sigma_z = 200 - 1400$ μm σ_{p_t}/p_t $= (0.19 p_t \oplus 0.30)\%$ $\sigma_{dE/dx} = 6.9\%$
ACC	Silica aerogel	960 barrel/228 end-cap FM-PMT readout	1788	$N_{\text{p.e.}} \geq 6$ K/π separation at $1.2 < p < 3.5$ GeV/c
TOF	Scintillator	128 ϕ segmentations $r = 120$ cm, 3-m long TSC: 64 ϕ segmentations	TOF: 128×2 TSC: 64	$\sigma_t = 100$ ps K/π separation at $p < 1.2$ GeV/c
ECL	CsI (towered structure)	Barrel: $r = 125$–162 cm Endcap: $z = -102$ cm and 196 cm	Brl: 6624 Fwd: 1152 Bwd: 960	$\sigma_E/E = (0.0066/E$ $\oplus 1.53/E^{1/4} \oplus 1.18)\%$ (E in GeV)
KLM	Resistive plate counters	14 layers (5 cm Fe + 4 cm gap) 2 RPCs in each gap	38×10^3	$\Delta\phi = \Delta\theta = 30$ mrad for K_L $\sim 1\%$ hadron fake
EFC	BGO	Segmentation 32 in ϕ; 5 in θ	320	$\sigma_E = (7 - 10)\%$
Magnet	Supercon.	$r = 170$ cm		$B = 1.5$ T

DSSDs.

Each DSSD has 1280 sense strips and 640 readout pads on both side. The z-strip pitch (n-side) is 42 μm, and the ϕ-strip pitch (p-side) is 25 μm. The size of DSSDs is 57.5×33.5 mm^2. Signals from DSSDs are read out by 128 channel VA1 chips [51] placed on both the sides of the ladder. Inside the VA1 chips, signals are amplified and then sent to shaping circuits, where the shaping time is adjusted to about 1 μs. Then, the outputs of the shaper are held when the VA1 chips receive a level-0 (L0) trigger signal provided by the TOF. This analog information is passed to fast analog-to-digital converters (FADC) in the electronics hut[7] if a level-1 (L1) trigger occurs. The total number of the readout channels is 81920.[8]

---

[7] A hut near the Belle detector. It contains electronics, power supplies, gas systems etc. which are necessary to the operation of Belle.

[8] There are 65280 (= 640×102) readout channels each for z and ϕ. But, when one half-ladder has two DSSDs, a readout pad is connected to both a z-strip of one DSSD and a ϕ-strip of the other DSSD. In this case, the DSSD
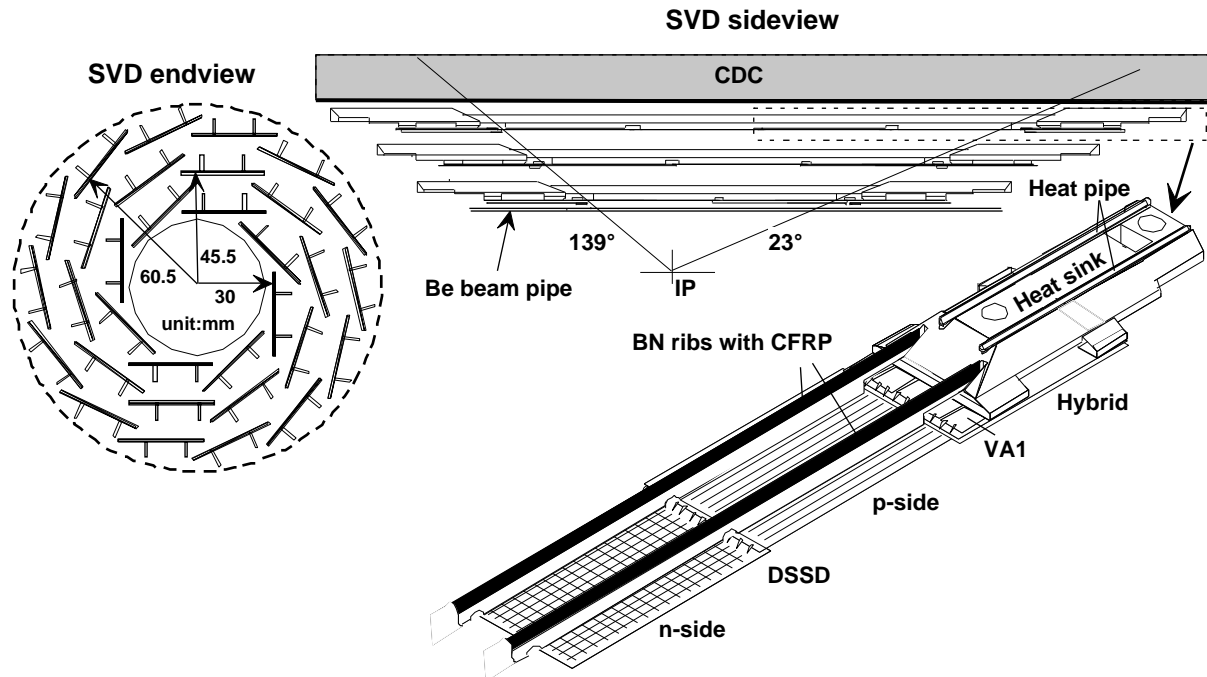
Figure 3.6: Configuration of the SVD.

The main purpose of the SVD is to determine the vertices of B mesons as well as to improve the charged tracking. For the study of the time-dependent CP asymmetries, the distances of the two vertices of B mesons must be measured with the precision of about 100 μm. As shown in Fig. 3.7, the momentum and angular dependences of the impact parameter (closest approach of tracks to the IP) resolution follow

$$\sigma_{xy} = 19 \oplus 49(p\beta \sin^{3/2}\theta)^{-1} \quad \mu\text{m} \tag{3.8}$$

$$\sigma_z = 36 \oplus 42(p\beta \sin^{5/2}\theta)^{-1} \quad \mu\text{m}, \tag{3.9}$$

where $\oplus$ indicates a quadratic sum, and the momentum p is given in units of GeV/c. The impact parameter resolution for an 1 GeV/c normal track is around 55 μm.

3.5.3 Central drift chamber (CDC)

The CDC performs precise determination of three-dimensional trajectories of charged particles, which, together with a 1.5 T magnetic field made by the superconducting solenoid, provides the measurement of momenta of charged particles. In addition, the CDC is used to measure the energy loss (dE/dx) of charged particles for their particle identification. Another important role of the CDC is to provide hardware trigger information in the r-ϕ and z dimensions.

The CDC is a cylindrical wire drift chamber that contains 50 layers (32 axial and 18 small-angle stereo layers) of anode wires, and three cathode strip layers. Since stereo layers combining with axial layers provide z information of tracks, we obtain three-dimensional track information from the anode wires. The cathode strips improve the z measurement [52].[9] They also produce a fast trigger by combining with stereo layers. Figure 3.8 illustrates the configuration of anode

---

can be identified by the polarity of the signal.

[9]However, because we cannot apply enough high voltage to the cathode part due to high background, cathode informations are not used in the analysis.
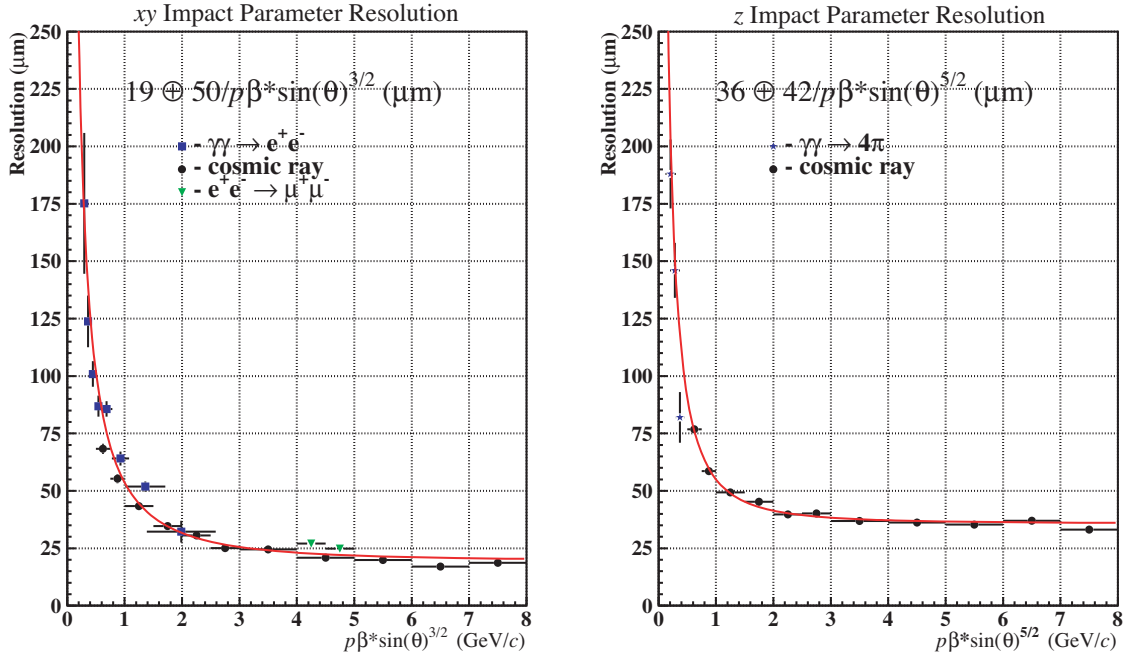
Figure 3.7: Impact parameter resolution of the SVD.

wires and cathode strips. An anode wire (sense wire) and field wires that surround the anode wire form a drift cell. Each drift cell has a maximum drift distance between 8 mm to 10 mm. Positive high voltage of around 2.4 kV is applied to sense wires. In total, there are 8400 sense wires, i.e. 8400 anode channels, and 33344 field wires. The number of cathode channels is 1792.

The structure of the CDC is shown in Fig. 3.9. The CDC covers the volume of 77 mm to 880 mm in radius and $17°$ to $150°$ in polar angle.

The use of low-Z (atomic number) gas is important to reduce multiple Coulomb scattering and improve the momentum resolution. We use a 50% He and 50% C_2H_6 gas mixture, which has a radiation length of around 640 m and a drift velocity of around 4 cm/μs. In spite of the low-Z nature of the mixture, good dE/dx resolution is provided by the large ethane component of the gas.

Signals from the chamber are amplified and sent to the Shaper/QTC modules in the electronics hut. This module shapes and discriminates signals, and performs a charge-to-time conversion (QTC) to the signals. The output signals are read by time-to-digital converters (TDC), which are commonly used for the readout in all the sub-detectors except the SVD. We can determine the drift time from the timing of the leading edge of the output signal of the module, and the input pulse height from the width of the output signal. The input pulse height is used to measure dE/dx.

Let us briefly mention the performance of the CDC. The spacial resolution is approximately $\sigma_{r\phi} = 130$ μm. The p_t resolution is found to be $(0.19 p_t \oplus 0.30)\%$ (p_t is given in GeV/c) by the cosmic-ray data, but is slightly worse in the beam data. As for dE/dx measurement, a scatter plot of measured dE/dx against particle momentum is shown in Fig. 3.10. The dE/dx resolution is measured to be 6.9% for minimum-ionizing pions.
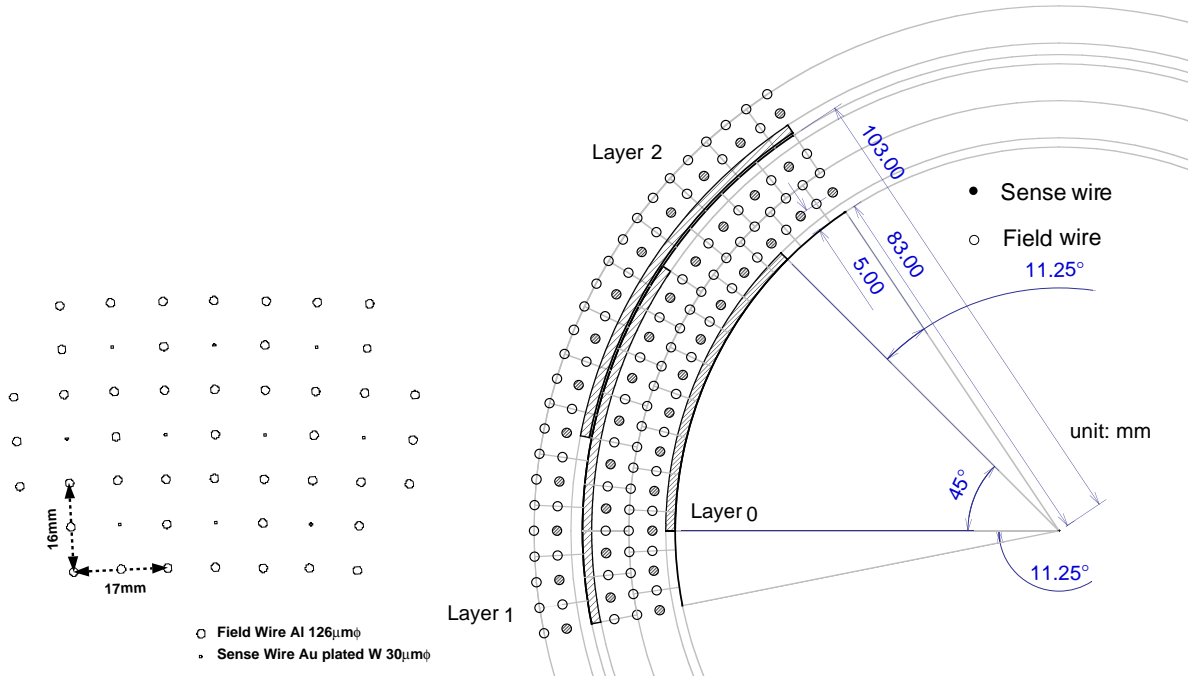
Figure 3.8: Cell structure of the CDC. Cathode strips are also drawn by hatches in the right figure.
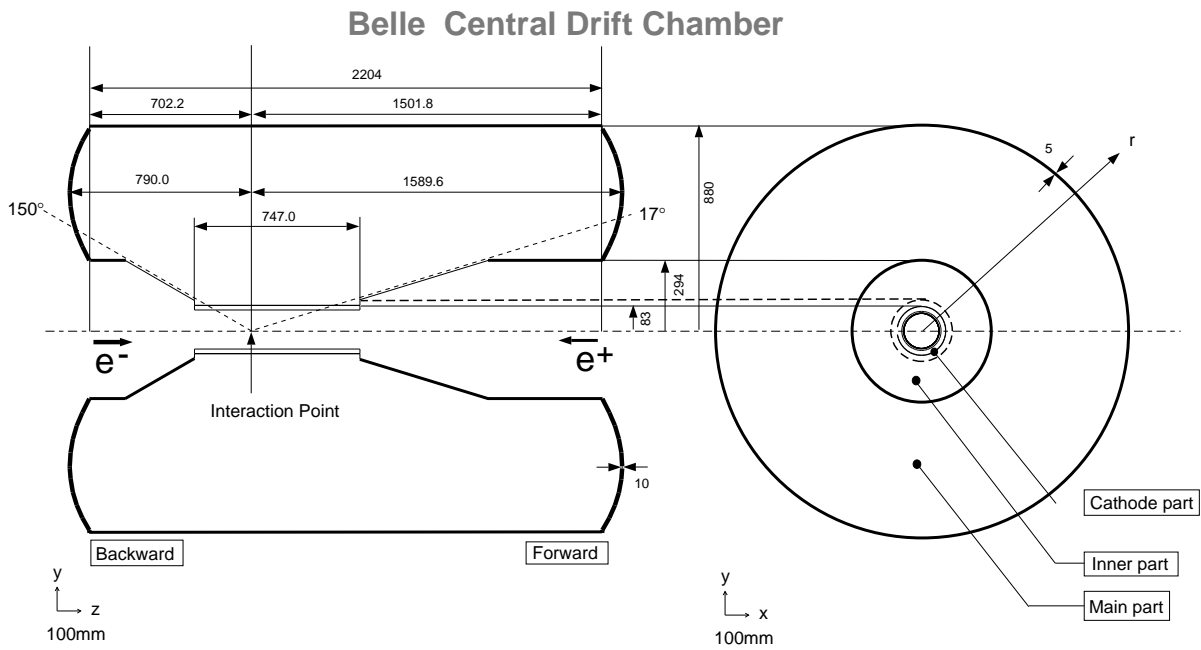
Figure 3.9: Structure of the CDC.
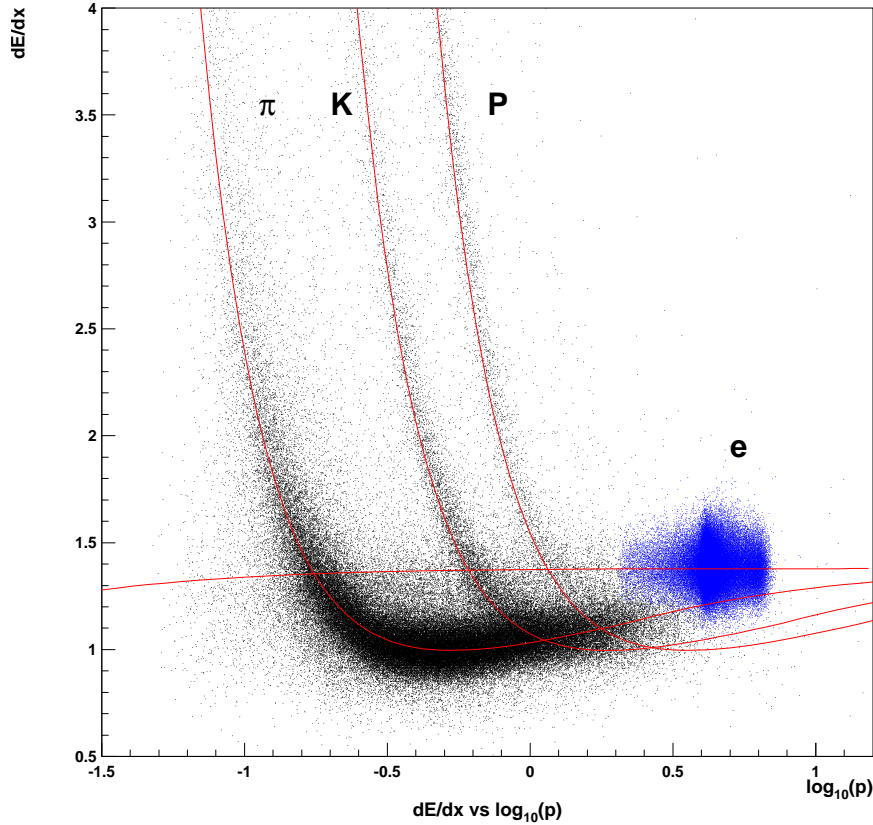
Figure 3.10: Scatter plot for momentum vs. dE/dx. Expected relations for π, K, p and e are also shown by solid curves. The momenta are given in units of GeV/c.

3.5.4 Aerogel Cherenkov counter (ACC)

Particle identification, in particular the identification of π^+ and K^+, plays an important role in the experiment. For example, studies of rare decay modes $B^0 \to K^+\pi^-(\pi^+\pi^-)$ or $B^0 \to \rho\gamma$ require good K/π separation. The K/π separation in the momentum region below 1 GeV/c is performed by dE/dx from the CDC and time of flight measurement (cf. Fig. 3.10). The threshold type silica aerogel Cherenkov counter extends the coverage of the momentum region up to 3.5 GeV/c.

The configuration of the ACC is shown in Fig. 3.11. ACC consists of 960 modules segmented into 60 cells in the ϕ direction for the barrel part and 228 modules arranged in 5 concentric layers for the forward endcap part. Figure 3.12 shows the barrel and endcap ACC module. The refractive indices of aerogels are selected to be between 1.01 to 1.03 depending on their polar angle. Roughly speaking, Cherenkov light is emitted in the aerogel when charged pions above 1 GeV/c pass, while the aerogel is insensitive to charged kaons below 3.5 GeV/c. The Cherenkov light is detected by one or two fine-mesh photomutipliers (FM-PMT) which are operated in the magnetic field of 1.5 T. The total number of PMTs and readout channels is 1788.

Figure 3.13 shows the measured pulse height distribution for e^+ tracks in Bhabha events and K^+ candidates in hadronic events. It indicates clear separation between particles above and below the threshold.
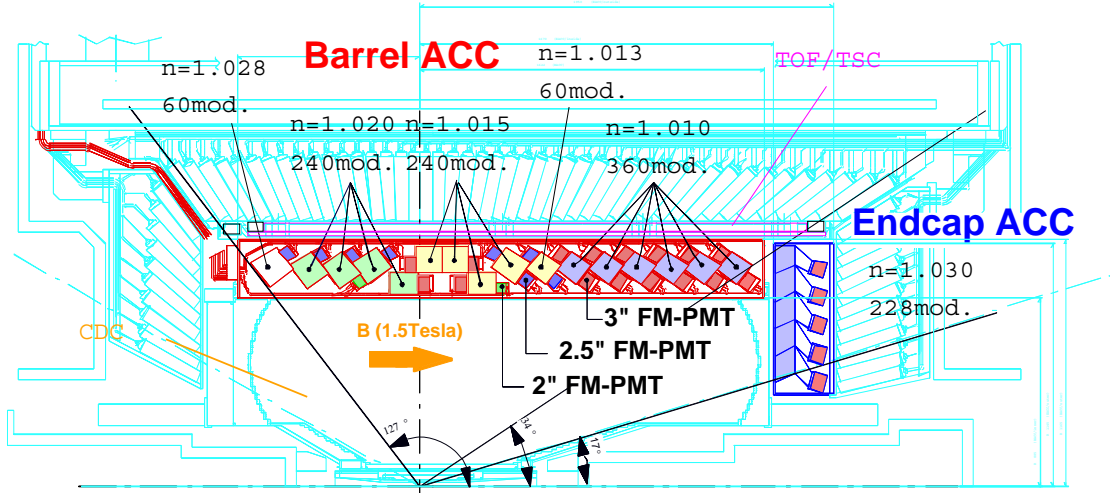
Figure 3.11: Arrangement of the ACC. n indicates the refractive index.

a) Barrel ACC Module
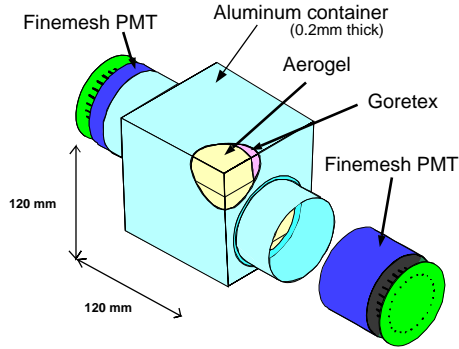
b) Endcap ACC Module
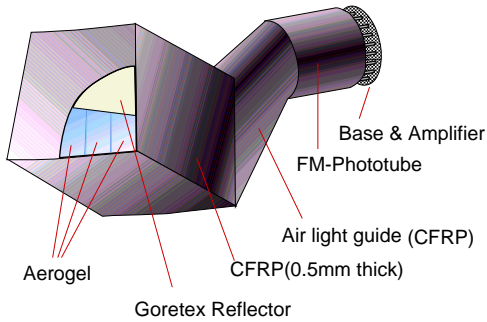
Figure 3.12: Schematic drawing of a typical ACC module.
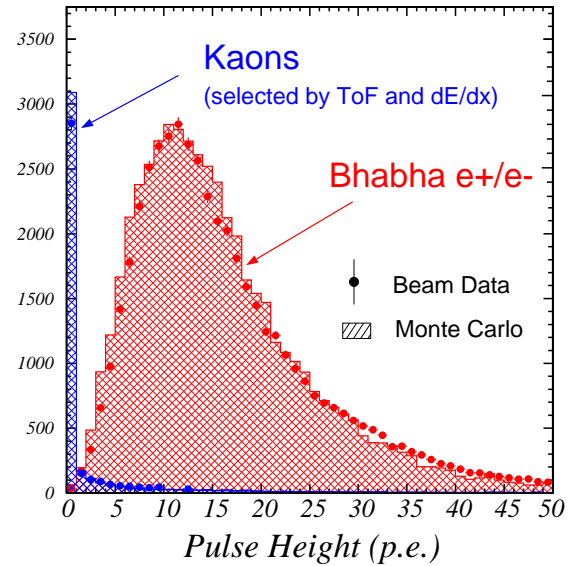
Figure 3.13: Pulse height spectra for electrons and kaons in units of photoelectrons (p.e.) observed by the barrel ACC. Kaon candidates are obtained by dE/dx and TOF measurements. The MC expectation are superimposed.

Table 3.7: Geometrical configuration of the ECL. θ coverage, segmentation (seg.), number of crystals and position are listed.

	θ coverage	θ seg.	ϕ seg.	No. of crystals	Position
Forward endcap	$12.4° < \theta < 31.4°$	13	48 to 144	1152	$z = 196$ cm
Barrel	$32.2° < \theta < 128.7°$	46	144	6624	$r = 125$ cm
Backward endcap	$130.7° < \theta < 155.1°$	10	64 to 144	960	$z = 196$ cm
Total				8736	

3.5.5 Time of flight (TOF)

The TOF detector system provides the particle identification below 1.2 GeV/c as well as the fast trigger signals. The required timing resolution is 100 ps.

Figure 3.14 shows the configuration of TOF counters and a trigger scintillation counter (TSC). TOF counters and TSCs are made of fast scintillators and FM-PMTs that are directly mounted to the scintillator. Two TOF counters (4 cm thick) and one TSC (0.5 cm thick) form one module. TSC is used to produce trigger signals taking a coincidence with the TOF counters to reduce the trigger hit rate. A total of 64 modules are located at a radius of 1.2 m, and cover the region $34° < \theta < 120°$. Each TOF counter is read out by two FM-PMTs at both the ends of the scintillator, while each TSC is read out by a single FM-PMT at the backward end. The total number of TOF counters, TSCs and readout channels are 128, 64 and 320, respectively.

Output pulses from the TOF pass the time-stretcher circuit, which expands the time difference of the TOF pulse and the 64 MHz reference clock by a factor of 20 (Fig. 3.15), and are read out by the TDCs. By this scheme, we can measure the timing of the TOF pulse with 25 ns precision using the common TDCs whose timing precision is 500 ns.

Figure 3.16 shows the mass distribution for tracks in hadronic events, where the momentum and path length are determined by the CDC. We can see a clear peak for π^+, K^+ and p. The distribution for data is in good agreement with that for MC in which the timing resolution of the TOF is assumed to be 100 ps.

3.5.6 Electromagnetic calorimeter (ECL)

The ECL is composed of an array of tower-shaped CsI(Tl) crystals. The configuration is illustrated in Fig. 3.17. Each crystal is arranged so that it points the interaction point.[10] The geometrical configuration of the ECL is shown in Table 3.7. There are 29, 36 and 40 different types of crystal for barrel, forward endcap and backward endcap, respectively. Typical size of CsI(Tl) crystals for the barrel region is 5.5 cm × 5.5 cm in the front face and 6.5 cm × 6.5 cm in the back face. The length of crystals is 30 cm, which corresponds to 16.2 radiation length. Each crystal is read out by a pair of silicon PIN photodiodes.

The energy resolution of the ECL is measured to be [53]

$$\frac{\sigma_E}{E} = \frac{0.0066}{E} \oplus \frac{1.53}{E^{1/4}} \oplus 1.18 \quad (\%), \tag{3.10}$$

where the energy E is given in GeV. Here, the first term is from the contribution of electronic noise, and the second term and a part of the third term come from the shower leakage fluctuation. The third term also includes systematic effects such as the uncertainty of the calibration on crystals. The spatial resolution is found to be $0.27 + 3.4/\sqrt{E} + 1.8/E^{1/4}$ mm.

---

[10]There is small tilt angle so that photons do not pass through a gap between crystals.

Backward   **Forward**

I.P (Z=0)

- 91.5   - 80.5   - 72.5   182. 5   190. 5

1. 0
PMT   PMT   4. 0   TOF   4.0 t   x   6.0 W   x   255.0 L   PMT   122.0
1. 5

TSC   0.5 t   x   12.0 W   x   263.0 L   R= 117. 5

282. 0
287. 0

Light guide

R=120. 05

PMT   PMT   R= 122. 0

R=117. 5   R= 117. 5

TSC 40t × 60w × 2550L   BC408

TSC 5t × 120w × 2630L   BC412

2" FM-PMT   **TOF/TSC Module**

Figure 3.14: Configuration of a TOF module made of two TOF counters and one TSC.

Collision Time   *TDC Stop*

RF clock
508.9 MHz

2 ns   *TS Clock Edge*

TS clock

16 ns

PMT signal

T

Time Stretcher
output

f x T

T4   T3   T2   T1

Figure 3.15: Scheme for the time stretcher for the TOF.

Figure 3.16: Mass distribution from TOF measurements for particles with momentum below 1.2 GeV/c. Points and histograms show the data and MC distributions, respectively.
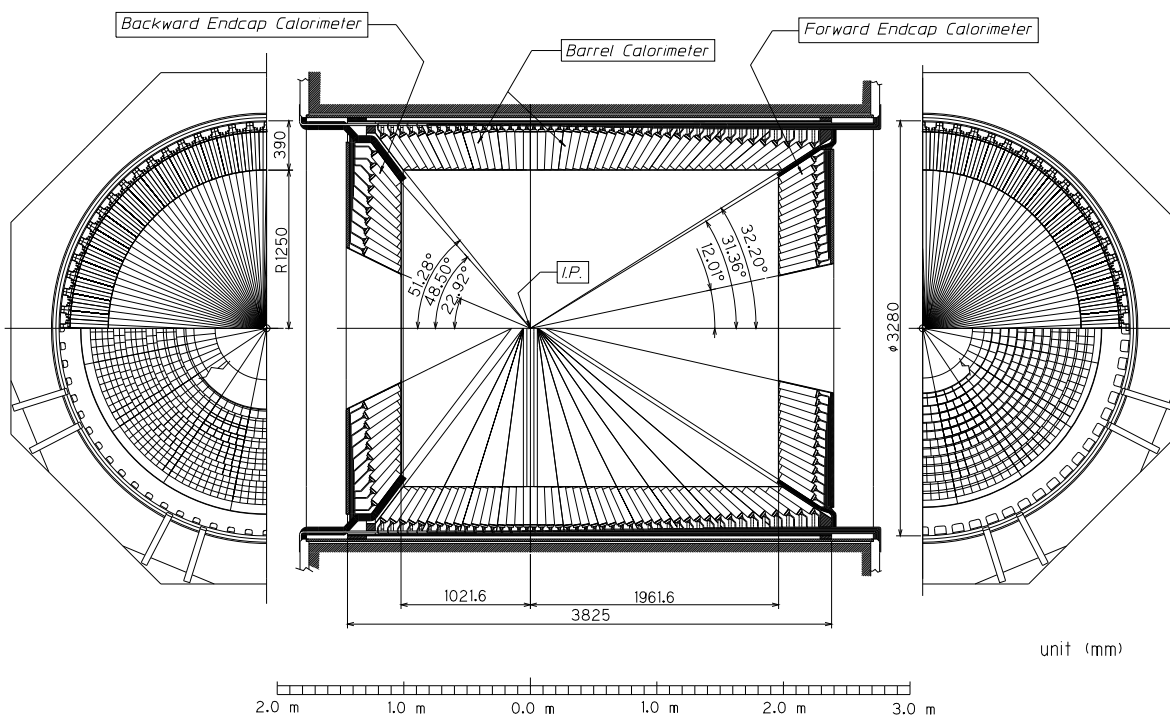
Figure 3.17: Configuration of the ECL.

(a) E/p (b) E_9/E_{25}
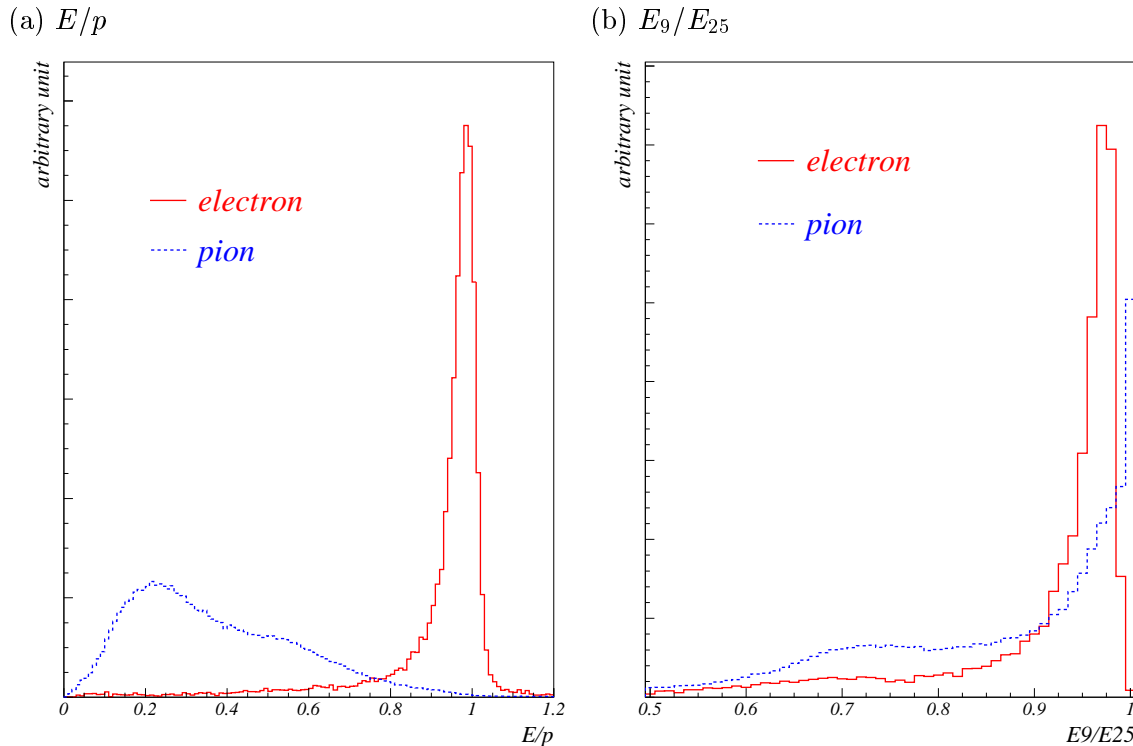
Figure 3.18: (a) E/p and (b) E_9/E_{25} distributions for electrons (solid) and charged pions (dashed). In (a), particle momenta are limited to $0.5 \text{ GeV}/c < p < 3.0 \text{ GeV}/c$.

In addition to the measurement of energy of photons and electrons, the ECL plays an important role for the electron identification [54]. The electron identification is performed combining the following informations.

- Matching between the position of the charged track measured by the CDC and that of the energy cluster measured by the ECL.

- E/p, i.e. a ratio of the energy measured by the ECL and the momentum measured by the CDC.

- E_9/E_{25} at the ECL, i.e. the ratio of the ECL shower energy in an array of 3×3 crystals to the energy in an array of 5×5 crystals.

- dE/dx in the CDC.

- Light yield in the ACC.

We make probability density functions (PDFs) for them, and then calculate a likelihood ratio for every track. Figure 3.18 shows data distributions for E/p and E_9/E_{25} for electrons and charged pions. The distributions for electrons are obtained from radiative Bhabha events ($e^+e^- \rightarrow e^+e^-\gamma$), and those for pions are obtained from $K_S^0 \rightarrow \pi^+\pi^-$ decays. From the MC, the typical electron identification efficiency is estimated to be 92% with the pion mis-identification rate of 0.25% for electrons between 1 GeV/c and 3 GeV/c in the lab frame.

The ECL also provides trigger information and online luminosity information [55]. We briefly describe the trigger system of the ECL in Sec. 3.6.2.

3.5.7 K_L and muon detector (KLM)

The KLM is located outside of the solenoid coil, and perform the identification of muons and the detection of K_L^0 mesons. The KLM consists of alternating layers of resistive plate counters (RPC) and 4.7 cm thick iron plates. The iron plates also serve as the flux-return yoke of the solenoid coil. There are 15 (14) detector layers and 14 iron layers in the barrel (endcap) region.[11] The iron layers provides 3.9 interaction length in addition to 0.8 interaction length of material of the ECL. Muons are identified based on the number of the iron layers penetrated by particles. K_L^0s are detected by a shower of ionizing particles produced inside of the ECL or iron layers by the interaction of the K_L^0. We can measure the location of K_L^0 clusters, but not the energy.

Figure 3.19 shows the schematic diagrams of the cross section of a KLM super layer and the barrel and endcap RPC modules. RPCs have two parallel plate electrodes with high bulk resistivity ($> 10^{10}$ Ωcm) separated by a gas-filled gap. In the streamer mode, an ionizing particle traversing the gap initiates a streamer in the gas that results in the discharge of the plates. The discharge induces a signal on external pickup strips along θ or ϕ directions.

3.5.8 Extreme forward calorimeter (EFC)

The EFC is located in the extreme forward ($6.4° < \theta < 11.5°$) and backward ($163.3° < \theta < 171.1°$) region surrounding the beam pipe. The distance between the front surface of the crystals and the IP is 60 cm and 43 cm, respectively. The inner radius of the detector is 6.5 cm. The EFC is made of BGO ($Bi_4Ge_3O_{12}$) crystals which are tolerant to very high radiation. The lengths of the crystals are 12 and 11 radiation lengths for the forward and backward part. The energy resolution is found to be between 7 to 10% at 1 to 3 GeV [56]. The EFC is segmented into 32 in ϕ and 5 in θ both for the forward and backward part. Hence, the total number of readout channels is 320.

Along with the energy measurement in the small polar angle region, the EFC is used for the online luminosity monitor and the beam monitor for the KEKB control. It can also be used as a tagging device for the two-photon physics.

3.6 Trigger

3.6.1 Level-1 (L1) trigger

In the experiment with high luminosity, physics events including $B\bar{B}$ events are produced in a high rate. However, we also expect high beam background due to the high beam current. Therefore, the trigger system, which selects useful events from many unnecessary events in the online level, plays an important role. The Belle experiment adopted a two-level trigger system of hardware trigger called level-1 (L1) trigger, and an online software trigger called level-3 (L3) trigger.[12] In this section, we summarize the L1 trigger system in Belle. The L3 trigger is described in Sec. 3.7.2.

Table 3.8 lists the cross sections and trigger rates at the design luminosity of 10^{34} cm^{-2}s^{-1} for the various physics processes of interest. Bhabha events and $\gamma\gamma$ events are useful for luminosity measurements and detector calibration, but these triggers should be prescaled due to their high rates. The total physics trigger rate is expected to be around 100 Hz. The trigger rate due to

---

[11]The outer two layers of the endcap have been disabled since Nov. 2001 due to high background.

[12]We do not have a level-2 trigger which, by convention, represents a trigger that utilizes a part of the data that are read out. On the other hand, there are two more things that are called by similar names. The level-0 (L0) trigger is a pre-trigger signal of the SVD that is sent from the TOF (Sec. 3.5.2). The level-4 (L4) filter (Sec. 3.7.2) is sometimes called L4 trigger, but is not a trigger, to be exact.

(b) barrel RPC

(a) cross section
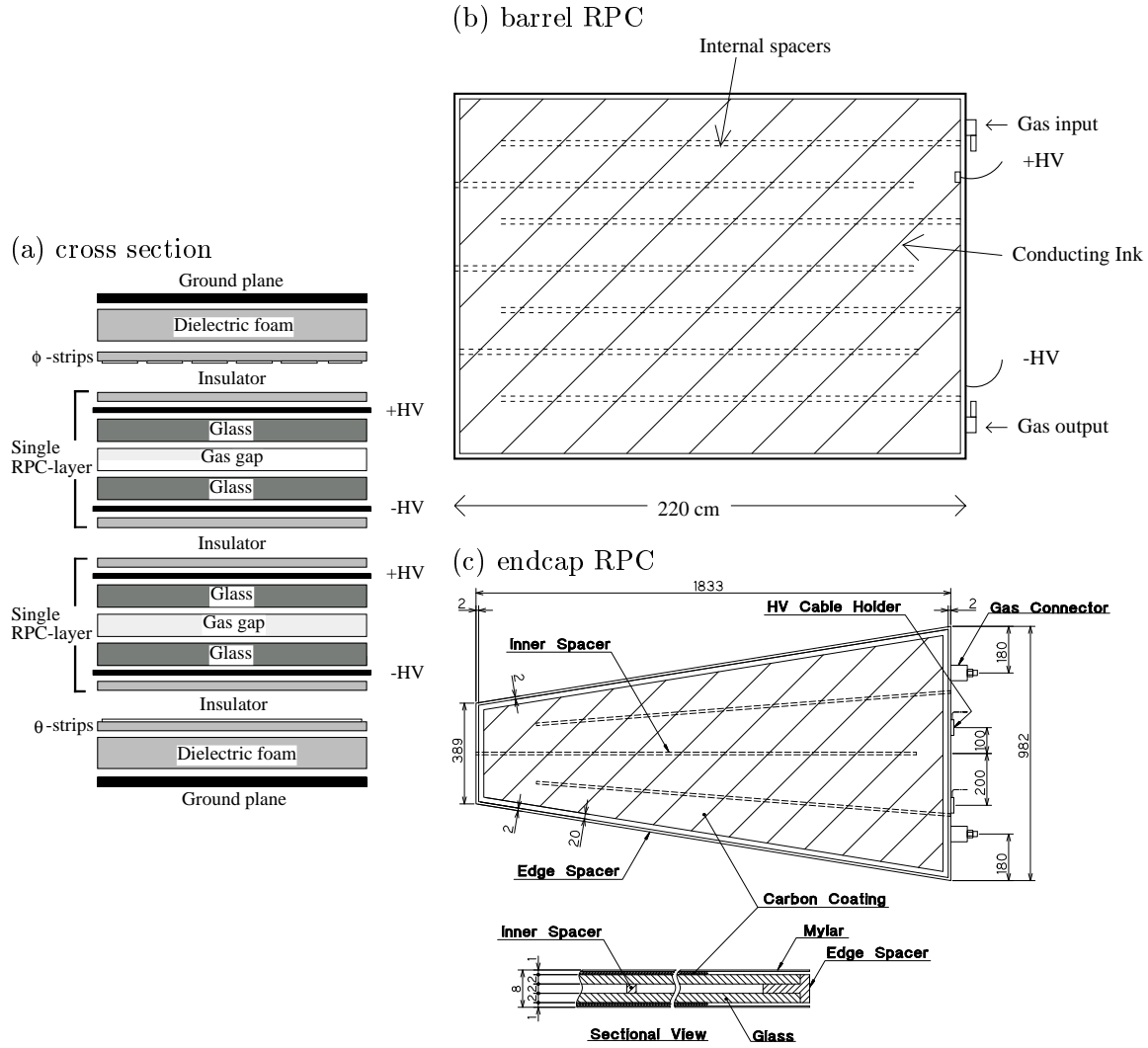
(c) endcap RPC

Figure 3.19: Schematic diagrams of (a) cross section of a KLM super layer, (b) barrel RPC and (c) endcap RPC modules.

beam background is estimated to be around 100 Hz, although it is difficult to reliably estimate it from a simulation. Therefore, the trigger system is designed to keep the rate below 200 Hz, and the data acquisition (DAQ) system is designed to be tolerable to the trigger rate of 500 Hz.

Figure 3.20 shows the overview of the L1 trigger system. It consists of the sub-trigger systems and the central trigger system named Global Decision Logic (GDL) [57]. All the sub-trigger signals must arrive at the GDL within 1.85 μs after the event occurs, and the L1 final trigger signal must be issued 2.2 μs after the event crossing. The timing of the trigger signal must be accurate, because the trigger signal determines the readout timing. We determine the timing of the final trigger by the TOF trigger or ECL trigger.

3.6.2 Sub-triggers

Table 3.9 lists the signals that are provided by the sub-trigger systems. We briefly summarize them below.

The CDC provides two types of triggers: the r-ϕ trigger and the z trigger [58]. The r-ϕ trigger is based on the signals from six axial super-layers, where a super-layer consists of five

Table 3.8: Total cross section (σ) and trigger rates with $L = 10^{34}$ cm^{-2}s^{-1} from various physics processes at $\Upsilon(4S)$.

Physics process	σ (nb)	Rate (Hz)
$\Upsilon(4S) \to B\bar{B}$	1.2	12
Hadron production from continuum	2.8	28
$\mu^+\mu^- + \tau^+\tau^-$	1.6	16
Bhabha ($\theta \geq 17°$)	44	4.4[†]
$\gamma\gamma$ ($\theta \geq 17°$)	2.4	0.24[†]
2γ processes ($\theta \geq 17°$, $p_t \geq 0.1$ GeV/c)	~ 15	~ 35[‡]
Total	~ 67	~ 96

[†] Indicates the values prescaled by a factor 1/100
[‡] Indicates the restricted condition of $p_t \geq 0.3$ GeV/c

or six axial layers. It provides the number of full and short tracks. A full track is formed by a coincidence logic of all the six axial super-layers, while a short track is formed by a coincidence logic of the three inner super-layers. The momentum thresholds for full and short tracks are variable, and are set to around 200 MeV/c and 300 MeV/c, respectively. The r-ϕ trigger also provides triggers based on the event topology. The CDC back-to-back trigger (`cdc_bb`) is issued when the event contains two short tracks with back-to-back configuration (opening angle greater than 160°), and the opening angle trigger (`cdc_open`) is issued when the maximum opening angle of tracks is greater than 135°. The z trigger is formed by signals from the cathode strips and
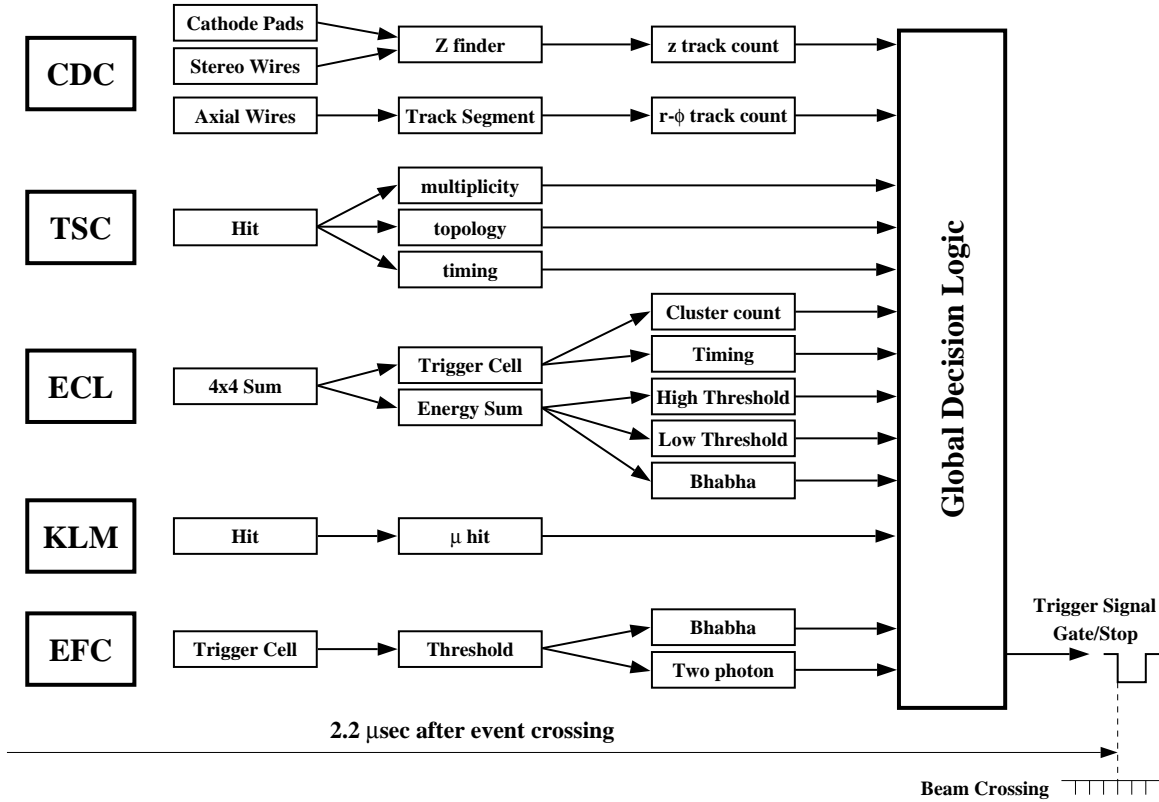
Figure 3.20: Level-1 trigger system for the Belle detector.

Table 3.9: Summary of the sub-trigger signals. The number of the bits (N_{bit}) for each signal is also listed.

Sub-triggers	Name	N_{bit}	Description
CDC	ncdr_full	2	number of CDC r-ϕ full tracks
CDC	ncdr_short	3	number of CDC r-ϕ short tracks
CDC	cdc_bb	1	back-to-back short tracks
CDC	cdc_open	1	maximum opening angle ($> 135°$)
CDC	ncdz	2	number of CDC z tracks
TOF	ntsc	2	number of TSC hits[†]
TOF	tsc_pat	1	TSC back-to-back
TOF	tsc_mult	1	TSC multiplicity
TOF	tsc_timing	1	TSC timing
ECL	ecl_timing	1	ECL timing
ECL	e_high	1	ECL high energy trigger (> 1.0 GeV)
ECL	e_low	1	ECL low energy trigger (> 0.5 GeV)
ECL	e_lum	1	ECL energy trigger to monitor luminosity (> 3.0 GeV)
ECL	csi_bb	1	ECL Bhabha (veto) trigger
ECL	csi_bbpre	1	prescaled ECL Bhabha
ECL	nicl	3	number of isolated cluster
ECL	csi_cosmic	1	ECL cosmic veto trigger
ECL	csi_brlbb	1	ECL barrel Bhabha trigger[‡]
ECL	csi_fabbb	1	ECL Bhabha trigger (AND of forward and backward)[‡]
ECL	csi_fobbb	1	ECL Bhabha trigger (OR of forward and backward)[‡]
ECL	csi_tpbb etc.	4	ECL Bhabha trigger with θ-ϕ segmentation[§]
KLM	klm_fwd	1	KLM forward endcap trigger
KLM	klm_bwd	1	KLM backward endcap trigger
KLM	klm_brl	1	KLM barrel endcap trigger
EFC	efc_bb	1	EFC Bhabha trigger
EFC	efc_tag	1	EFC two photon tag trigger
SEQ	random	1	random trigger
—	revolution	1	revolution signal
SEQ	final	1	delayed final trigger (as a random source)[¶]

[†] tsc_ge1 (TSC hit) and tsc_ge2 (multiple TSC hits) are provided instead of ntsc since exp. 21.

[‡] available since exp. 13 run 451.

[§] in preparation.

[¶] available since exp. 21.

z information inferred from the axial and stereo layer. It provides the number of z-tracks, i.e. tracks that come from near $z = 0$.

The TOF produces trigger signals based on the hit multiplicity and the back-to-back topology. The TOF is divided into 32 segments in ϕ, and the hits in each segment are based on the coincidence of the TOF and TSC. An important part of the TOF sub-trigger system is to make a timing signal. The time jitter of the TOF signal is less than 10 ns. The original design was to produce a timing signal based on a single hit on TOF and keep the single hit rate less than 70 kHz. However, we find the rate is higher due to high background, and we now require a coincidence of more than one hits for the timing signal.
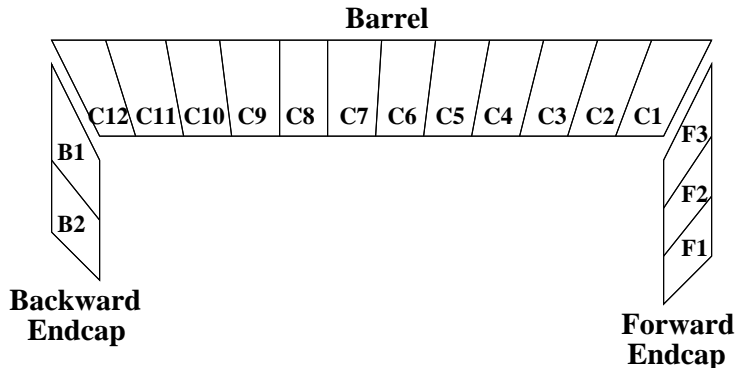
Figure 3.21: Calorimeter division for the selection of Bhabha events in the θ-direction. Each unit represents one ϕ-ring summation.

Table 3.10: ϕ-ring combinations and energy thresholds of the analog sum for the ECL Bhabha trigger. The names of ϕ-rings corresponds to those shown in Fig. 3.21. Type 3 and 11 corresponds to the backward and endcap gap, respectively.

Type	Logic	Threshold	Type	Logic	Threshold
1	F1+F2+B1+B2	5.0 GeV	7	C2+C8+C9	5.0 GeV
2	F2+F3+B1+B2+C11+C12	5.5 GeV	8	C3+C7+C8	5.0 GeV
3	F2	5.0 GeV	9	C4+C6+C7	5.0 GeV
4	F3+C10+C11+C12	5.0 GeV	10	C5+C6	5.0 GeV
5	C1+C9+C10	5.0 GeV	11	C10	3.0 GeV
6	C1+C2+C9	5.0 GeV			

The ECL trigger is based on trigger cells (TC) formed by 4×4 crystals. We segment the calorimeter into 17 ϕ-rings (12 in the barrel and 5 in the endcap) in the θ direction as shown in Fig. 3.21. First, energy deposit in TCs are summed within each ϕ-ring. Then, a total energy signal is formed by summing all the ϕ-rings except B1, F1 and F2. Triggers with three different thresholds are produced. Bhabha triggers are realized by making the analog sum of specific ϕ-rings. Table 3.10 lists 11 types of the ϕ-ring combinations for the Bhabha trigger (`csi_bb`). New Bhabha triggers based on the θ-ϕ segmentation are now in preparation [59].

The ECL also provides a cluster trigger, where the number of isolated clusters are calculated based on the TC hit patterns.

There are two more sub-detectors that contribute to the trigger. The KLM detects muons using four (two) layers in the barrel (endcap) parts, and sends trigger signals to the GDL. The EFC provides two types of triggers. The EFC Bhabha trigger is based on the forward and backward coincidence, while the two-photon trigger is based on a single hit.

The other important sub-trigger is the random trigger, which is useful to understand the background. A random trigger signal of 21 Hz is supplied by the sequence controller (SEQ). The accelerator provides a signal synchronized with the revolution of the beam, which we call the "revolution signal". The rate of the signal is 100 kHz. In addition, since experiment (exp.) 21, the delayed final trigger signal is returned back to the input of the GDL, and is used as a random trigger source whose rate is proportional to the final trigger rate. These random triggers are prescaled so that their rate becomes around 1 Hz.
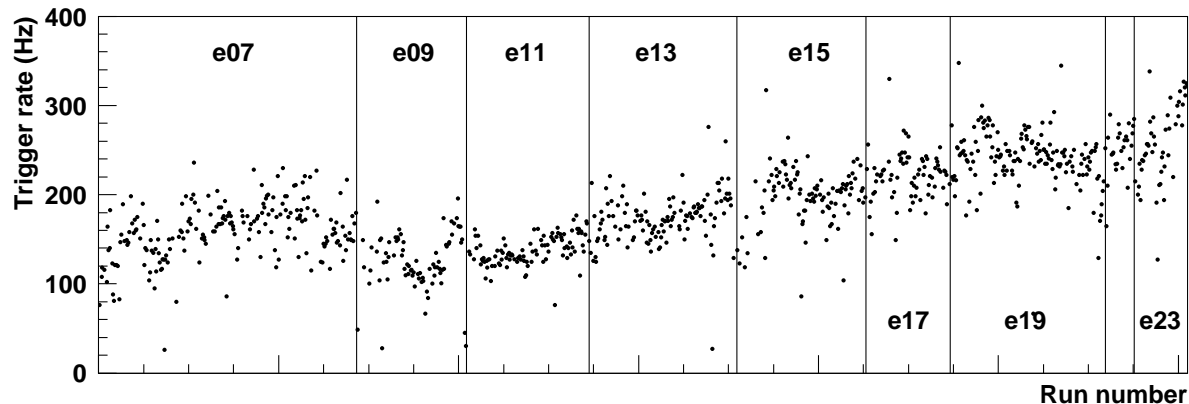
Figure 3.22: Average trigger rate for runs between exp. 7 and exp. 23.

3.6.3 Global decision logic (GDL)

The GDL receives up to 48 sub-trigger signals, and adjusts their timings by adding delays to each channel. Then, it performs trigger logic operation to the sub-trigger signals, and generate 48 types of triggers.[13] These 48 signals are prescaled or disabled channel by channel. Finally, the GDL issues the final trigger 2.2 μs after the event crossing. In order to make the timing of the final trigger signal accurate, the trigger timing is determined by the timing signal from the TOF or ECL. Details of the GDL are described in Appendix B

The trigger logic is determined so that the L1 trigger is fully efficient for $B\bar{B}$ events. We prepare 4 kinds of triggers for $B\bar{B}$ events: 1) three-track trigger based on CDC and TSC sub-triggers, 2) energy trigger from ECL, 3) cluster trigger from ECL and 4) combination of track trigger, energy and cluster trigger. Each trigger provides 90% to 97% efficiency for $B\bar{B}$ events [60]. Because triggers 1) to 3) are almost independent, we expect more than 99% efficiency for $B\bar{B}$ events.

Figure 3.22 shows the average trigger rate for runs between exp. 7 and exp. 23. The trigger rate is correlated to the beam currents and the luminosity, but it also depends on the beam background condition. In spite of the improvement of the beam background condition and the modification of the trigger logic, the trigger rate gradually increases as the beam currents and the luminosity increase.

3.7 Data acquisition and data processing

3.7.1 Data acquisition (DAQ)

The overview of the Belle DAQ system is shown in Fig. 3.23 [61]. Signals from most of the sub-detectors go through a charge-to-time (Q-to-T) converter and are processed by a TDC. Namely, Q-to-T converters make a pulse whose width is proportional to the input charge, and TDCs digitize the timings of the leading and trailing edges. As for TDCs, we use a multi-hit FASTBUS TDC module, LeCroy LRS1877S. Only the SVD use FADCs instead of TDCs. The readout sequence starts when the sequence controller (SEQ) receives a final trigger by the GDL and distributes a common stop signal to TDCs.

The data from each sub-detectors are combined into a single event by the event builder, which converts the "detector-by-detector" parallel data streams to "event-by-event" data. The

---

[13]Since exp. 21, the number of the trigger types are increased from 48 to 64.
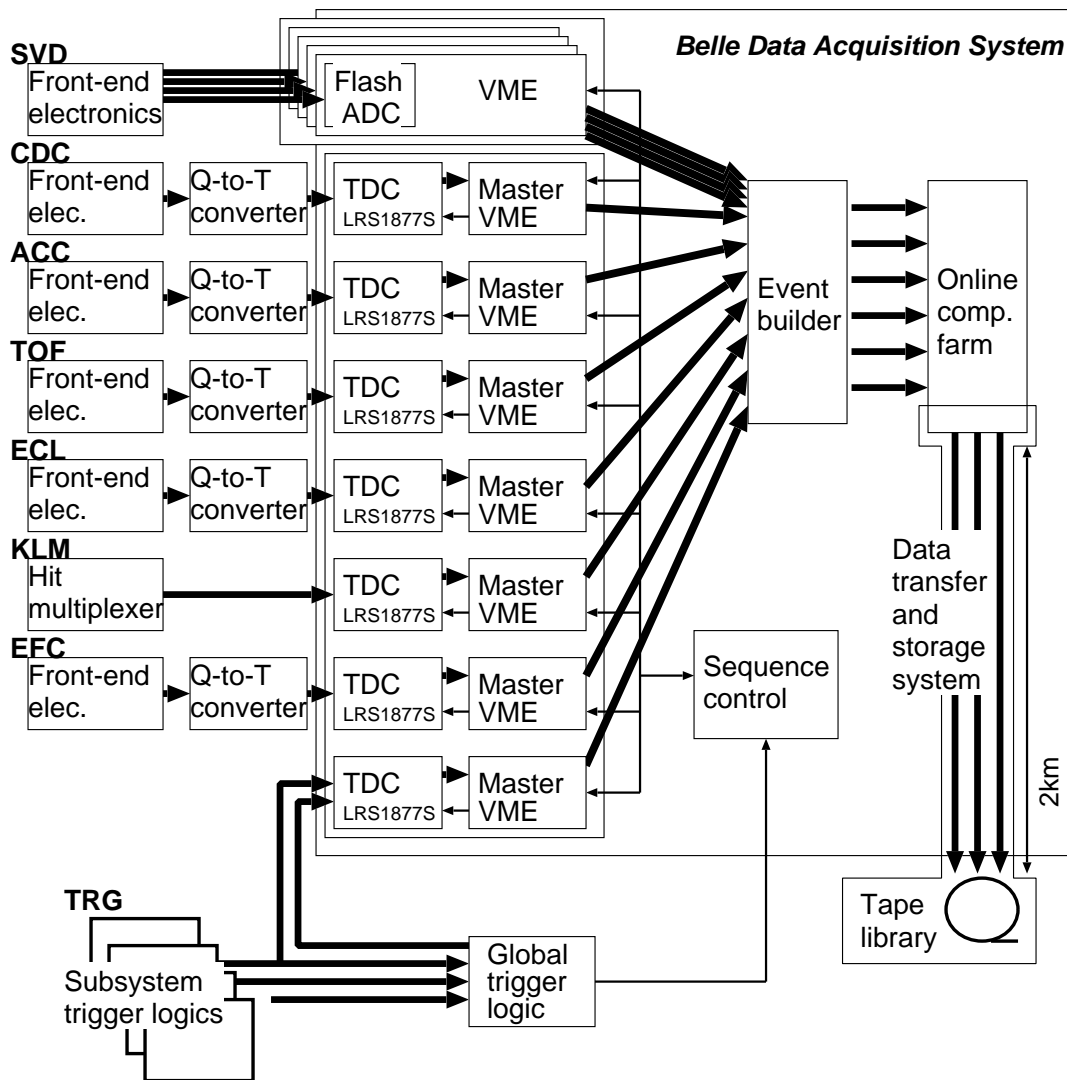
Figure 3.23: Overview of the Belle DAQ system.

output data of the event builder are transfered to the online computer farm, and pass through the L3 trigger. The quality of the data is monitored by the online Data Quality Monitor (DQM) in the online farm. Finally, the data are sent via optical fibers to the mass storage system located at the KEK computer center that is 2 km away from the experimental hall. A typical data size for a hadronic event is around 30 kB, so the maximum data transfer speed is required to be 15 MB/s in the design trigger rate of 500 Hz.

The event builder was a 12×6 barrel shifter [62] as shown in Fig. 3.24 (a). Although it worked well at the beginning of the experiment, we found a saturation of the data acquisition rate at the trigger rate of about 300 Hz due to the larger data size than expected. Therefore, in order to prepare for the higher trigger rate, we developed a switchless event builder [63] based on PCs and Gigabit Ethernet. The overview of the switchless event builder is shown in Fig. 3.24 (b). It is installed in the summer of 2001, and works without problems under condition with the trigger rate of 500 Hz. It is designed to be tolerable up to around 1 kHz.
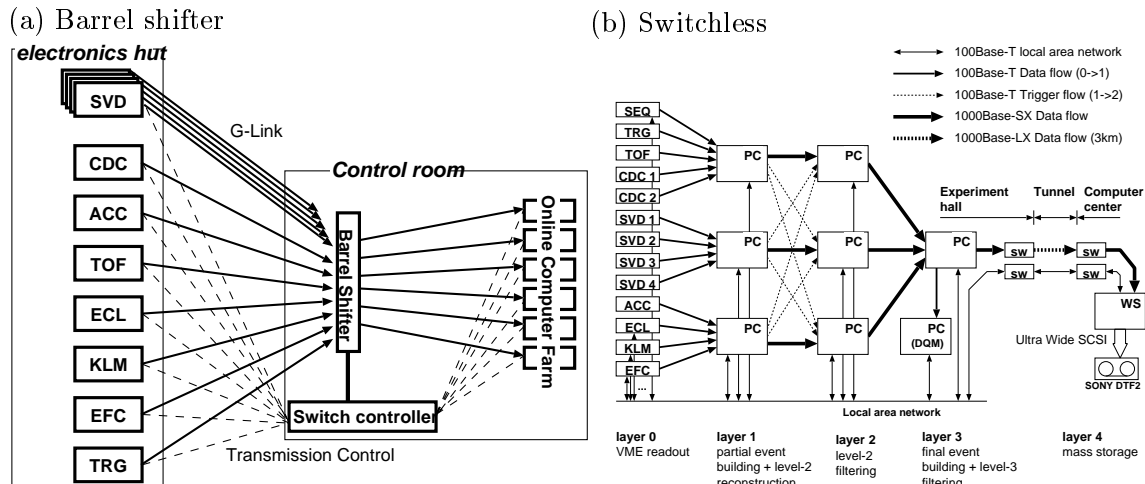
Figure 3.24: (a) Barrel shifter and (b) switchless event builders.

3.7.2 Level-3 (L3) trigger and level-4 (L4) filter

The L3 trigger is an online software trigger which processes the data after the event building. The L3 first checks the L1 trigger information, and passes some categories of events such as Bhabha events and random trigger events. If an event does not belong to these categories, the L3 performs a fast reconstruction and discards the event if it has no track with $|z| < 5$ cm. A large part of the beam background events are discarded by this procedure.

The L3 software is activated from exp. 11. We find around 50% of the events triggered by the L1 are discarded by the L3 filter, while the efficiencies of the L3 filter for hadronic and τ-pair events are more than 99%.

The L4 filter is an offline software applied to raw data before full event reconstruction [64]. The purpose and procedure of the L4 are similar to the L3 trigger. The biggest difference is that events rejected by the L4 still remain in raw data, while events rejected by the L3 are not recorded anywhere. So, the L3 is effective to reduce the data size to be recorded, while the L4 is effective to reduce the time and CPU consumption for the DST production (Sec. 3.7.3).

In the L4, charged tracks are reconstructed by a fast tracker, and events are selected if at least one track with the transverse momentum greater than 300 MeV/c originates from $r < 1$ cm and $|z| < 4$ cm.

3.7.3 DST production and event classification

The events accepted by the L4 filter are reconstructed and the information is stored as Data Summary Tape (DST). In this stage, raw data, the contents of which are direct logs from data acquisition devices, are converted into physics objects of momentum 3-vector p_μ, closest approach x_μ to the IP and associated particle identification information.

Then, events are classified into several categories based on the certain selection criteria, and stored as the skimmed data, accordingly. Table 3.11 lists examples of the event classification. Most analyses, including this analysis, start from the `HadronB` sample (Sec. 4.3.1).

Table 3.11: Examples of event classifications.

Category	Description
HadronB	general hadronic events
HadronC	tight general hadronic events (≥ 5 tracks)
Bhabha	Bhabha ($e^+e^- \rightarrow e^+e^-$) events
RadBhabha	radiative Bhabha ($e^+e^- \rightarrow e^+e^-\gamma$) events
GammaPair	$e^+e^- \rightarrow \gamma\gamma$ events
MuPair	$e^+e^- \rightarrow \mu^+\mu^-$ events
TauPair	$e^+e^- \rightarrow \tau^+\tau^-$ events
LowMulti	two photon events etc.
Random	random triggered events

Chapter 4

Reconstruction and Background Suppression

4.1 Overview of the analysis

In this analysis, we reconstruct B mesons decaying into $K^+\pi^-\gamma$ and $K^+\pi^-\pi^+\gamma$ final states. We start from events that pass general selection criteria for hadronic events. First, we select events that contain a high energy photon (γ). We then form and select a K_X system from a kaon and one or two pions in the K_X invariant mass (M_{K_X}) range up to 2.4 GeV/c^2. This M_{K_X} selection covers a large part of the M_{K_X} distribution predicted by various theoretical models. Then, we combine the K_X system with the high energy photon to form a B candidate.

The largest source of background in this analysis originates from continuum $q\bar{q}$ ($q = u, d, s, c$) production including initial state radiation ($e^+e^- \to q\bar{q}\gamma$). We suppress the $q\bar{q}$ background using a selection criterion that utilizes the difference of the event topology between signal events and $q\bar{q}$ events. $B\bar{B}$ decays containing K, π and γ are potential background to our signal; however, the background level is found to be small by MC simulation. Finally, we choose one candidate even if we find multiple candidates in one event.

Details of the signal reconstruction and background suppression are described in this chapter. In estimating acceptance and efficiencies of various selections for the signals $B^0 \to K^+\pi^-\gamma$ and $B^+ \to K^+\pi^-\pi^+\gamma$, we often need good MC simulators. We actually consider various resonant channels such as $B^0 \to K_2^*(1430)^0\gamma$, $B^0 \to K^*(1410)^0\gamma$ and $B^+ \to K^*(1680)^+\gamma$; the efficiency studies based on these MC simulations will be presented in Chapter 5 and 6. However, in this chapter, we often employ $B^0 \to K_2^*(1430)^0\gamma$ as a representative example for those MC simulations. Distributions such as $\cos\theta_\gamma$ and E_9/E_{25} (see below for the detail) are found almost independent of resonant channels, and are well represented by the particular decay.

After finding $B^0 \to K^+\pi^-\gamma$ and $B^+ \to K^+\pi^-\pi^+\gamma$ signal candidates, we estimate the signal yield and the branching fraction. We also decompose the signal to several sub-components. These procedures are described in Chapter 5 and 6.

4.2 Data set

The analysis is based on an on-resonance data sample of 29.4 fb^{-1} recorded at the Belle detector by the summer of 2001. We do not use off-resonance data due to its small statistics.

The number of $B\bar{B}$ events ($N_{B\bar{B}}$) included in the data sample is estimated using the relation

$$N_{B\bar{B}} = N_{\text{on}} - \frac{\epsilon_{\text{on}}}{\epsilon_{\text{off}}} \frac{\mathcal{L}_{\text{on}}}{\mathcal{L}_{\text{off}}} N_{\text{off}}, \tag{4.1}$$

where N_{on} (N_{off}), ϵ_{on} (ϵ_{off}) and $\mathcal{L}_{\text{on}}$ ($\mathcal{L}_{\text{off}}$) are the number of events, the $q\bar{q}$ efficiency and the luminosity in the on-resonance (off-resonance) data, respectively. $N_{B\bar{B}}$ is evaluated to be

$$N_{B\bar{B}} = (31.92 \, {}^{+\,0.31}_{-\,0.32}) \times 10^6. \tag{4.2}$$

We use Monte Carlo (MC) simulation for the study of the efficiency, background and so on. MC events are generated using an event generator called QQ [65] and the response of the Belle detector is simulated with a GEANT3-based program [66]. MC samples used in the analysis are listed in Table 4.1. In MC samples for specific B decays, the other side Bs follow "generic B decay", i.e. they decay through $b \to c$ transition with the branching fractions based on PDG2000 [67].

MC samples for resonant decays $B \to K_X\gamma$ are used to estimate the efficiencies and to determine the coefficients of SFW (Sec. 4.4.1). In the MC samples of $B \to K_X\gamma$, the ratio of events with $K^+\pi^-\pi^+\gamma$ final states to all the events is determined by the isospin relation.[1]

As for the background MC simulation, we analyze a total of 182×10^6 $q\bar{q}$ MC events. In addition, we use MC samples of $B^0\bar{B}^0$ and B^+B^-, where both Bs follow generic decays. We also examine charmless rare B decay MC, which roughly corresponds to 6×10^8 $B\bar{B}$ pairs.[2] The rare B MC contains $B \to PP$, PV, VV and PS decays and $B \to p\bar{p}h$ ($h = K$, π), where P (pseudo-scaler) is either of π, K, η and η', V (vector) is either of ρ, K^*, ω and ϕ, and S (scaler) is either of $K_0^*(1430)$, $f_0(980)$, $f_0(1370)$ and $f_0(1500)$. The branching fractions are based on the central value or upper limit given in PDG2000 [67], but are updated with results from Belle. The branching fractions for $B \to PV$ and PS are obtained from the study of charmless three body B decays at Belle [68], so the MC includes two and three body charmless B decays.

The inclusive $b \to s\gamma$ MC samples are generated as an equal mixture of $s\bar{d}$ and $s\bar{u}$ quark pairs that are hadronized by JETSET [13]. Then, the samples are weighted by rejecting events so that the mass spectrum of the recoil system (X_s) follows the prediction by Kagan and Neubert [69] assuming $m_b = 4.75$ GeV/c^2 (m_b is the b quark mass) and requiring $M_{X_s} > 1.15$ GeV/c^2 [12]. We also generate samples with $m_b = 4.65$ GeV/c^2 and $m_b = 4.85$ GeV/c^2, which are used for the cross check. Corresponding number of $B\bar{B}$ pairs are also shown in Table 4.1 assuming branching fractions measured by Belle (Eq. (2.11) and Table 2.1).

4.3 Signal reconstruction

4.3.1 Hadronic event selection

To select hadronic events ($B\bar{B}$ and $q\bar{q}$ events), general selection criteria called `HadronB` are applied. The selection criteria are as follows [70]:

1. An event has at least three charged tracks with $|p_T| > 100$ MeV/c, $r < 2$ cm and $|z| < 4$ cm. Here, p_T is the transverse momentum and r is the closest distance from the nominal IP, and z is a z-position of the closest point.

2. $E_{\text{vis}}^* > 0.2\sqrt{s}$, where E_{vis}^* (total visible energy) is the sum of energy of charged tracks and reconstructed photons, calculated in the CM frame.

3. The sum of momenta of charged tracks and photons in the CM frame must be balanced along the z axis: $|\sum p_z^* c| < 0.5\sqrt{s}$.

---

[1] For the phase space $K_X \to K\pi\pi\gamma$ decay, we cannot determine the ratio from the isospin relation. So, we assume 0.466 according to the QQ event generator. This assumption does not affect the result.

[2] Due to the uncertainty of the branching fraction, the rare B MC is not suitable for estimating the precise amount of the background contribution from charmless B decays.

Table 4.1: List of MC samples used in the analysis. Charge conjugate modes are included. For example, "2×10000 events of $B^+ \to K_2^*(1430)^+\gamma$ MC" means 10000 events of $B^+ \to K_2^*(1430)^+\gamma$ MC and 10000 events of $B^- \to K_2^*(1430)^-\gamma$ MC. For $B \to K^*(892)\gamma$, four modes with B^0, $\bar{B}^0$, B^+ and B^- are prepared.

Mode	Number of events	
$B^0 \to K^*(1410)^0\gamma \to K\pi\gamma$	2×10000	
$B^0 \to K_2^*(1430)^0\gamma \to K\pi\gamma$	2×10000	
$B^0 \to K_2^*(1430)^0\gamma \to K\pi\gamma$	2×10000	for SFW training
$B^+ \to K_2^*(1430)^+\gamma \to K\pi\gamma$	2×10000	for SFW training
$B^+ \to K_1(1270)^+\gamma \to K\rho\gamma$	2×10000	
$B^+ \to K_1(1400)^+\gamma \to K^*\pi\gamma$	2×10000	
$B^+ \to K_1(1400)^+\gamma \to K\pi\pi\gamma$	2×10000	phase space decay for $K\pi\pi$
$B^+ \to K^*(1410)^+\gamma \to K^*\pi\gamma$	2×10000	
$B^+ \to K_1(1650)^+\gamma \to K\pi\pi\gamma$	2×10000	phase space decay for $K\pi\pi$
$B^+ \to K^*(1680)^+\gamma \to K^*\pi\gamma$	2×10000	
$B^+ \to K^*(1680)^+\gamma \to K^*\pi\gamma$	2×10000	for SFW training
$B^+ \to K^*(1680)^+\gamma \to K\rho\gamma$	2×10000	
$B^+ \to K^*(1680)^+\gamma \to K\rho\gamma$	2×10000	for SFW training
$B^+ \to K_1(1270)^+\gamma$	2×10000	
$B^+ \to K_1(1400)^+\gamma$	2×10000	
$B^+ \to K^*(1410)^+\gamma$	2×10000	
$B^+ \to K_2^*(1430)^+\gamma$	2×10000	
$B \to K^*(892)\gamma$	4×10000	$\sim (4.5 \pm 0.7) \times 10^8 \ B\bar{B}$
$b \to s\gamma$ inclusive ($m_b = 4.65$ GeV)	221430	$\sim (3.7 \pm 1.1) \times 10^8 \ B\bar{B}$
$b \to s\gamma$ inclusive ($m_b = 4.75$ GeV)	247476	$\sim (4.1 \pm 1.1) \times 10^8 \ B\bar{B}$
$b \to s\gamma$ inclusive ($m_b = 4.85$ GeV)	240131	$\sim (4.0 \pm 1.1) \times 10^8 \ B\bar{B}$
$B^- \to D^0\pi^- \to K^-\pi^+\pi^-$	2×20000	
$B^0 \to D^-\pi^+ \to K^0\pi^-\pi^+$	2×20000	
$B^0 \to D^-\pi^+ \to K^+\pi^-\pi^-\pi^+$	2×10000	
$q\bar{q}$	182×10^6	$u\bar{u}, d\bar{d}, s\bar{s} \ 112 \times 10^6 \ + c\bar{c} \ 70 \times 10^6$
generic $B^0\bar{B}^0$	39×10^6	
generic B^+B^-	39×10^6	
rare B decay	0.2×10^6	$\sim 6 \times 10^8 \ B\bar{B}$

4. Event primary vertex must be near the nominal IP: $r < 1.5$ cm, $|z| < 3.5$ cm. This criterion reduces beam gas events.

5. $0.1 < E_{\mathrm{sum}}^*/\sqrt{s} < 0.8$, where E_{sum}^* is the sum of ECL energy of clusters in the CM frame in $17° < \theta < 150°$.

6. At least two ECL clusters are in the barrel region.

7. Average cluster energy is less than 1 GeV.

8. The heavy jet mass M_{jet} is the larger of two invariant masses, where the invariant mass is calculated using the tracks in each of two hemispheres divided by the plane perpendicular to the event thrust axis. $M_{\mathrm{jet}}c^2/E_{\mathrm{vis}}^*$ is around 0.4 for hadronic events, but around 0.2 for τ pair events and around 0.1 for QED events. We apply a selection $M_{\mathrm{jet}}c^2/E_{\mathrm{vis}}^* > 0.25$. Since this cut is slightly tight for $q\bar{q}$ events, we do not reject events with $M_{\mathrm{jet}} > 1.8$ GeV/c^2.

Table 4.2: Efficiencies (ϵ) of the hadronic event (`HadronB`) selection and effective cross sections ($\epsilon\sigma$) for various processes.

Process	$B\bar{B}$	$q\bar{q}$	$\tau^+\tau^-$	QED	$\gamma\gamma$
ϵ (%)	0.991	0.795	0.049	0.00002	0.004
$\epsilon\sigma$ (nb)	1.09	2.62	0.05	0.001	0.04

9. Another energy sum cut $E_{\text{sum}}'^* > 0.18\sqrt{s}$ is applied. In contrast to 5, $E_{\text{sum}}'^*$ includes all the clusters in the calorimeter. As in the selection 8, we keep events with $M_{\text{jet}} > 1.8 \text{ GeV}/c^2$.

The first two selections remove most of the beam gas or beam wall events and two photon events. The selections 5, 6 and 7 are useful to reduce QED events. The selection 8 rejects τ pair events. The selection efficiencies for the selection criteria estimated by MC are listed in Table 4.2.

4.3.2 Photon reconstruction

A photon candidate is reconstructed from an ECL cluster not associated with charged tracks. The standard requirements applied to all photon candidates are as follows [71]:

- $17° < \theta_\gamma < 150°$

- $E_\gamma > 20 \text{ MeV}$

- If E_γ is less than 500 MeV, $E_9/E_{25} > 0.75$ and $w_{\text{shower}} < 6$ cm.

Here, E_9/E_{25} is the ratio of the ECL shower energy in an array of 3×3 crystals to the energy in an array of 5×5 crystals as described before, and RMS shower width w_{shower} is defined as $w_{\text{shower}}^2 = (\sum |\vec{x}_i - \langle\vec{x}\rangle|^2 E_i)/(\sum E_i)$, where $\vec{x}_i$ (E_i) is the position (energy) at the i'th ECL crystal in the cluster and $\langle\vec{x}\rangle = (\sum E_i \vec{x}_i)/(\sum E_i)$.

A radiative B decay event, originating from the basic process of $b \to s\gamma$, generally contains a high energy photon in the final state. In the $B \to X_s\gamma$ decay, the photon energy in the B rest frame is calculated to be

$$E_\gamma^{(B)} = \frac{M_B}{2} - \frac{M_{X_s}^2}{2M_B}, \tag{4.3}$$

where M_{X_s} is the invariant mass of the X_s system. If we move to the CM frame, the photon energy is smeared by the factor of $\beta_B = 0.0614$ to be $(1 - \beta_B)E_\gamma^{(B)} < E_\gamma^* < (1 + \beta_B)E_\gamma^{(B)}$, where $\beta_B c$ is the velocity of the B meson in the CM frame. Figure 4.1 shows the kinematical relation between M_{X_s} and E_γ^*. Two solid lines in Fig. 4.1 show the kinematical boundary set by the formulae above. In order to reduce the data size, we select events containing high energy photons with $1.8 \text{ GeV}/c^2 < E_\gamma^* < 3.4 \text{ GeV}/c^2$. From the figure, we can see that this selection does not remove events with $M_{X_s} < 2.4 \text{ GeV}/c^2$. Figure 4.2 (a) shows the E_γ^* distributions for $B^0 \to K_2^*(1430)^0\gamma \to K\pi\gamma$ signal and $q\bar{q}$ background. We can see that the E_γ^* selection does not remove the signal but reduces $q\bar{q}$ background.

We regard the most energetic photon in an event as the primary photon candidate from a radiative B decay. We apply several criteria for the primary photon. The ECL cluster of the primary photon candidate is required to be within the acceptance of the barrel region ($33° < \theta_\gamma < 128°$). Application of this selection makes us unnecessary to consider the systematic effect of the boundary of the barrel and endcap ECL. As shown in Fig. 4.2 (b), photon candidates
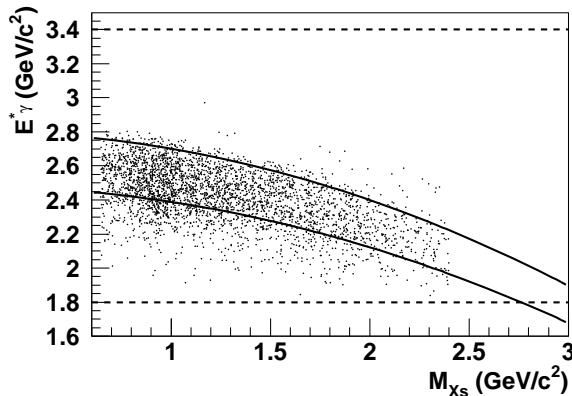
Figure 4.1: Kinematical relation between M_{X_s} and E_γ^* in $B \to X_s\gamma$ decays. Two solid curves show the kinematic boundary. The dashed lines show the selection to be applied. Inclusive $b \to s\gamma$ MC events that are reconstructed in $B^0 \to K^+\pi^-\gamma$ final states up to $M_{X_s} = 2.4$ GeV/c^2 are also plotted for comparison.

in the endcap ECL region are not so useful, because the contribution from $q\bar{q}$ background including initial state radiation ($e^+e^- \to q\bar{q}\gamma$) is large in the endcap region.

Decays of high energy π^0 and η mesons to $\gamma\gamma$ produce high energy photon and hence become background. To reduce this background, we apply a selection on E_9/E_{25}. For high energy π^0 and η, the distance between two photon clusters tends to be small, and the two clusters sometimes overlap to each other resulting small E_9/E_{25}. The distribution is shown in Fig. 4.2 (c). We require $E_9/E_{25} > 0.95$. In addition, we combine the primary photon candidate with all other photon clusters with the energy greater than 30 MeV/c^2 (200 MeV/c^2) in the event, and reject the candidate if the invariant mass of any pair is within 18 MeV/c^2 (32 MeV/c^2) of the nominal π^0 (η) mass. This condition is referred to as the π^0/η veto. The invariant mass distribution for all the combination is shown in Fig. 4.2 (d).

4.3.3 Charged track reconstruction

Charged tracks are reconstructed using the CDC and the SVD. In order to reduce bad quality tracks and electrons from photon conversion in beam-gas or beam-wall background events, we require that charged tracks for the invariant mass calculations should satisfy $dr < 0.5$ cm and $|dz| < 5$ cm, where dr is the closest approach to the IP in the transverse (r-ϕ) plane and $|dz|$ is a z-position of the closest point. This requirement is loose enough compared with the beam size ($\sigma_x \sim 100$ μm, $\sigma_y \sim 5$ μm, $\sigma_z \sim 6$ mm). In addition, we require their CM momenta to be greater than 200 MeV/c. This requirement reduces cross feeds from other $b \to s\gamma$ decays as well as combinatorial background from $q\bar{q}$. Figures 4.3 (a) and (b) show the dr and $|dz|$ distributions for signal and background.

We perform a particle identification (PID) between pion and kaon to every charged track. A single likelihood for each K and π hypothesis ($\mathcal{L}_K$ and $\mathcal{L}_\pi$) is formed based on the Cherenkov light yield from the ACC, the time of flight measured by the TOF, and the energy loss (dE/dx) measured by the CDC. We select kaon and pion candidates by making a selection on the likelihood ratio $PID = \mathcal{L}_K/(\mathcal{L}_K + \mathcal{L}_\pi)$. Figures 4.3 (c) and (d) show the PID distributions for K^+ and π^+ in the $B^0 \to K^+\pi^-\gamma$ analysis. We make a tight selection $PID > 0.6$ for kaon candidates and a loose selection $PID < 0.9$ for pion candidates. From the study with the inclusive η

(a) E_γ^*

(b) $\cos\theta_\gamma$

(c) E_9/E_{25}

(d) $M(\gamma\gamma_2)$
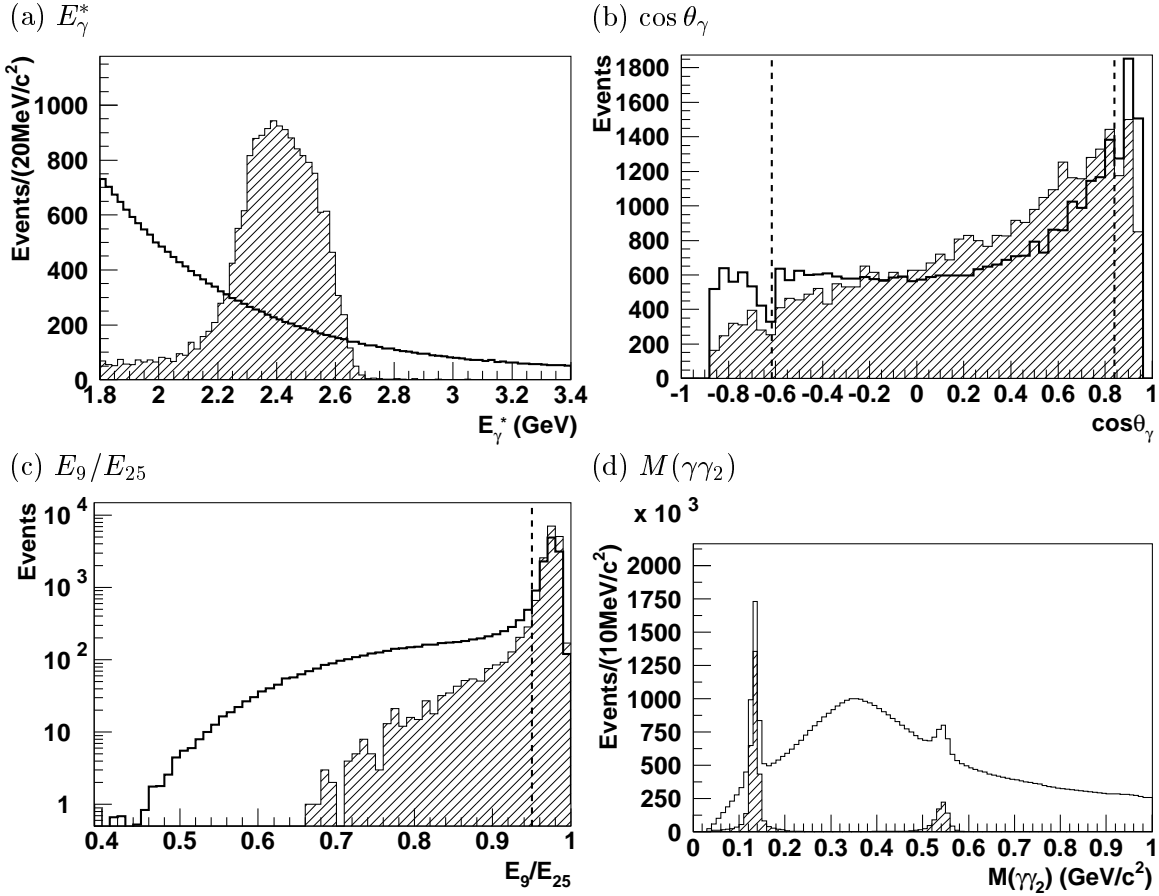
Figure 4.2: (a) E_γ^* (b) $\cos\theta_\gamma$ (c) E_9/E_{25} distributions for signal MC (hatched histogram) and $q\bar{q}$ MC (open histogram). Histograms for $q\bar{q}$ are normalized to the histograms for signal (i.e. same number of events in the plot). The $B^0 \to K_2^*(1430)^0\gamma \to K\pi\gamma$ sample with 20000 events is used as signal MC. Dashed lines show the selection to be applied. (d) Distribution of invariant mass of the primary photon candidate and another photon cluster greater than 30 MeV/c^2 in the $q\bar{q}$ MC. All the combinations are plotted. Contributions from π^0 and η are shown in hatch.

and ϕ samples,[3] we find an efficiency of 83% and a pion mis-identification rate (the probability that pions pass the selection) of 8% for the kaon selection, while the efficiency and the kaon mis-identification rate for the pion selection are 97% and 28%, respectively.

4.3.4   *B* reconstruction

We reconstruct B meson candidates by combining a high energy photon with a K_X system up to 2.4 GeV/c^2, where the K_X system is reconstructed from $K^+\pi^-$ or $K^+\pi^-\pi^+$. We form two independent kinematic variables calculated in the CM frame: the beam constraint mass ($M_{\rm bc}$) and the energy difference (ΔE). They are defined as

$$M_{\rm bc} \equiv \sqrt{\left(E_{\rm beam}^*/c^2\right)^2 - \left(|\vec{p}_{K_X}^* + \vec{p}_\gamma^*|/c\right)^2} \tag{4.4}$$

$$\Delta E \equiv E_{K_X}^* + E_\gamma^* - E_{\rm beam}^*, \tag{4.5}$$

---

[3]The procedures to obtain the efficiencies and mis-identification rates are similar to those described in Sec. 5.4.4 and Sec. 5.4.5.
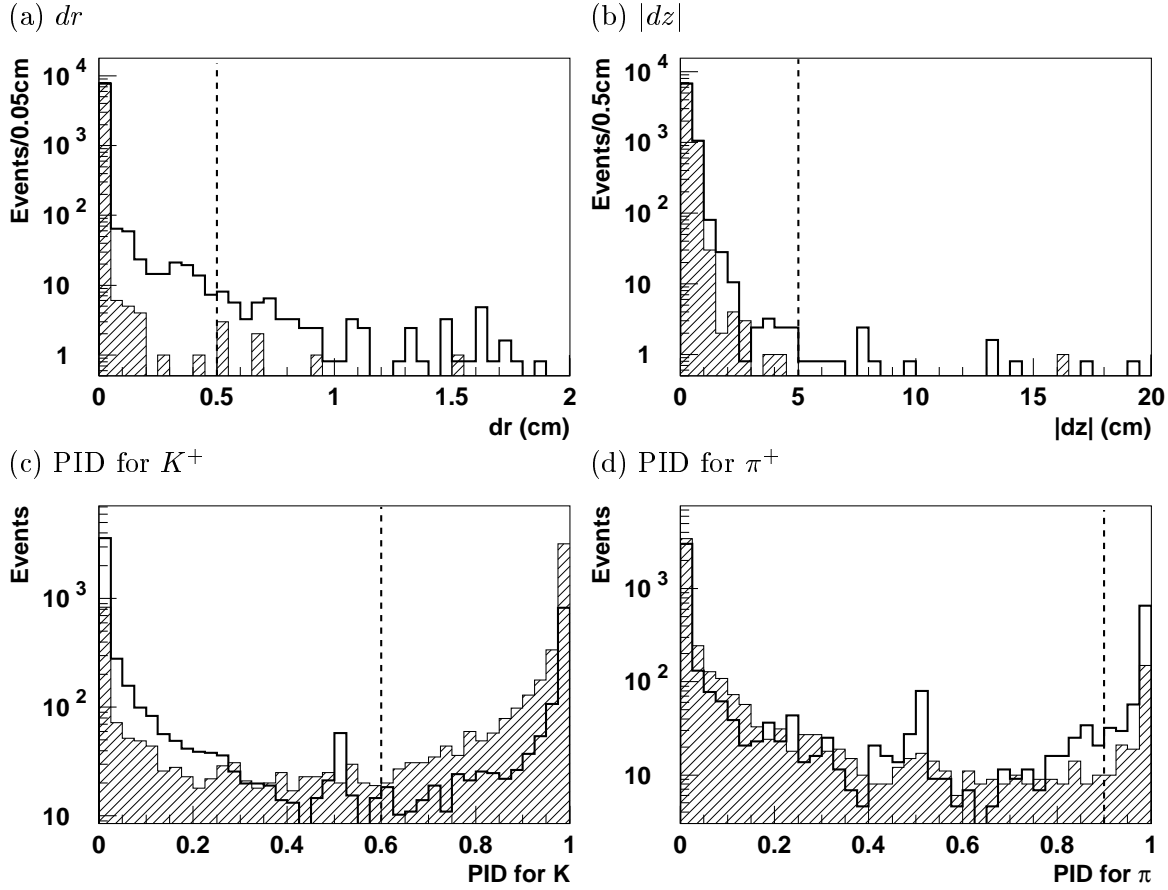
Figure 4.3: Distributions for (a) dr, (b) $|dz|$, (c) PID for K and (d) PID for π for signal (hatched histogram) and $q\bar{q}$ (open histogram) in the $B^0 \to K^+\pi^-\gamma$ analysis, where criteria for primary photons are applied. PIDs for π and K are also applied in (c) and (d), respectively. Histograms for $q\bar{q}$ are normalized to the histograms for signal. The $B^0 \to K_2^*(1430)^0\gamma \to K\pi\gamma$ sample with 20000 events is used as signal MC. Dashed lines show the selection to be applied.

where $\vec{p}_\gamma^*$, E_γ^*, $\vec{p}_{K_X}^*$, $E_{K_X}^*$ are the momenta and energies of the photon and the K_X system, respectively, calculated in the CM frame. The beam energy E_{beam}^* is calibrated using fully reconstructed B decays every some hundred runs [72]. For the M_{bc} calculation, the photon momentum is rescaled so that $|\vec{p}_\gamma^*| = (E_{\mathrm{beam}}^* - E_{K_X}^*)/c$ is satisfied, because the photon energy is less precisely measured than the momenta of charged particles and the beam energy. We apply $|\Delta E| < 0.5$ GeV and $M_{\mathrm{bc}} > 5.2$ GeV/c^2 as a pre-selection.

We show M_{bc} and ΔE distributions for signal and $q\bar{q}$ MC in Fig. 4.4 as an example. Signal events concentrate around $M_{\mathrm{bc}} = 5.28$ GeV/c^2 and $\Delta E = 0$ GeV, while $q\bar{q}$ events distribute almost uniformly in $M_{\mathrm{bc}} < 5.29$ GeV/c^2. Based upon this MC simulations, we define a signal region[4] to be -0.1 GeV $< \Delta E < 0.075$ GeV at $M_{\mathrm{bc}} > 5.27$ GeV/c^2. Note that this ΔE selection will be applied after the best candidate selection described later. We also define a ΔE sideband region to be 0.1 GeV $< \Delta E < 0.5$ GeV with $M_{\mathrm{bc}} > 5.2$ GeV/c^2. The ΔE sideband region, where the signal and $B\bar{B}$ background contribution is negligible, is used to estimate the shape of the $q\bar{q}$ background.

---

[4]Because the ΔE distribution for signal has a long tail in the lower side due to the leakage of the photon energy at the ECL, the criterion for ΔE is chosen to be asymmetric. The ΔE selection removes 19% and 3% of signal on the lower and higher sides, respectively.
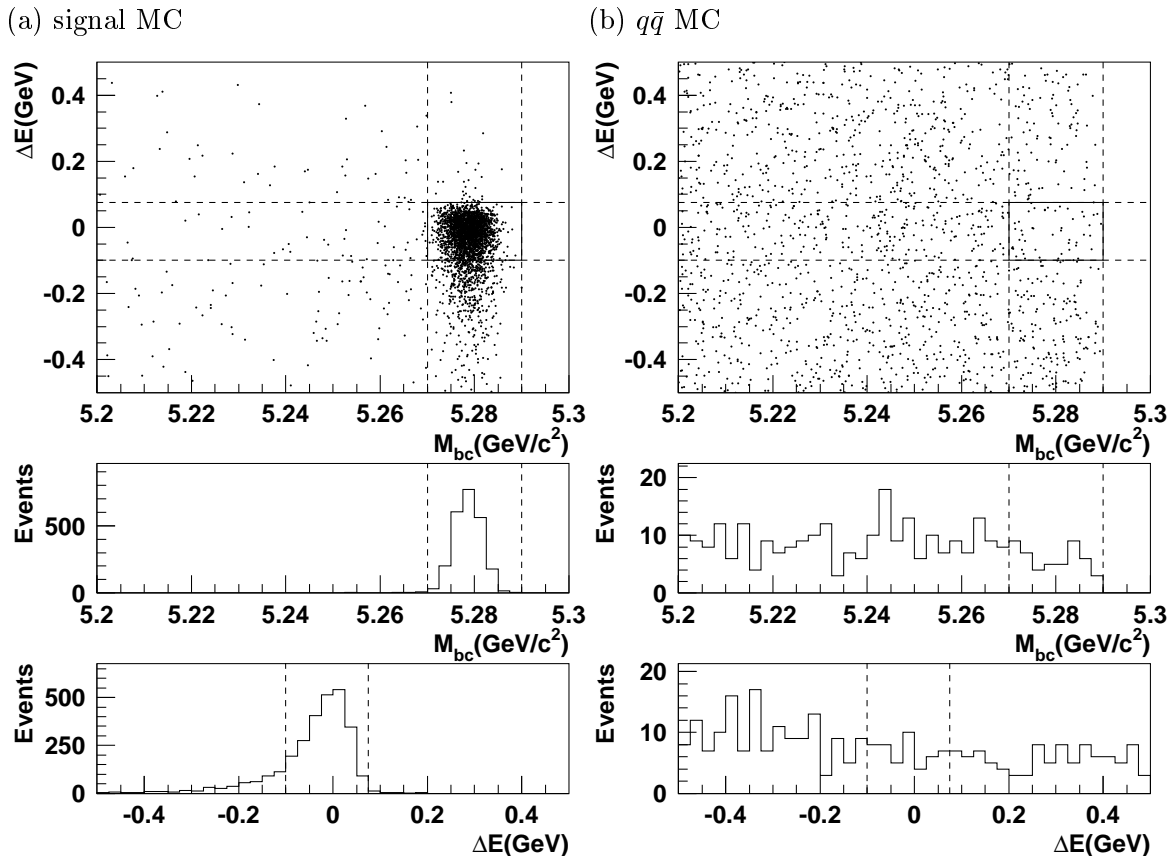
Figure 4.4: M_{bc} vs. ΔE scatter plots and their projections to M_{bc} and ΔE axis for (a) $B^0 \to K_2^*(1430)^0\gamma$ signal MC and (b) $q\bar{q}$ MC in the $B^0 \to K^+\pi^-\gamma$ analysis after applying the selection criteria for the background suppression. In the M_{bc} (ΔE) projections, -0.1 GeV $< \Delta E < 0.075$ GeV ($M_{\mathrm{bc}} > 5.27$ GeV/c^2) is applied. Lines show the signal region (The lines $M_{\mathrm{bc}} = 5.29$ GeV/c^2 is shown only for display purpose; no event exists at $M_{\mathrm{bc}} > 5.29$ GeV/c^2 by definition).

4.4 Background suppression

4.4.1 SFW

To reduce the $q\bar{q}$ background, we use the difference of the event topology between the signal events and $q\bar{q}$ events. Because B mesons are produced almost at rest in the CM system, decay particles from the signal events distribute isotropically. On the other hand, since each quark of the $q\bar{q}$ events is produced with a momentum of a few GeV/c, $q\bar{q}$ events tend to have two jets.

Normalized Fox-Wolfram moments [73] are one of the useful variables to describe the event topology. They are defined as

$$R_l = \frac{H_l}{H_0} = \frac{\sum_{ij}|\vec{p}_i||\vec{p}_j|P_l(\cos\theta_{ij})}{\sum_{ij}|\vec{p}_i||\vec{p}_j|}, \qquad (4.6)$$

where P_l is the Legendre polynomial, and suffixes i and j represent charged particles or photons detected in the detector. R_2 takes a value between 0 and 1, and the value becomes smaller as the event is isotropic. R_2 is often used as a simple event shape variable to separate the signal events from $q\bar{q}$ events.

We divide R_l into three terms:

$$R_l^{\text{kinematic}} = \frac{\sum_{\alpha\beta} |\vec{p}_\alpha||\vec{p}_\beta| P_l(\cos\theta_{\alpha\beta})}{\sum_{\alpha\beta} |\vec{p}_\alpha||\vec{p}_\beta|} \tag{4.7}$$

$$R_l^{\text{major}} = \frac{\sum_{\alpha i} |\vec{p}_\alpha||\vec{p}_i| P_l(\cos\theta_{\alpha i})}{\sum_{\alpha i} |\vec{p}_\alpha||\vec{p}_i|} \tag{4.8}$$

$$R_l^{\text{minor}} = \frac{\sum_{ij} |\vec{p}_i||\vec{p}_j| P_l(\cos\theta_{ij})}{\sum_{ij} |\vec{p}_i||\vec{p}_j|}, \tag{4.9}$$

where α, β run over the particles which are used to reconstruct the signal (the signal decay product), and i, j run over the remaining particles. Unfortunately, $R_l^{\text{kinematic}}$ is highly correlated with M_{bc} and ΔE, because all the momenta used in the calculation of $R_l^{\text{kinematic}}$ are also used in the calculation of M_{bc} and ΔE. So, we do not include $R_l^{\text{kinematic}}$ in the final event shape estimator (see Eq. (4.11)) We also find that R_1^{major} and R_3^{major} have correlations with M_{bc} and ΔE, and we discard them. To further reduce the correlation, the summation over the signal decay products (α) in Eq. (4.8) is restricted to a term from the primary photon:

$$R_l^{\text{major}} = \frac{\sum_i |\vec{p}_\gamma||\vec{p}_i| P_l(\cos\theta_{\gamma i})}{\sum_i |\vec{p}_\gamma||\vec{p}_i|}. \tag{4.10}$$

Finally, we use momenta in the candidate B rest frame, rather than those in the CM frame, which is also useful to reduce the correlation. We then make their linear combination to form a single event shape estimator called SFW (Super Fox Wolfram) which gives better separation power,

$$SFW = \alpha_2 R_2^{\text{major}} + \alpha_4 R_4^{\text{major}} + \sum_{l=1}^{4} \beta_l R_l^{\text{minor}}, \tag{4.11}$$

where R_l^{major} and R_l^{minor} are defined in Eq. (4.9) and (4.10).

The coefficients α_l, β_l in Eq. (4.11) are determined using the method of the Fisher discriminant [74]. The idea of the method is to minimize $D = \left(\sum \lambda_i(\mu_i^{\text{S}} - \mu_i^{\text{B}})\right)/\sqrt{\sum \lambda_i \lambda_j (U_{ij}^{\text{S}} + U_{ij}^{\text{B}})}$ with $(\lambda_i) = (\alpha_2, \alpha_4, \beta_1, \cdots, \beta_4)$ and $(x_i) = (R_2^{\text{major}}, R_4^{\text{major}}, R_1^{\text{minor}}, \cdots, R_4^{\text{minor}})$, where μ_i^{S} (μ_i^{B}) and U_{ij}^{S} (U_{ij}^{B}) are means and covariant matrices of x_i for signal (background), respectively. λ_i that minimizes D can be written in the formula

$$\lambda_i = \sum_j (U_{ij}^{\text{B}} + U_{ij}^{\text{S}})^{-1}(\mu_j^{\text{B}} - \mu_j^{\text{S}}). \tag{4.12}$$

We calculate μ_i^{S} (μ_i^{B}) and U_{ij}^{S} (U_{ij}^{B}) using the signal (background) MC, and we can determine λ_i, i.e. α_i and β_i, from Eq. (4.12). This procedure to determine the coefficients is called "training".

We determine different sets of coefficients for the $B^0 \to K^+\pi^-\gamma$ analysis and the $B^+ \to K^+\pi^-\pi^+\gamma$ analysis. We use a $B \to K_2^*(1430)\gamma \to K\pi\gamma$ MC sample with 40000 events (10000 each for B^0, $\bar{B}^0$, B^+, B^-) as signal MC for $B \to K\pi\gamma$,[5] and an MC sample that contains 20000 $B^+ \to K^*(1680)^+\gamma \to K^*\pi\gamma$ events and 20000 $B^+ \to K^*(1680)^+\gamma \to K\rho\gamma$ events as signal MC for $B^+ \to K^+\pi^-\pi^+\gamma$. A $q\bar{q}$ MC sample that contains 60×10^6 $u\bar{u}$, $d\bar{d}$ and $s\bar{s}$ events and 38×10^6 charm events is used as background MC. The selection criteria applied in the training are listed in Table 4.3. We do not restrict primary photons to the barrel region to increase the statistics. The coefficients are determined to be

$$\alpha_2 = -4.084, \ \alpha_4 = -0.819, \ \beta_1 = -2.4511, \ \beta_2 = 0.1247, \ \beta_3 = 1.246, \ \beta_4 = 1.789 \tag{4.13}$$

---

[5]Not only $K^+\pi^-\gamma$ final states but also $K_S^0\pi^+\gamma$ final state are reconstructed to determine a common set of coefficients for neutral and charged $B \to K\pi\gamma$ analysis, although the result of the analysis for the charged mode is not shown in this dissertation.

(a) $B \to K\pi\gamma$ (b) $B^+ \to K^+\pi^-\pi^+\gamma$
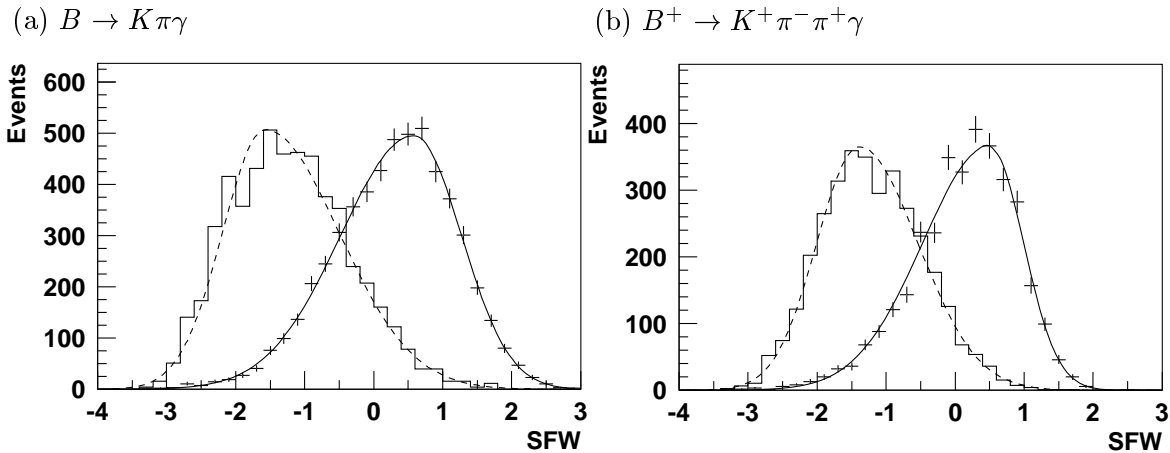
Figure 4.5: SFW distributions for (a) $B \to K\pi\gamma$ and (b) $B^+ \to K^+\pi^-\pi^+\gamma$. The distributions and the fit results for signal ($q\bar{q}$) MC are shown in crosses (open histograms) and solid (dashed) curves.

(a) $B \to K\pi\gamma$ (b) $B^+ \to K^+\pi^-\pi^+\gamma$
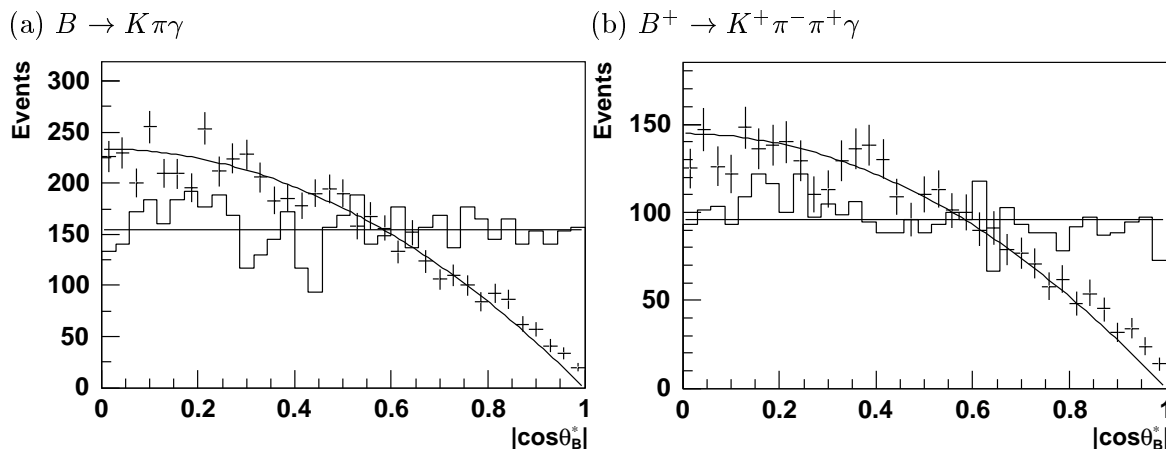
Figure 4.6: $\cos\theta_B^*$ distributions for (a) $B \to K\pi\gamma$ and (b) $B^+ \to K^+\pi^-\pi^+\gamma$. The distributions for signal MC (crosses) follow $1 - \cos^2\theta_B^*$ (solid curves), while those for $q\bar{q}$ MC (open histograms) are uniform (dashed curve).

for $B \to K\pi\gamma$ and

$$\alpha_2 = -3.537, \ \alpha_4 = -0.405, \ \beta_1 = -1.760, \ \beta_2 = -0.449, \ \beta_3 = 0.787, \ \beta_4 = 1.539 \qquad (4.14)$$

for $B^+ \to K^+\pi^-\pi^+\gamma$. The resulting SFW distributions[6] in the signal region are shown in Fig. 4.5. The distributions are fitted with asymmetric Gaussians.

4.4.2 B flight direction

The cosine of the polar angle of the B meson flight direction ($\cos\theta_B^*$) also provides a small separation power between the signal events and $q\bar{q}$ events. The $\cos\theta_B^*$ distribution is $1 - \cos^2\theta_B^*$ for the signal events, while that for $q\bar{q}$ background is uniform because B meson candidates in $q\bar{q}$ background are formed by random combinations. The distributions are shown in Fig. 4.6.

---

[6]The selection on θ_γ is applied.

(a)

(b)
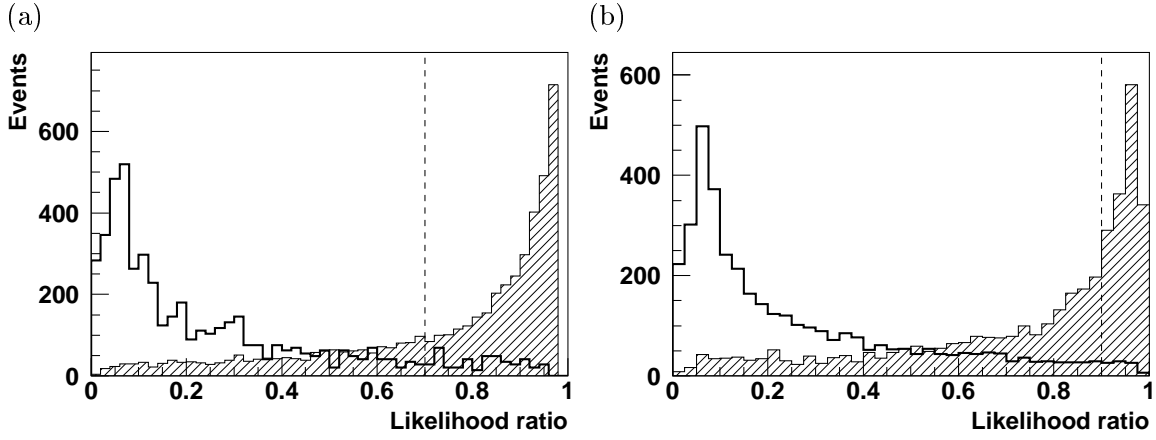
Figure 4.7: Likelihood ratio distributions for (a) $B \to K\pi\gamma$ and (b) $B^+ \to K^+\pi^-\pi^+\gamma$ for signal (hatched histogram) and $q\bar{q}$ background (open histogram). Dashed lines show the selection to be applied.

4.4.3 Likelihood ratio

To make use of full information from SFW and $\cos\theta_B^*$, we calculate a likelihood ratio, LR, defined as

$$LR = \frac{\mathcal{L}_{\text{sig}}}{\mathcal{L}_{\text{sig}} + \mathcal{L}_{\text{bg}}} = \frac{p_{\text{sig}}(SFW)p'_{\text{sig}}(\cos\theta_B^*)}{p_{\text{sig}}(SFW)p'_{\text{sig}}(\cos\theta_B^*) + p_{\text{bg}}(SFW)p'_{\text{bg}}(\cos\theta_B^*)}, \tag{4.15}$$

where $\mathcal{L}_{\text{sig}}$ ($\mathcal{L}_{\text{bg}}$) is the likelihood for signal (background), and p_{sig} (p_{bg}) and p'_{sig} (p'_{bg}) are the signal (background) probability density functions (PDF) for SFW and $\cos\theta_B^*$, respectively. As for the PDFs for $\cos\theta_B^*$, we use $p'_{\text{sig}}(\cos\theta_B^*) = \frac{3}{2}\sin^2\theta_B^*$ and $p'_{\text{bg}}(\cos\theta_B^*) = \frac{1}{2}$. The PDFs for SFW is obtained by fitting the distributions in Fig. 4.5 with asymmetric Gaussians.

Figure 4.7 shows the likelihood ratio distributions for the signal and $q\bar{q}$ MC. The same decay modes as those used in the SFW training are used for signal MC. The selection criteria on the likelihood ratio are chosen so that $S/\sqrt{S+N}$ is maximized, where S and N are signal and background yields obtained from MC assuming the branching fractions predicted by Veseli and Olsson (Table 2.3). We apply $LR > 0.7$ for $B \to K\pi\gamma$ and $LR > 0.9$ for $B^+ \to K^+\pi^-\pi^+\gamma$.

4.4.4 $K^*\gamma$ veto for $B \to K\pi\pi\gamma$

In the $B^+ \to K^+\pi^-\pi^+\gamma$ analysis, $B \to K^*(892)\gamma$ events sometimes pick up another low-momentum pion, and fall in the ΔE sideband region. This may cause a small bias of the M_{bc} distribution in the ΔE sideband. To remove the $K^*(892)\gamma$ contribution in the ΔE sideband, we exclude a $B^+ \to K^+\pi^-\pi^+\gamma$ candidate if M_{bc} and ΔE calculated from K^+, π^- and γ satisfies -0.2 GeV $< \Delta E < 0.1$ GeV with $M_{\text{bc}} > 5.2$ GeV/c^2. This requirement causes negligible inefficiency for the signal components.

4.5 Best candidate selection

We sometimes find multiple B meson candidates with $|\Delta E| < 0.5$ GeV and $M_{\text{bc}} > 5.2$ GeV/c^2 in the same event after applying the selection criteria mentioned above, as shown in Fig. 4.8. In such a case, we take the candidate which has the highest confidence level when we fit the K_X decay vertex. The vertex of the candidate B meson and the other B meson is different in $B\bar{B}$ events, and we expect worse vertex fit if tracks from the other side B are included in the K_X
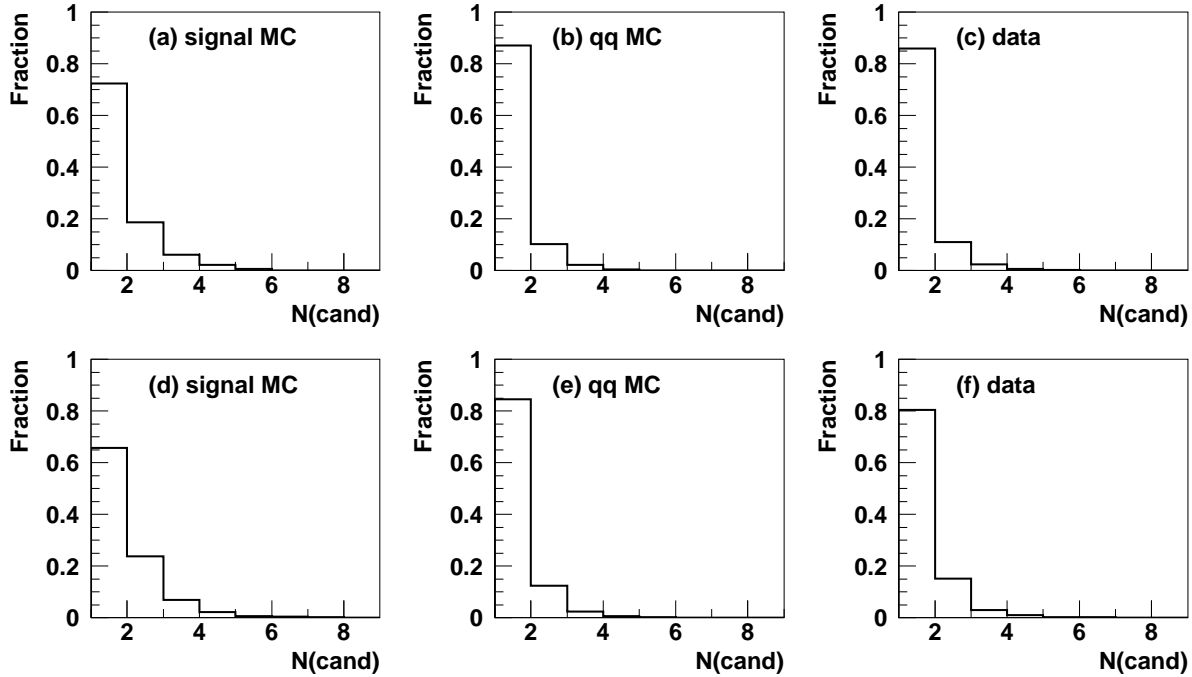
Figure 4.8: Number of candidates in signal MC, $q\bar{q}$ MC and data for (a) – (c) $B^0 \to K^+\pi^-\gamma$ and (d) – (f) $B^+ \to K^+\pi^-\pi^+\gamma$.

decay products. In the $B^0 \to K^+\pi^-\gamma$ analysis, the probability to choose the correct candidate when a event has multiple events is estimated to be 72%, and 64% of incorrect candidates are rejected.

4.6 Summary of the selection criteria

Table 4.3 summarizes the selection criteria. It also shows whether each selection is applied for the SFW training, the determination of the PDFs for LR, and the ΔE sideband.

As described later, the ΔE sideband region (0.1 GeV $< \Delta E < 0.5$ GeV at $M_{\rm bc} > 5.2$ GeV/c^2) is used to estimate the $q\bar{q}$ background shape. For this purpose, we do not apply the selections on θ_γ, the likelihood ratio and the best candidate selection in order to increase the statistics. From the MC study, we find that the $M_{\rm bc}$ distribution is not biased even if we remove these selections.

The last two selection criteria, B reconstruction, will be applied in Chapter 5 and 6, but we list them in the table for convenience.

Table 4.3: Summary of the selection criteria. The column "TR" shows the selections applied for the SFW training. "LR" shows the selections applied to determine the PDFs for the likelihood ratio. "SB" shows the selections for the ΔE sideband data described later. "◯" ("×") represents that the selection is (not) applied.

Category	Selection	TR	LR	SB
B pre-selection	$M_{\rm bc} > 5.2$ GeV/c^2, $|\Delta E| < 0.5$ GeV	◯	◯	◯
charged paritcle	$dr < 0.5$ cm, $|dz| < 5$ cm and $|\vec{p}_{\rm CM}| < 0.2$ GeV/c	◯	◯	◯
charged K	$PID > 0.6$ (for K)	◯	◯	◯
charged π	$PID < 0.9$ (for π)	◯	◯	◯
photon	$33° < \theta_\gamma < 132°$ (barrel part)	×	◯	×
photon	$E_9/E_{25} > 0.95$	◯	◯	◯
photon	π^0/η veto	◯	◯	◯
$K^*\gamma$ veto	see text (only for $B^+ \to K^+\pi^-\pi^+\gamma$)	◯	◯	◯
likelihood ratio	$LR > 0.7$ (for $K^+\pi^-\gamma$), $LR > 0.9$ (for $K^+\pi^-\pi^+\gamma$)	×	×	×
M_{K_X}	$M_{K_X} < 2.4$ GeV/c^2	◯	◯	◯
best candidate	highest C.L. in the K_X vertex fit	×	×	×
B reconstruction	-0.1 GeV $< \Delta E < 0.075$ GeV	×	◯	$\triangle$[A]
B reconstruction	$M_{\rm bc} > 5.27$ GeV/c^2 [B]	×	◯	×

[A]0.1 GeV $< \Delta E < 0.5$ GeV
[B]This selection is not applied when we fit the $M_{\rm bc}$ distribution.

Chapter 5

Analysis of $B^0 \to K^+ \pi^- \gamma$

5.1 $B^0 \to K^+ \pi^- \gamma$ signal

We start the $B^0 \to K^+ \pi^- \gamma$ analysis by looking at the M_{bc} distribution. After applying the selection criteria described in Chapter 4, we select the $K\pi$ invariant mass range 1.2 GeV/c^2 < $M_{K\pi}$ < 2.4 GeV/c^2 to remove the $B^0 \to K^*(892)^0\gamma$ contribution. We also apply the ΔE selection -0.1 GeV < ΔE < 0.075 GeV. The obtained M_{bc} distribution is shown in Fig. 5.1 (a). We perform a binned likelihood fit[1] to the M_{bc} distribution to extract the signal yield. Here, we consider only the signal and $q\bar{q}$ background component. The other background components are basically negligible as described later.

The M_{bc} distribution for the $q\bar{q}$ background is modeled by an empirical function called ARGUS function [24]

$$ f(x) = Nx\sqrt{1 - \left(\frac{x}{E^*_{\mathrm{beam}}}\right)^2} \exp\left[a\left\{1 - \left(\frac{x}{E^*_{\mathrm{beam}}}\right)^2\right\}\right], \tag{5.1} $$

where $x = M_{\mathrm{bc}}$, E^*_{beam} is the beam energy in the CM frame, a is the shape variable and N is the normalization factor. We fix E^*_{beam} at 5.290 GeV. The M_{bc} distribution for the signal is modeled by a Gaussian.

$$ g(x) = \frac{1}{\sqrt{2\pi}\sigma} \exp\left[-\frac{(x-\mu)^2}{2\sigma^2}\right], \tag{5.2} $$

where μ and σ are the mean and width of the Gaussian. The parameter a in the ARGUS function is determined by fitting the M_{bc} distribution with the ΔE sideband data, and is fixed during the subsequent fit. In the same way, μ and σ in the Gaussian are determined by MC and $B^- \to D^0\pi^-$ data, and are fixed. We mention the procedure in detail later. The fit result is overlaid in Fig. 5.1 (a). We find the signal yield to be $54.9\,^{+\,11.2}_{-\,10.6}$ events.

Figure 5.1 (b) shows the $M_{K\pi}$ distribution for events in the signal region. The distribution for the $q\bar{q}$ background obtained from the ΔE sideband data is overlaid in the figure. Here, the distribution is normalized to the number of $q\bar{q}$ events in the signal region obtained from the M_{bc} fit. We can see a clear enhancement around $M_{K\pi} = 1.4$ GeV/c^2. This enhancement indicates the $B^0 \to K_2^*(1430)^0\gamma$ signal, but the $B^0 \to K^*(1410)^0\gamma$ signal can also contribute to

---

[1]In the binned likelihood fit to determine a set of parameters $\boldsymbol{\alpha}$, the likelihood $\mathcal{L}(\boldsymbol{\alpha})$ is calculated by the formula $F(\boldsymbol{\alpha}) \equiv -\ln\mathcal{L} \equiv \sum\{n_i \ln(n_i/\mu_i(\boldsymbol{\alpha})) - (n_i - \mu_i(\boldsymbol{\alpha}))\}$, where n_i and $\mu_i(\boldsymbol{\alpha})$ is the observed and expected number of events in the i'th bin. In this formula, if either n_i or μ_i is 0, the log term is set to 0. In order to determine $\boldsymbol{\alpha}$, we minimize $F(\boldsymbol{\alpha})$ instead of maximizing $\mathcal{L}(\boldsymbol{\alpha})$. The errors of $\boldsymbol{\alpha}$ are calculated in the same way as in the unbinned maximum likelihood fit (Eq. (5.6)).

(a) (b)
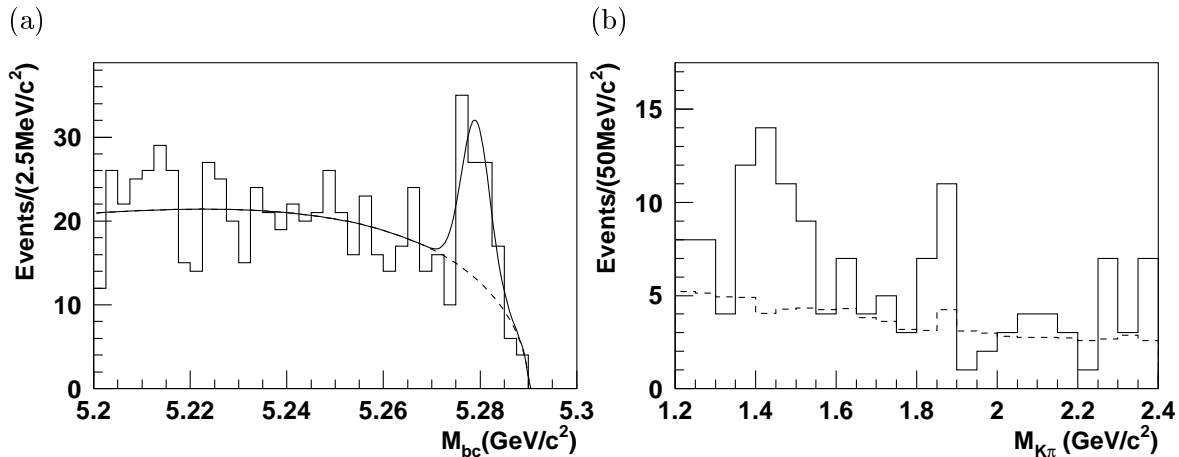
Figure 5.1: (a) M_{bc} distribution for data with $1.2 \text{ GeV}/c^2 < M_{K\pi} < 2.4 \text{ GeV}/c^2$ in the $B^0 \to K^+\pi^-\gamma$ analysis. The fit result is overlaid. (b) $M_{K\pi}$ distribution (solid) for $B^0 \to K^+\pi^-\gamma$. ΔE sideband data normalized using the M_{bc} fit result is overlaid (dashed).

the enhancement. We analyze the region $1.25 \text{ GeV}/c^2 < M_{K\pi} < 1.6 \text{ GeV}/c^2$ to disentangle the signal composition.

We also see an enhancement around $M_{K\pi} = 1.85 \text{ GeV}/c^2$. However, although the background from generic $B\bar{B}$ decays are basically negligible in the $B^0 \to K^+\pi^-\gamma$ analysis as described later, we find the non-negligible background contribution of the decay mode $B^0 \to \bar{D}^0\pi^0$ in this $M_{K\pi}$ region. Indeed, we analyze 10000 events of $B^0 \to \bar{D}^0\pi^0$ MC and find 78 events at $M_{K\pi} = 1.85 \text{ GeV}/c^2$, which corresponds to 2.9 ± 0.7 events for 29.4 fb^{-1} assuming $\mathcal{B}(B^0 \to \bar{D}^0\pi^0) = (3.1 \pm 0.4 \pm 0.5) \times 10^{-4}$ [75]. Therefore, the enhancement can be explained by the background from $B^0 \to \bar{D}^0\pi^0$ and the $q\bar{q}$ background. It should be studied with more data.

5.2 $B^0 \to K^+\pi^-\gamma$ around $M_{K\pi} = 1.4 \text{ GeV}/c^2$

Figure 5.2 (a) shows the M_{bc} vs. ΔE scatter plot for data in $1.25 \text{ GeV}/c^2 < M_{K\pi} < 1.6 \text{ GeV}/c^2$. We can see that data events distribute over the whole area ($M_{\mathrm{bc}} < 5.29 \text{ GeV}/c^2$) of the scatter plot, but we can also see an event concentration in the signal region. Most of the events, especially outside the signal region are consistent with the continuum background shown in Fig. 5.2 (b). Possible contaminations from other background sources[2] are examined using corresponding MC as shown in Fig. 5.2. Most of the $B\bar{B}$ background contributes only to the region $\Delta E < 0.1 \text{ GeV}/c^2$. We expect the contribution of around one event or less from each background to the signal region, and we neglect them.[3]

We extract the signal yield in the region $1.25 \text{ GeV}/c^2 < M_{K\pi} < 1.6 \text{ GeV}/c^2$ from the M_{bc} fit. The M_{bc} distributions for the signal and the $q\bar{q}$ background are modeled by a Gaussian (Eq. (5.2)) and an ARGUS function (Eq. (5.1)), respectively.

The shape variable a of an ARGUS function is determined by fitting the M_{bc} distribution of the ΔE sideband data. To increase the statistics, we do not apply the θ_γ, likelihood ratio and best candidate selection to the ΔE sideband data (Table 4.3). The M_{bc} distribution for the ΔE sideband is shown in Fig. 5.3 (a). As a cross check, we estimate the shape variable a using

---

[2]Cross feed from $b \to s\gamma$ is small and not examined here. It is included in the non-resonant $B^0 \to K^+\pi^-\gamma$ component in the unbinned maximum likelihood fit.

[3]We expect that $B \to K^*(892)\gamma$ background does not affect to the $B^0 \to K_2^*(1430)^0\gamma$ yield because its behaviour should be similar to $B^0 \to K^*(1410)^0\gamma$.

(a) data

(b) $q\bar{q}$ MC ($\times 1.9$)

(c) $B\bar{B}$ MC ($\times 2.4$)

(d) $B \to K^*(892)\gamma$ MC ($\times 14$)
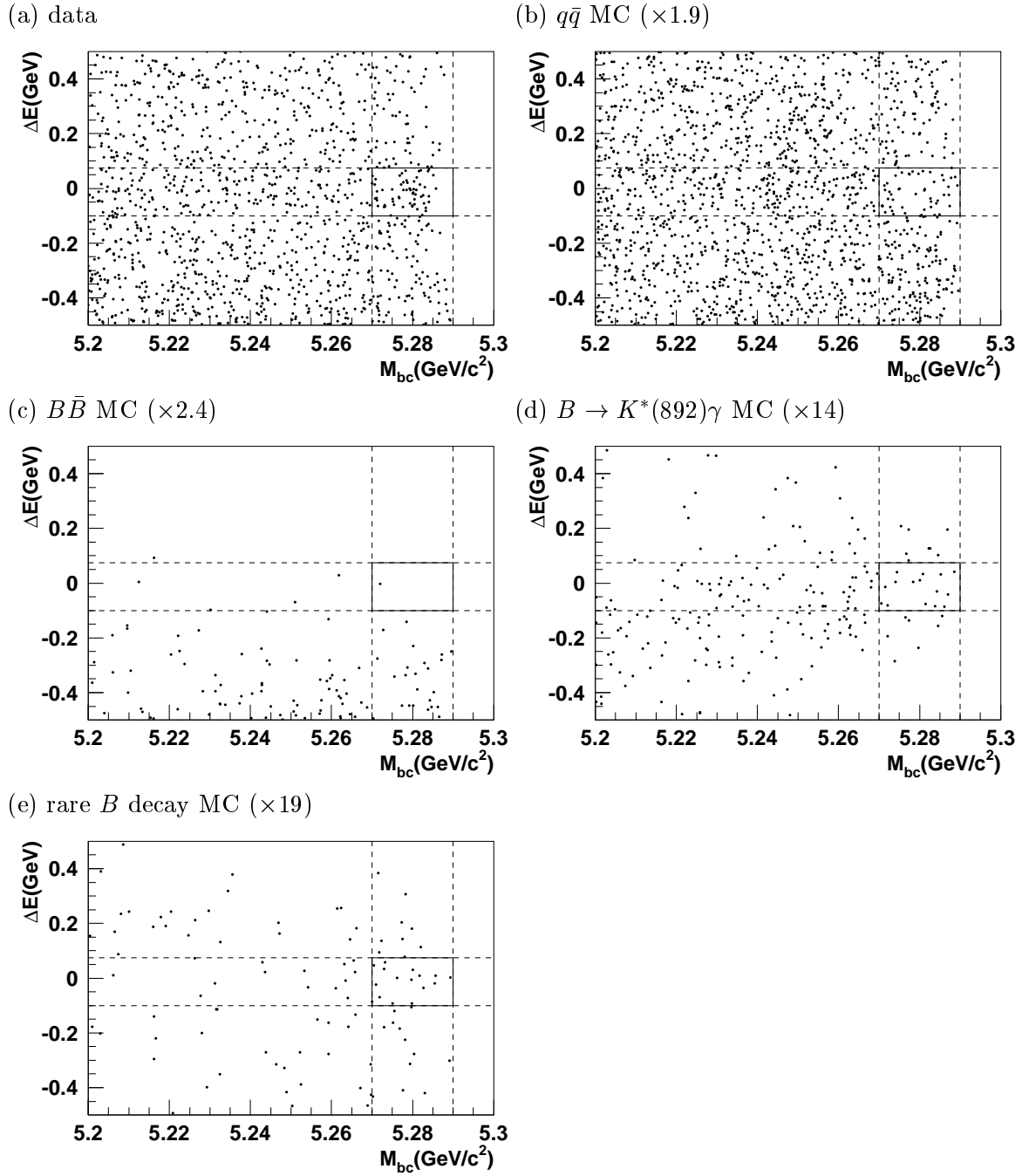
(e) rare B decay MC ($\times 19$)

Figure 5.2: M_{bc} vs. ΔE scatter plots for (a) data, (b) $q\bar{q}$ MC, (c) $B\bar{B}$ MC, (d) $B \to K^*(892)\gamma$ MC and (e) rare B decay MC in the $B^0 \to K^+\pi^-\gamma$ analysis with $1.25 \text{ GeV}/c^2 < M_{K\pi} < 1.6 \text{ GeV}/c^2$. (b) $-$ (e) correspond to 61×10^6, 78×10^6, $(4.5 \pm 0.7) \times 10^8$ and about 6×10^8 $B\bar{B}$ events, respectively.
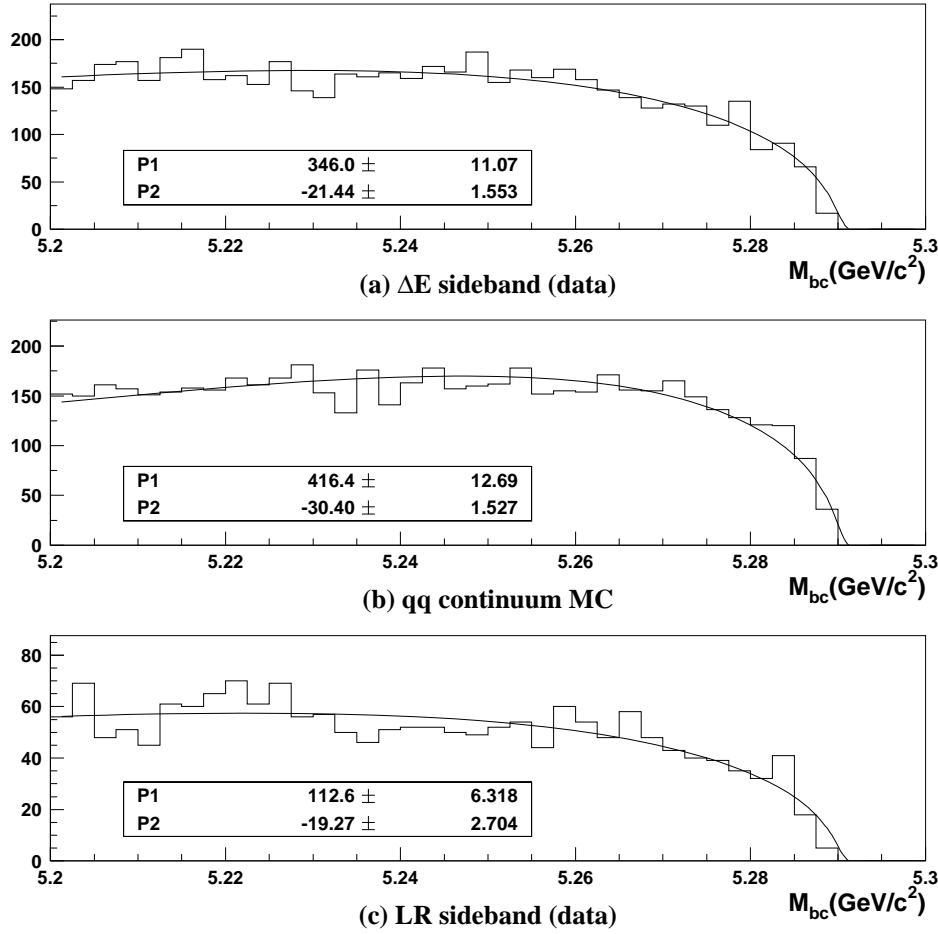
Figure 5.3: M_{bc} distributions in the $B^0 \to K^+\pi^-\gamma$ analysis with 1.25 GeV/$c^2 < M_{K\pi} < 1.6$ GeV/c^2 for (a) the ΔE sideband data, (b) the $q\bar{q}$ MC and (c) the likelihood ratio sideband data. Fit results are overlaid. Parameters P1, P2 are the normalization and shape variable a obtained from the fit, respectively.

the $q\bar{q}$ MC and likelihood ratio sideband ($LR < 0.3$) data as shown in Fig. 5.3. We find small discrepancy between a from the ΔE sideband data and a from the $q\bar{q}$ MC. Possible bias caused by the discrepancy is estimated as a systematic error in the fitting procedure as described later.

The mean μ of a Gaussian is obtained from $B \to D\pi$ data analysis (Fig. 5.4). We obtain $\mu = 5279.1 \pm 0.1$ MeV/c^2 from $B^- \to D^0\pi^-$ data, and $\mu = 5279.4 \pm 0.2$ MeV/c^2 from $B^0 \to D^-\pi^+$ data. We use the value $\mu = 5279.1 \pm 0.3$ MeV/c^2. Here, the central value is taken from $B^- \to D^0\pi^-$ data because the final state of $B^- \to D^0\pi^-$ is similar to that of $B^0 \to K^+\pi^-\gamma$. The error is the quadratic sum of the error from $B^- \to D^0\pi^-$ data and the deviation of the central value of $B^- \to D^0\pi^-$ and $B^0 \to D^-\pi^+$ data.

The width σ of the Gaussian is obtained to be $\sigma = 2.9$ MeV/c^2 from $B^0 \to K_2^*(1430)^0\gamma$ signal MC (Fig. 5.5). The reliability of MC is confirmed using $B \to D\pi$ analysis (Fig. 5.4), where the width is well simulated by MC. We regard the quadratic sum of errors from $B \to D\pi$ and $B^0 \to K_2^*(1430)^0\gamma$ MC as the error for σ. Hence, we use $\sigma = 2.9 \pm 0.1$ MeV/c^2.

The data M_{bc} distribution and the fit result is shown in Fig. 5.6. The signal yield is found to be $27.0^{+7.5}_{-6.8}{}^{+0.8}_{-3.4}$ with a statistical significance of 5.0σ. Here, the significance is defined as $\sqrt{-2\ln(\mathcal{L}(0)/\mathcal{L}_{\max})}$, where $\mathcal{L}_{\max}$ is the maximum of the likelihood and $\mathcal{L}(0)$ is the likelihood

(a) $B^- \to D^0\pi^-$ MC
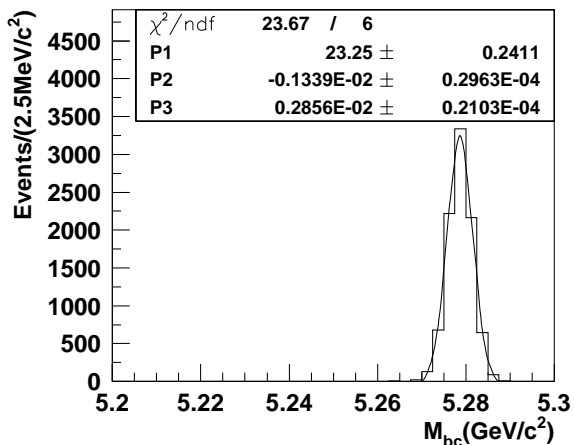
(b) $B^0 \to D^-\pi^+$ MC
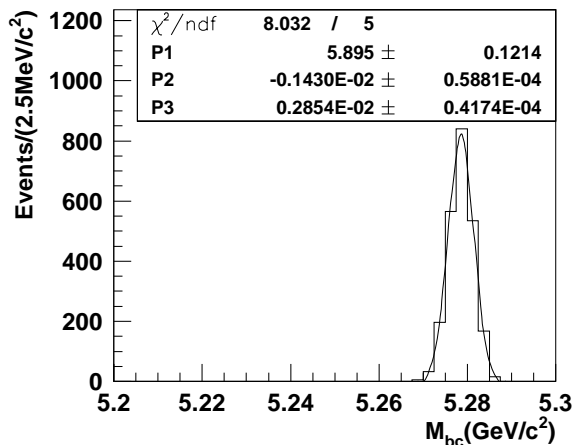
(c) $B^- \to D^0\pi^-$ data
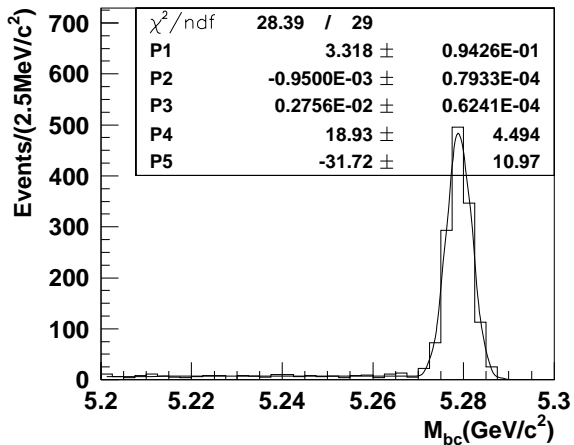
(d) $B^0 \to D^-\pi^+$ data
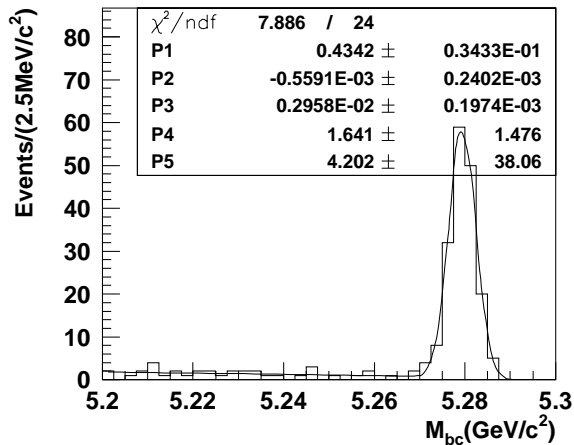
Figure 5.4: M_{bc} distributions for $B \to D\pi$ MC and data. MC distributions are fitted with a Gaussian in 5.27 GeV/c^2 < M_{bc} < 5.29 GeV/c^2. Data distributions are fitted using a sum of a Gaussian and an ARGUS function. The fit values are also shown in the plot, where parameters P1 − P3 are the normalization, mean (difference from 5.28 GeV/c^2) and width of the Gaussian, and P4, P5 are the normalization and shape variable a of the ARGUS function, respectively.

for zero signal yield.[4] This is the first observation of the $B^0 \to K^+\pi^-\gamma$ decay which does not come from $B^0 \to K^*(892)^0\gamma$. The second error of the signal yield is the systematic error in the fitting procedure and is estimated as follows. We vary the value of μ or σ by 1σ and calculate the signal yield for each case by performing the M_{bc} fit. We regard the maximum deviation of the obtained signal yield as a systematic error from the signal shape. Similarly, we vary a by 1σ or to the value obtained from the $q\bar{q}$ MC and likelihood ratio sideband data, and estimate the systematic error from the background shape. The total systematic error in the fitting procedure are the quadratic sum of the two errors. Signal yields in these tests are listed in Table 5.1.

---

[4]If $\mathcal{L}$ is a Gaussian (e.g. when the data sample is large enough), $-\ln\mathcal{L}$ becomes parabolic. Or, in the χ^2 fit (i.e. method of least square), when the fitted function can be written as $f(x) = Nf_1(x, \boldsymbol{\alpha}) + f_2(x, \boldsymbol{\alpha})$, where N ($\boldsymbol{\alpha}$) is the signal yield (other parameters) to be determined, the distribution of χ^2, which corresponds to $-2\ln\mathcal{L}$, is parabolic. In such a case, if the significance of the yield is 5σ, the central value of the yield is away from zero by 5 times of its error. In this case, however, $-\ln\mathcal{L}$ is not parabolic, so we cannot tell the significance from the size of the error.
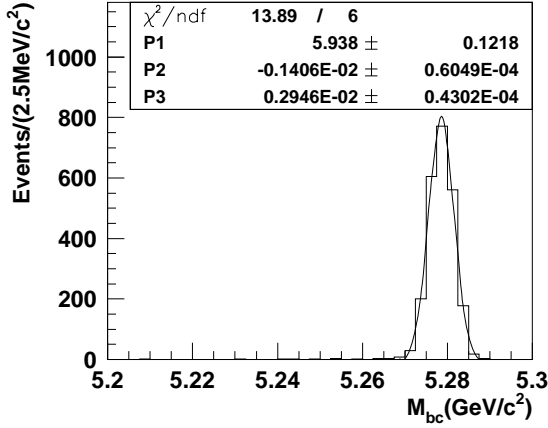
Figure 5.5: M_{bc} distribution for the $B^0 \to K_2^*(1430)^0\gamma$ MC. See the caption of Fig. 5.4 for the fit and parameters.
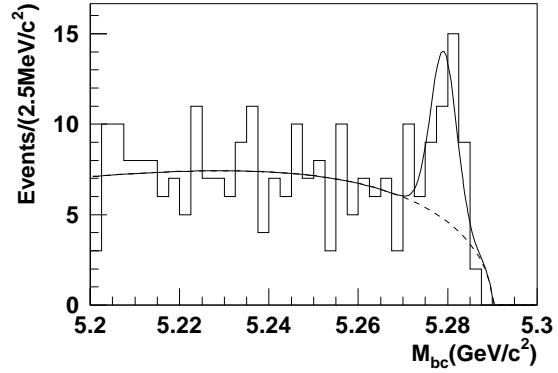
Figure 5.6: M_{bc} distribution for data in the $B^0 \to K^+\pi^-\gamma$ analysis with 1.25 GeV/c^2 < $M_{K\pi}$ < 1.6 GeV/c^2. The fit result is overlaid.

Table 5.1: Breakdown of the systematic error of the $B^0 \to K^+\pi^-\gamma$ yield at 1.25 GeV/c^2 < $M_{K\pi}$ < 1.6 GeV/c^2.

	yield	deviation
standard ($a = -21.4$)	27.0	–
μ ($+0.3$ MeV/c^2)	27.1	$+0.1$
μ (-0.3 MeV/c^2)	26.7	-0.3
σ ($+0.4$ MeV/c^2)	27.3	$+0.3$
σ (-0.4 MeV/c^2)	26.5	-0.5
$a = -19.3$ (LR sideband)	27.7	$+0.7$
$a = -30.4$ ($q\bar{q}$ MC)	23.6	-3.4
total systematic error		$+0.8 - 3.4$

We also estimate the signal yield from the ΔE distribution for the consistency check. Instead of applying the ΔE selection -0.1 GeV < ΔE < 0.075 GeV, we apply the M_{bc} selection $M_{\mathrm{bc}} > 5.27$ GeV/c^2, and then we fit the ΔE distribution. The ΔE shape for the signal is modeled by a Crystal-Ball line shape (CBLS),[5] and that for the $q\bar{q}$ background is modeled by a first order polynomial. We determine the shape of the CBLS using the $B^0 \to K_2^*(1430)^0\gamma$ MC, while the slope of the polynomial is determined from the M_{bc} sideband (5.2 GeV/c^2 < M_{bc} < 5.26 GeV/c^2) data to which the θ_γ, likelihood ratio and best candidate selection are not applied in order to increase the statistics. In the fit, we exclude the region -0.5 GeV < ΔE < -0.2 GeV to avoid the contribution from the $B\bar{B}$ background. The data ΔE distribution and the fit result are shown in Fig. 5.7. We find the signal yield to be $34.9^{+10.9}_{-11.6}$. Considering the MC efficiency of the ΔE selection is 78%, this corresponds to the signal yield of $27.2^{+8.5}_{-9.0}$ in the signal region, which is in good agreement with the signal yield of $27.0^{+7.5}_{-6.8}{}^{+0.8}_{-3.4}$ obtained from the M_{bc} fit.

---

[5]The definition of the CBLS, which is introduced by the Crystal-Ball experiment [76], is

$$f(x) = \begin{cases} A \exp\left(-\frac{1}{2}\left(\frac{x-x_0}{\sigma}\right)^2\right) & (x - x_0 \geq \alpha\sigma) \\ A \exp\left(-\frac{\alpha^2}{2}\right)\left[1 - \frac{\alpha}{N}\frac{x-x_0}{\sigma} - \frac{\alpha^2}{N}\right]^{-N} & (x - x_0 < \alpha\sigma). \end{cases}$$
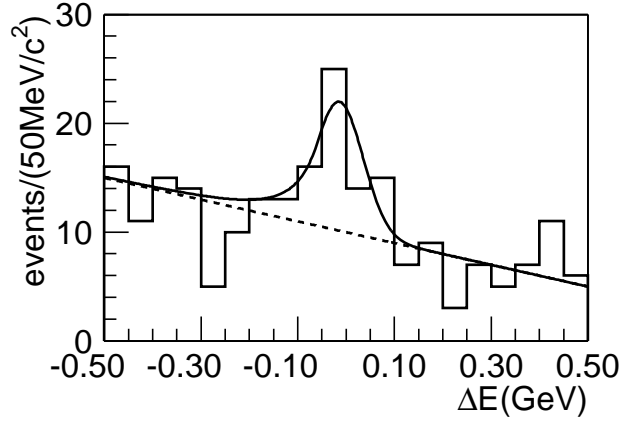
Figure 5.7: ΔE distribution for data with 1.25 GeV/c^2 < $M_{K\pi}$ < 1.6 GeV/c^2 in the $B^0 \to K^+\pi^-\gamma$ analysis. The fit result is overlaid.

5.3 Decomposition of the signal

5.3.1 Overview

The observed signal may be explained as a mixture of three components:[6] $B^0 \to K_2^*(1430)^0\gamma$, $B^0 \to K^*(1410)^0\gamma$ and non-resonant (N.R.) $B^0 \to K^+\pi^-\gamma$. In order to distinguish them, we perform an unbinned maximum likelihood fit to $M_{\rm bc}$, $\cos\theta_{\rm hel}$ and $M_{K\pi}$. Here, the helicity angle $\theta_{\rm hel}$ is defined as

$$\cos\theta_{\rm hel} = -\frac{\vec{p}'_B \cdot \vec{p}'_K}{|\vec{p}'_B||\vec{p}'_K|}, \tag{5.3}$$

where $\vec{p}'_B$ ($\vec{p}'_K$) is the momentum of B (K) in the K_X rest frame.

In the decay $B \to K_2^*(1430)\gamma$, because the photon is polarized, $K_2^*(1430)$ takes the spin states of $J = 2$ and $J_z = \pm 1$, where the direction of the photon is defined as the z axis in the B rest frame. Then, the orbital angular momentum is $L = 2$ and $L_z = \pm 1$ in the decay $K_2^*(1430) \to K\pi$, because K and π are spinless. The angular momentum wave function ψ is $\psi = Y_2^{\pm 1} = \mp\sqrt{15/(8\pi)}\sin\theta\cos\theta e^{\pm i\theta}$. Here, θ is the polar angle in the $K_2^*(1430)$ rest frame measured from the z axis, so θ is identical to $\theta_{\rm hel}$. The angular distribution of the decay is $|\psi|^2 \propto \cos^2\theta_{\rm hel} - \cos^4\theta_{\rm hel}$. Similarly, in the decay $B \to K^*(1410)\gamma$, the helicity angular distribution follows $|Y_1^{\pm 1}|^2 \propto 1 - \cos^2\theta_{\rm hel}$. In the non-resonant decay, the $\cos\theta_{\rm hel}$ distribution is expected to be uniform.[7]

5.3.2 Unbinned maximum likelihood fit

The unbinned maximum likelihood fit is done as follows. Suppose we measure n events with the values $\boldsymbol{x}_i = (x_i^{(1)}, \cdots, x_i^{(d)})$, where $i = 1, \cdots, n$ and we expect that they follow a PDF f which depends on $\boldsymbol{x}$ and a set of parameters $\boldsymbol{\alpha}$ to be determined. The likelihood $\mathcal{L}$ is the product of the probability of each event, and can be written as

$$\mathcal{L}(\boldsymbol{\alpha}) = \frac{1}{n!}\exp\left[-\int f(\boldsymbol{x}, \boldsymbol{\alpha})\,d\boldsymbol{x}\right]\prod_{i=1}^{n} f(\boldsymbol{x}_i, \boldsymbol{\alpha}). \tag{5.4}$$

---

[6]In this study, we do not consider the interference between resonances that is expected to be negligible.

[7]We assume the matrix element of the decay depends only on the photon energy.

We choose $\boldsymbol{\alpha}$ so that $\mathcal{L}(\boldsymbol{\alpha})$ becomes maximum. This is equivalent to minimize

$$F(\boldsymbol{\alpha}) \equiv -\ln \mathcal{L}(\boldsymbol{\alpha}) = \int f(\boldsymbol{x}, \boldsymbol{\alpha}) \, d\boldsymbol{x} - \sum_{i=1}^{n} \ln f(\boldsymbol{x_i}, \boldsymbol{\alpha}), \tag{5.5}$$

where terms independent of $\boldsymbol{x_i}$ and $\boldsymbol{\alpha}$ are dropped out. Once $F(\boldsymbol{\alpha})$ is minimized to F_0 and parameters $\boldsymbol{\alpha}$ are estimated to be $\boldsymbol{\alpha^*}$, we can estimate $\delta\alpha_j$ (the error of parameter α_j) by the formula

$$F_{\min}^{(j)}(\alpha_j^* + \delta\alpha_j) - F_0 = \frac{1}{2}, \tag{5.6}$$

where $F_{\min}^{(j)}(a)$ is the minimum value of $F(\boldsymbol{\alpha})$ when α_j is fixed to a.

What we determine by the unbinned maximum likelihood fit are the signal yields for $B^0 \to K_2^*(1430)^0\gamma$ ($N_{K_2^*}$), $B^0 \to K^*(1410)^0\gamma$ (N_{K^*}), non-resonant $B^0 \to K^+\pi^-\gamma$ ($N_{\mathrm{N.R.}}$) and the $q\bar{q}$ background yield ($N_{q\bar{q}}$). We write the PDF using these parameters:

$$f(\boldsymbol{x}, \boldsymbol{N}) = N_{q\bar{q}} p_{q\bar{q}}^{(1)}(x_1) p_{q\bar{q}}^{(2)}(x_2) p_{q\bar{q}}^{(3)}(x_3) + N_{K_2^*} p_{K_2^*}^{(1)}(x_1) p_{K_2^*}^{(2)}(x_2) p_{K_2^*}^{(3)}(x_3)$$

$$+ N_{K^*} p_{K^*}^{(1)}(x_1) p_{K^*}^{(2)}(x_2) p_{K^*}^{(3)}(x_3) + N_{\mathrm{N.R.}} p_{\mathrm{N.R.}}^{(1)}(x_1) p_{\mathrm{N.R.}}^{(2)}(x_2) p_{\mathrm{N.R.}}^{(3)}(x_3), \tag{5.7}$$

where $\boldsymbol{x} = (x_1, x_2, x_3) = (M_{\mathrm{bc}}, \cos\theta_{\mathrm{hel}}, M_{K\pi})$, and $p^{(1)}(x)$, $p^{(2)}(x)$ and $p^{(3)}(x)$ are the PDF for each component. Therefore, we first determine these 12 PDFs, and then minimize $-\ln \mathcal{L}$.

The PDFs for M_{bc} are already described in Sec. 5.2. We use an ARGUS function for $q\bar{q}$ background, and an identical Gaussian for the three signal components, i.e. $p_{K_2^*}^{(1)}(M_{\mathrm{bc}}) = p_{K^*}^{(1)}(M_{\mathrm{bc}}) = p_{\mathrm{N.R.}}^{(1)}(M_{\mathrm{bc}})$.

5.3.3   PDFs for $\cos\theta_{\mathrm{hel}}$

We determine the $\cos\theta_{\mathrm{hel}}$ PDFs of the signal components from MC. The distributions are shown in Fig. 5.8 (a) – (c). We regard the inclusive $b \to s\gamma$ MC as a non-resonant $B \to K^+\pi^-\gamma$ MC sample. The $\cos\theta_{\mathrm{hel}}$ distributions are distorted due to the non-uniform efficiency. The distributions are fitted with fourth order polynomials, which are used as $\cos\theta_{\mathrm{hel}}$ PDFs. The $\cos\theta_{\mathrm{hel}}$ PDFs of the $q\bar{q}$ background is a fourth order polynomial obtained by fitting the ΔE sideband data. We also obtain a PDF from the $q\bar{q}$ MC for the cross check. They are shown in Fig. 5.8 (d).

In order to check the reliability of MC, we study the discrepancy of the $\cos\theta_{\mathrm{hel}}$ distribution between MC and data using $B^- \to D^0\pi^- \to K^-\pi^+\pi^-$ decay. The selection criteria for $B^- \to D^0\pi^-$ is the same as those for $B^0 \to K^+\pi^-\gamma$ except that γ is replaced by π and that the $M_{K\pi}$ criterion is $|M_{K\pi} - M_{D^0}| < 65$ MeV. We find that the ratio of $\cos\theta_{\mathrm{hel}}$ distribution of data to that of MC for $B^- \to D^0\pi^-$ is uniform as shown in Fig. 5.9, and hence we conclude that the MC simulates well the $\cos\theta_{\mathrm{hel}}$ distribution.

5.3.4   PDFs for $M_{K\pi}$

As for the $M_{K\pi}$ distributions for $B^0 \to K_2^*(1430)^0\gamma$ and $B^0 \to K^*(1410)^0\gamma$, we use a non-relativistic Breit-Wigner distribution

$$f(x) = f_0 \frac{\Gamma^2/4}{(x - M)^2 + \Gamma^2/4}, \tag{5.8}$$

where $x = M_{K\pi}$, M is the nominal mass, and Γ is the total width. In order to take the detector resolution into account, we obtain the distribution from MC, where events are generated

(a) $B^0 \to K_2^*(1430)^0\gamma$ MC

(b) $B^0 \to K^*(1410)^0\gamma$ MC

(c) non-resonant $B^0 \to K^+\pi^-\gamma$ MC

(d) $q\bar{q}$ background (ΔE sideband data)
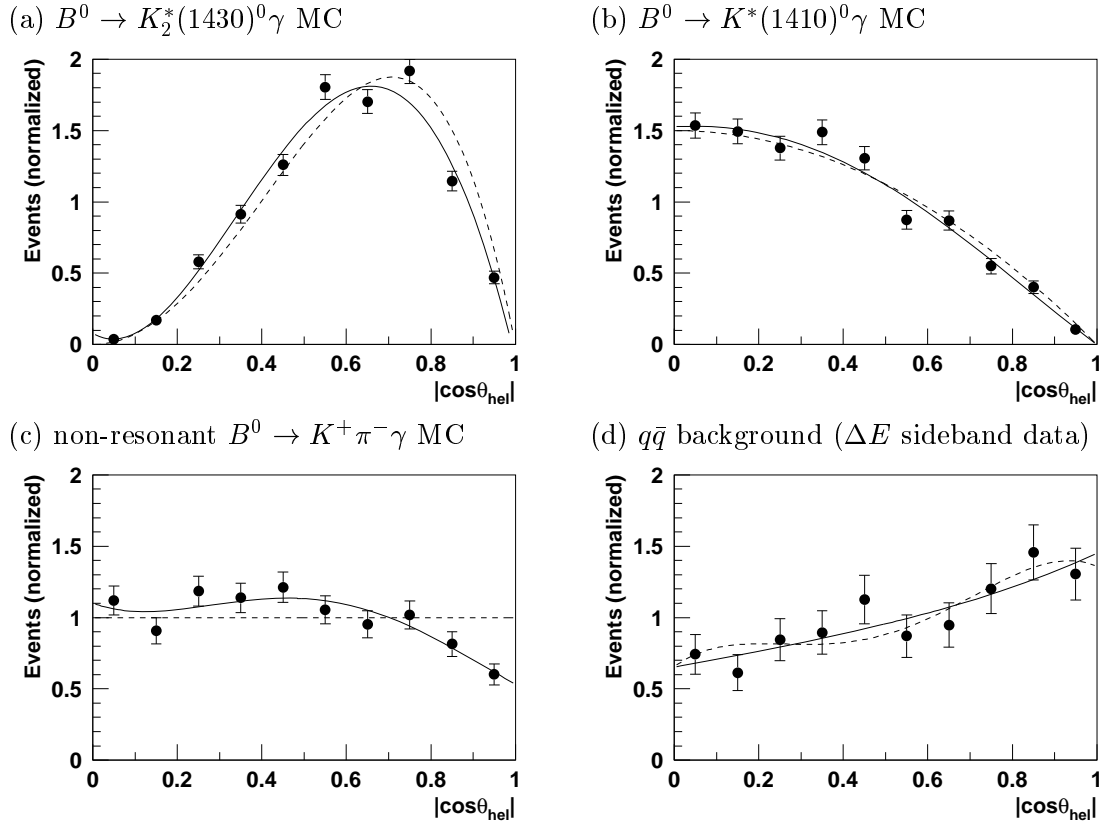
Figure 5.8: $\cos\theta_{\mathrm{hel}}$ distributions (points) and fit results (solid curves) for (a) $B^0 \to K_2^*(1430)^0\gamma$ MC, (b) $B^0 \to K^*(1410)^0\gamma$ MC (c) non-resonant $B^0 \to K\pi\gamma$ MC and (d) ΔE sideband data. Dashed curves shows the theoretical distributions in (a) $-$ (c) and the fit result from $q\bar{q}$ MC in (d).
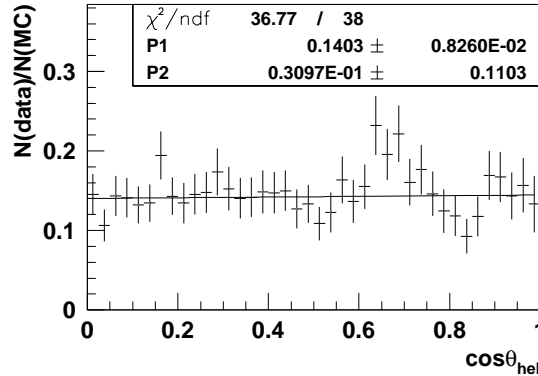
Figure 5.9: Ratio of data $\cos\theta_{\mathrm{hel}}$ distribution to MC $\cos\theta_{\mathrm{hel}}$ distribution for $B^- \to D^0\pi^-$. Fit results to a linear function are also shown. P2 is the obtained slope of the linear function.

(a) $B^0 \to K_2^*(1430)^0\gamma$ MC

(b) $B^0 \to K^*(1410)^0\gamma$ MC

(c) non-resonant $B^0 \to K^+\pi^-\gamma$ MC

(d) $q\bar{q}$ background (ΔE sideband data)
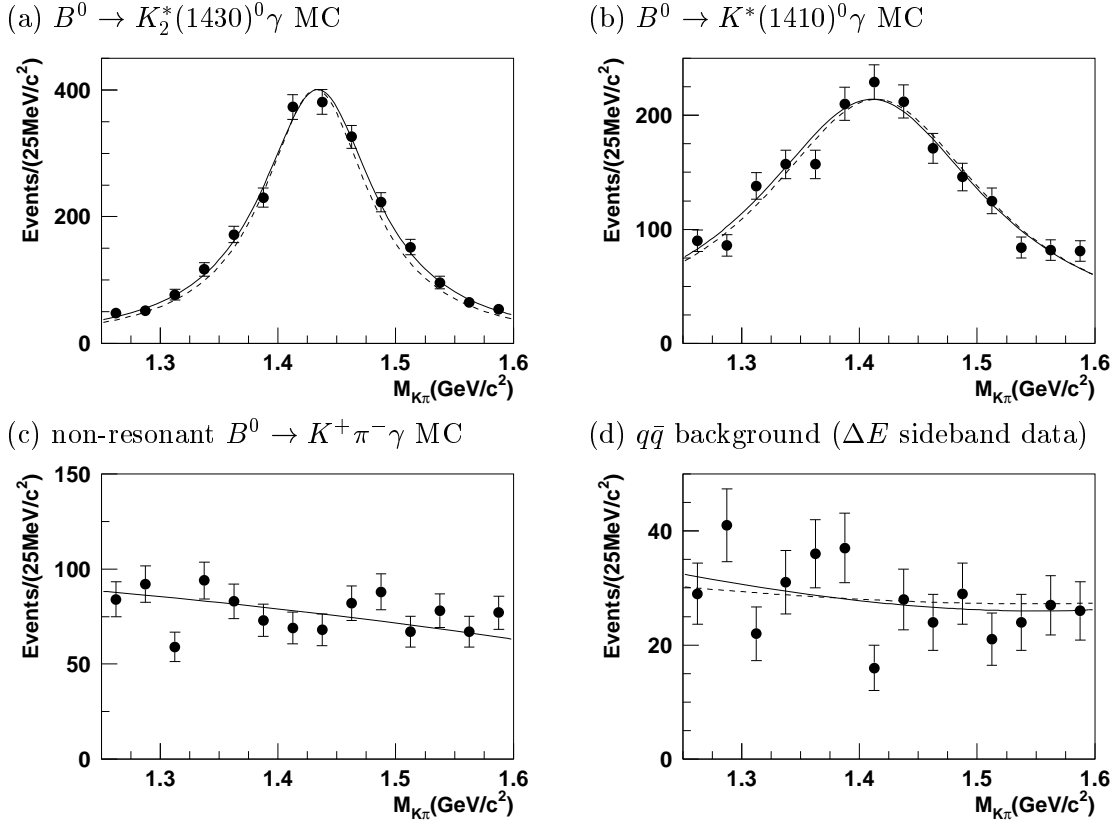
Figure 5.10: $M_{K\pi}$ distributions (points) and fit results (solid curves) for (a) $B^0 \to K_2^*(1430)^0\gamma$ MC, (b) $B^0 \to K^*(1410)^0\gamma$ MC, (c) non-resonant $B^0 \to K\pi\gamma$ MC and (d) data ΔE sideband. Dashed curves shows the original Breit-Wigner distributions in (a) and (b) and the fit result from $q\bar{q}$ MC in (d).

assuming a non-relativistic Breit-Wigner distribution. We find that the MC distribution can be fitted just with a Breit-Wigner function, because the resonance widths are much larger than the detector resolution. We use the fitted Breit-Wigner functions as $M_{K\pi}$ PDFs for $B^0 \to K_2^*(1430)^0\gamma$ and $B^0 \to K^*(1410)^0\gamma$. The distributions and PDFs are shown in Fig. 5.10 (a) and (b).

The PDFs for non-resonant $B^0 \to K^+\pi^-\gamma$ and the $q\bar{q}$ background are determined from the inclusive $b \to s\gamma$ MC and the ΔE sideband data, respectively (Fig. 5.10 (c) and (d)). They are fitted with fourth order polynomials. A fourth order polynomial from the $q\bar{q}$ MC is also used as a PDF for $q\bar{q}$ for a cross check.

It might be more exact to use a relativistic Breit-Wigner function instead of a non-relativistic function. In this case, the amplitude of decays of B to $K\pi\gamma$ through tensor state such as $K_2^*(1430)$ (denoted by r) can be written as [77][8]

$$\mathcal{A}(K\pi\gamma|r) = \frac{F_B F_r}{M_r^2 - M_{K\pi}^2 - i\Gamma_{K\pi}M_r}\left[\left(M_{\pi\gamma}^2 - M_{K\gamma}^2 + \frac{M_B^2(M_K^2 - M_\pi^2)}{M_r^2}\right)^2\right.$$
$$\left. - \frac{1}{3}\left(M_{K\pi}^2 - M_B^2 + \frac{M_B^4}{M_r^2}\right)\left(M_{K\pi}^2 - 2M_K^2 - 2M_\pi^2 + \frac{(M_K^2 - M_\pi^2)^2}{M_r^2}\right)\right]. \quad (5.9)$$

Here, F_B and F_r are form factors, M_r is the nominal mass of the resonance and $\Gamma_{K\pi}$ is the

---

[8]To be exact, this formula is valid only when a pseudo-scaler particle decays to three pseudo-scaler particles, so we might need further modification.
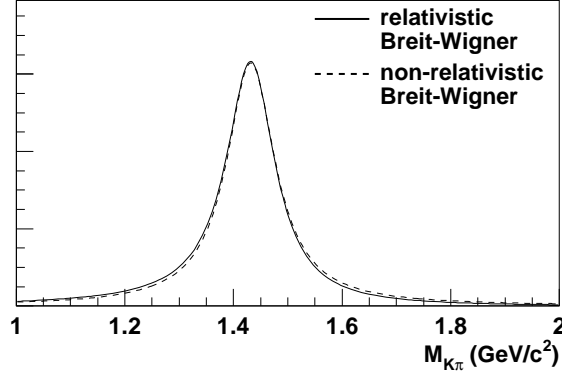
Figure 5.11: Relativistic and non-relativistic Breit-Wigner shapes with nominal $K_2^*(1430)^0$ mass and width.

mass dependent width. The form factors are unknown, but we usually use the Blatt-Weisskopf penetration factors [78]

$$F_r = \begin{cases} 1 & \text{(for spin 0 resonances)} \\ \sqrt{\frac{1+R^2 p_r^2}{1+R^2 p_{AB}^2}} & \text{(for spin 1 resonances)} \\ \sqrt{\frac{9+3R^2 p_r^2+R^4 p_r^4}{9+3R^2 p_{AB}^2+R^4 p_{AB}^4}} & \text{(for spin 2 resonances),} \end{cases} \tag{5.10}$$

where A and B are the daughter particles of r, p_{AB} and p_r are the daughter momenta in the resonance rest frame which are defined as

$$p_{AB} = \frac{\left[(M_{AB}^2 - (M_A + M_B)^2)\,(M_{AB}^2 - (M_A - M_B)^2)\right]^{1/2}}{2M_{AB}} \tag{5.11}$$

$$p_r = \frac{\left[(M_r^2 - (M_A + M_B)^2)\,(M_r^2 - (M_A - M_B)^2)\right]^{1/2}}{2M_r}, \tag{5.12}$$

and R is the meson radius parameter. We choose $R = 1.5\ \hbar c/\text{GeV}$ for $K_2^*(1430)$ similarly to Ref. [77]. The mass dependent width in $r \rightarrow AB$ can be written as

$$\Gamma_{AB} = \Gamma_r \left(\frac{p_{AB}}{p_r}\right)^{2J+1} \left(\frac{M_r}{M_{AB}}\right) F_r^2, \tag{5.13}$$

where Γ_r and J are the nominal width and the spin of the resonance r, respectively. Equation (5.9) has one free variable $M_{\pi\gamma}$ or $M_{K\gamma}$, and must be integrated over the phase space using the relation

$$M_{K\pi}^2 + M_{\pi\gamma}^2 + M_{K\gamma}^2 = M_B^2 - M_K^2 - M_\pi^2. \tag{5.14}$$

Figure 5.11 shows relativistic and non-relativistic Breit-Wigner functions. We find their difference is small, so we use a non-relativistic Breit-Wigner function for PDFs because of its simplicity. We also use relativistic Breit-Wigner function to describe the PDF for $B^0 \rightarrow K_2^*(1430)^0\gamma$ signal as a cross check.

5.3.5 Results

The result of the unbinned maximum likelihood fit is shown in Fig. 5.12. We find $N_{K_2^*} = 21.2\,{}^{+7.6}_{-7.1}$, $N_{K^*} = 7.6\,{}^{+7.1}_{-5.7}$, $N_{\text{N.R.}} = 0.0\,{}^{+4.7}_{-0.0}$ and $N_{q\bar{q}} = 246.2\,{}^{+16.6}_{-16.5}$, where the statistical significance of the $B^0 \rightarrow K_2^*(1430)^0\gamma$ signal is 3.2σ.
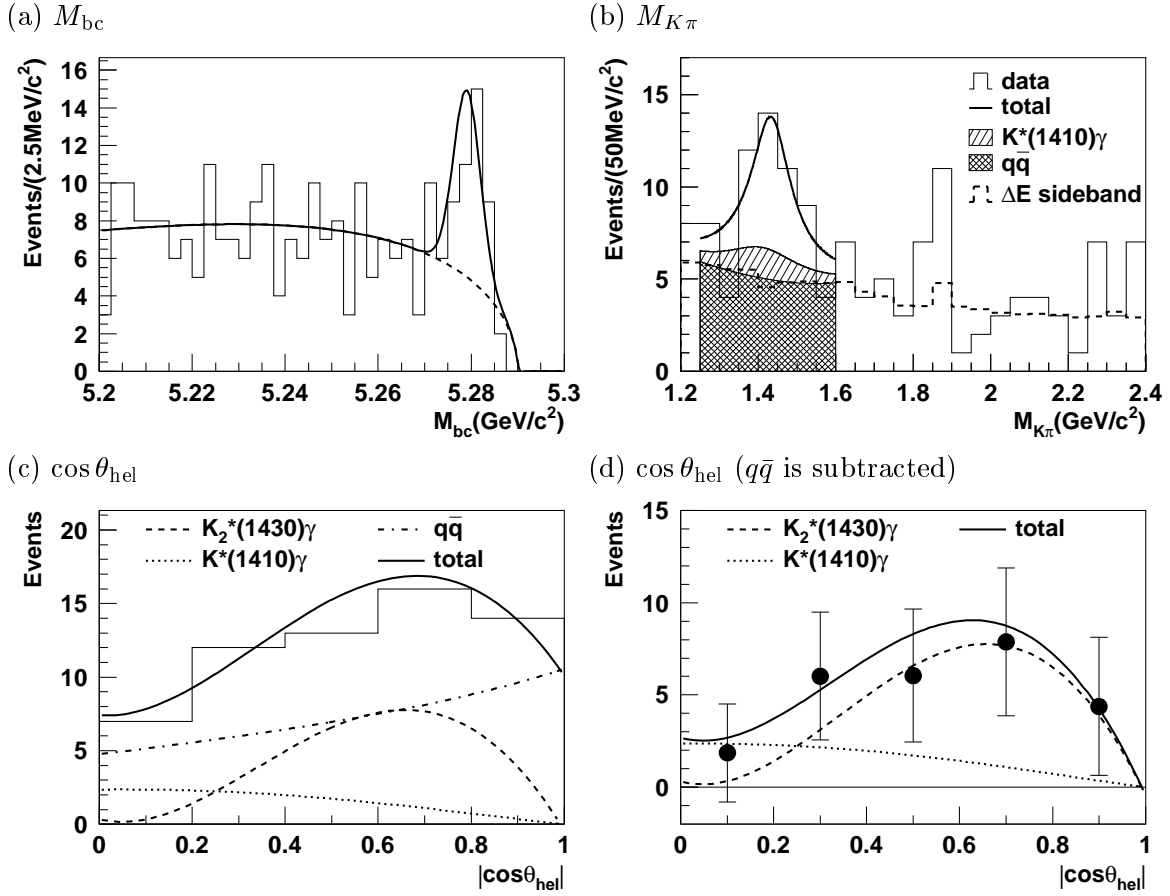
Figure 5.12: (a) M_{bc}, (b) $M_{K\pi}$ and (c), (d) $\cos\theta_{\mathrm{hel}}$ distributions and the unbinned maximum likelihood fit results. The $q\bar{q}$ background is subtracted in (d). $M_{\mathrm{bc}} > 5.27$ GeV/c^2 is applied except in (a), and 1.25 GeV/$c^2 < M_{K\pi} < 1.6$ GeV/c^2 is applied except in (b). In (b), the ΔE sideband data is scaled to the unbinned maximum likelihood fit result and overlaid.

We estimate the systematic error in the fitting procedure in the same way as what we do for the M_{bc} yield. We vary parameters of PDFs one by one (or use a different PDF), and perform the unbinned maximum likelihood fit for each case. Along with μ, σ and a of M_{bc} PDFs, we vary Γ and M of $M_{K\pi}$ PDFs for $B^0 \to K_2^*(1430)^0\gamma$ and $B^0 \to K^*(1410)^0\gamma$ by 1σ. To check the reliability of PDFs for $q\bar{q}$, we also use PDFs from $q\bar{q}$ MC instead of those from the ΔE sideband data. We weight $\cos\theta_{\mathrm{hel}}$ PDFs by the slope obtained from $B^- \to D^0\pi^-$. We also use PDFs from the inclusive $b \to s\gamma$ MC with different b quark mass m_b to test the model dependence of the non-resonant component. Finally, we use the $M_{K\pi}$ PDF for $B^0 \to K_2^*(1430)^0\gamma$ modeled by a relativistic Breit-Wigner function. We assign the largest deviation in several tests for a certain PDF as a systematic error for the PDF, and regard a quadratic sum of them as a systematic error in the fitting procedure. Signal yields for $B^0 \to K_2^*(1430)^0\gamma$ in these tests are listed in Table 5.2.

The $K^*(1410)\gamma$ and non-resonant $K^+\pi^-\gamma$ components are not significant, so we set upper limits. The 90% confidence level (C.L.) upper limit N is calculated from the relation

$$\int_0^N \mathcal{L}(n)dn = 0.9 \int_0^\infty \mathcal{L}(n)dn, \qquad (5.15)$$

where $\mathcal{L}(n)$ is the maximum likelihood with the signal yield fixed at n. To include the systematic

Table 5.2: Breakdown of the yield systematic errors in the fitting procedure for $B^0 \to K_2^*(1430)^0\gamma$.

	yield	deviation
standard ($a = -21.4$)	21.2	—
shape $a = -19.3$ (LR sideband)	21.5	$+0.3$
shape $a = -30.4$ ($q\bar{q}$ MC)	20.1	-1.1
gaussian peak ($+\Delta\mu$)	21.1	-0.1
gaussian peak ($-\Delta\mu$)	21.2	$+0.1$
gaussian width ($+\Delta\sigma$)	21.3	$+0.1$
gaussian width ($-\Delta\sigma$)	21.1	-0.1
$\cos\theta_{\text{hel}}$ for $q\bar{q}$ (MC)	21.6	$+0.4$
$\cos\theta_{\text{hel}}$ for $B \to K\pi\gamma$ ($+$slope)	21.2	$+0.0$
$\cos\theta_{\text{hel}}$ for $B \to K\pi\gamma$ ($-$slope)	21.2	$+0.0$
$\cos\theta_{\text{hel}}$ for $B \to K^*(1410)\gamma$ ($+$slope)	21.0	-0.1
$\cos\theta_{\text{hel}}$ for $B \to K^*(1410)\gamma$ ($-$slope)	21.3	$+0.2$
$\cos\theta_{\text{hel}}$ for $B \to K_2^*(1430)\gamma$ ($+$slope)	21.0	-0.2
$\cos\theta_{\text{hel}}$ for $B \to K_2^*(1430)\gamma$ ($-$slope)	21.3	$+0.2$
$M(K\pi)$ for $q\bar{q}$ (MC)	21.1	-0.1
$M_{K^*(1410)}$ ($+1\sigma$)	21.1	-0.1
$M_{K^*(1410)}$ (-1σ)	21.3	$+0.1$
$\Gamma_{K^*(1410)}$ ($+1\sigma$)	21.3	$+0.1$
$\Gamma_{K^*(1410)}$ (-1σ)	21.1	-0.1
$M_{K_2^*(1430)}$ ($+1\sigma$)	21.2	-0.0
$M_{K_2^*(1430)}$ (-1σ)	21.2	$+0.0$
$\Gamma_{K_2^*(1430)}$ ($+1\sigma$)	21.3	$+0.1$
$\Gamma_{K_2^*(1430)}$ (-1σ)	21.1	-0.1
relativistic Breit-Wigner for $K_2^*(1430)\gamma$	21.0	-0.2
$b \to s\gamma$ MC ($m_b = 4.65$ GeV/c^2)	21.2	$+0.0$
$b \to s\gamma$ MC ($m_b = 4.85$ GeV/c^2)	21.2	$+0.0$
total systematic error		$+0.5 - 1.2$

error from the fit procedure in the yield upper limit, the positive systematic error is added to the limit.

Finally, we obtain

$$N_{K_2^*} = 21.2\,^{+\,7.6}_{-\,7.1}\,^{+\,0.5}_{-\,1.2}$$
$$N_{K^*} = 7.6\,^{+\,7.1}_{-\,5.7}\,^{+\,0.5}_{-\,1.3} < 19.3 \qquad (5.16)$$
$$N_{\text{N.R.}} = 0.0\,^{+\,4.7}_{-\,0.0}\,^{+\,0.0}_{-\,0.0} < 15.3,$$

where the inequality means 90% C.L. upper limit including systematic errors. We conclude that the contribution from the tensor $K_2^*(1430)$ state is dominant in the decay $B^0 \to K^+\pi^-\gamma$ around $M_{K\pi} = 1.4$ GeV/c^2.

Table 5.3: MC efficiencies for $B^0 \to K_2^*(1430)^0\gamma$, $B^0 \to K^*(1410)^0\gamma$ and non-resonant $B^0 \to K^+\pi^-\gamma$ in the $B^0 \to K^+\pi^-\gamma$ analysis. Efficiency for $q\bar{q}$ is also listed for comparison.

Selections	$B^0 \to K_2^*(1430)^0\gamma$	$B^0 \to K^*(1410)^0\gamma$	$B^0 \to K^+\pi^-\gamma$ N.R.
signal reconstruction	0.332 ± 0.003	0.319 ± 0.003	0.499 ± 0.007
dr, $|dz|$ selection	0.929 ± 0.003	0.971 ± 0.002	0.935 ± 0.005
$|\vec{p}^*|$ selection	0.991 ± 0.001	0.998 ± 0.001	0.971 ± 0.003
kaon identification	0.896 ± 0.004	0.871 ± 0.004	0.888 ± 0.006
$\cos\theta_\gamma$	0.894 ± 0.004	0.907 ± 0.004	0.903 ± 0.006
E_9/E_{25}	0.956 ± 0.003	0.960 ± 0.003	0.947 ± 0.005
π^0/η veto	0.886 ± 0.005	0.880 ± 0.005	0.873 ± 0.008
likelihood ratio	0.681 ± 0.007	0.688 ± 0.007	0.696 ± 0.011
best cand. selection	0.878 ± 0.006	0.949 ± 0.004	0.936 ± 0.007
$M_{K\pi}$ selection	0.954 ± 0.004	0.732 ± 0.009	0.966 ± 0.006
Total	0.118 ± 0.002	$(9.84 \pm 0.21) \times 10^{-2}$	0.189 ± 0.005

Selections	$q\bar{q}$
signal reconstruction	$(1.94 \pm 0.01) \times 10^{-4}$
dr, $|dz|$ selection	0.748 ± 0.002
$|\vec{p}^*|$ selection	0.944 ± 0.001
kaon identification	0.637 ± 0.003
$\cos\theta_\gamma$	0.834 ± 0.003
E_9/E_{25}	0.644 ± 0.004
π^0/η veto	0.390 ± 0.005
likelihood ratio	$(8.47 \pm 0.48) \times 10^{-2}$
best cand. selection	0.894 ± 0.018
$M_{K\pi}$ selection	0.190 ± 0.025
Total	$(2.64 \pm 0.38) \times 10^{-7}$

5.4 Efficiency and systematic errors

5.4.1 MC Efficiency

We estimate the reconstruction efficiencies for $B^0 \to K_2^*(1430)^0\gamma$, $B^0 \to K^*(1410)^0\gamma$ and non-resonant $B^0 \to K^+\pi^-\gamma$ from corresponding MC samples. The results are listed in Table 5.3. Here, the sub-decay branching ratio of $K_2^*(1430)^0$ and $K^*(1410)^0$ are not included, but their isospin factor $\mathcal{B}(K_X \to K^+\pi^-)/\mathcal{B}(K_X \to K\pi) = 2/3$ is included in the efficiencies. The efficiency for non-resonant $B^0 \to K^+\pi^-\gamma$ is defined as

$$\epsilon_{\rm MC} = \frac{(\text{number of events reconstructed in } 1.25 \text{ GeV}/c^2 < M_{K\pi} < 1.6 \text{ GeV}/c^2)}{(\text{number of events generated in } 1.25 \text{ GeV}/c^2 < M_{K\pi} < 1.6 \text{ GeV}/c^2)}. \quad (5.17)$$

Then, we calibrate the MC efficiencies with control data sample and assign the systematic errors for categories described in the following subsections.

5.4.2 Photon

The systematic study of the photon reconstruction is performed using radiative Bhabha events $(e^+e^- \to e^+e^-\gamma)$ [79].

We first select radiative Bhabha events with following selection criteria:
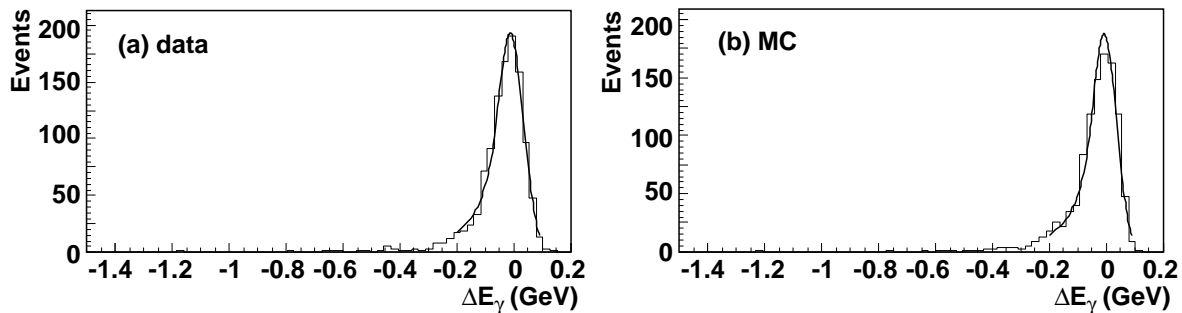
Figure 5.13: Distributions of ΔE_γ for radiative Bhabha data and MC. The distributions are fitted with the CBLS.

- There are only two charged tracks with opposite charges. Each track should be identified as an electron.

- The sum of all the ECL cluster energies in the barrel region is between 11 GeV and 12 GeV in the lab frame.

- The missing momentum vector constructed from two tracks is in the barrel region. The magnitude of the vector in the CM frame is between 2 GeV/c and 3 GeV/c. This range covers energy of photons used in the analysis.

- There is only one good matched cluster in the ECL for the each charged track. The missing momentum vector is more than 20° away from both the tracks. These criteria reduce the contribution of final state radiations and bremmstrahlungs inside the detector.

- The missing mass squared $M_{\mathrm{miss}}^2 = E_{\mathrm{miss}}^{*2} - |\vec{p}_{\mathrm{miss}}^{\,*}|^2$, where E_{miss}^* and $\vec{p}_{\mathrm{miss}}^{\,*}$ are respectively the missing energy and the missing momentum vector calculated in the CM frame, is between -0.3 $(\mathrm{GeV}/c^2)^2$ and 0.2 $(\mathrm{GeV}/c^2)^2$. This selection reduces the contribution of radiative Bhabha events with more than one photons.

Then, we look for a reconstructed photon within the 20° cone around the missing momentum vector. If we find multiple candidates, we select the most energetic one. If the photon is correctly reconstructed, E_{miss}^* should be equal to E_γ^* within the resolution, where E_γ^* is the reconstructed photon energy in the CM frame.

We estimate the photon reconstruction efficiency as the number of events with -0.1 GeV $< \Delta E_\gamma < 0.08$ GeV divided by the number of events that pass the criteria for the radiative Bhabha events, where $\Delta E_\gamma = E_\gamma^* - E_{\mathrm{miss}}^*$. This ΔE_γ selection is chosen based on the ΔE selection in the analysis (-0.1 GeV $< \Delta E < 0.075$ GeV). We estimate the photon reconstruction efficiency both for data and radiative Bhabha MC. The distribution of ΔE_γ is shown in Fig. 5.13. We obtain the efficiency ratio of 1.010 ± 0.020.

To check the possible systematics, we vary the range of the ΔE_γ selection. In addition, we fit the ΔE_γ distribution with the Crystal-Ball line shape, and determine the range of the ΔE_γ selection by the width from the fit result. We also check the efficiency using $E_\gamma^*/E_{\mathrm{miss}}^*$ instead of ΔE_γ. By this procedure, we find 2% systematic uncertainty on the method. By combining the uncertainty with the obtained efficiency ratio, we find the systematic error of photon reconstruction efficiency to be

$$\delta(\epsilon_{\mathrm{data}}^{\mathrm{photon}}/\epsilon_{\mathrm{MC}}^{\mathrm{photon}}) = 0.028. \tag{5.18}$$

Table 5.4: Summary of the tracking efficiency study. The errors are statistical only.

$N_{\text{data}}(\eta \to \pi^+\pi^-\pi^0)/N_{\text{data}}(\eta \to \gamma\gamma)$	0.2685 ± 0.0034
$N_{\text{MC}}(\eta \to \pi^+\pi^-\pi^0)/N_{\text{MC}}(\eta \to \gamma\gamma)$	0.2806 ± 0.0082
$\epsilon_{\text{data}}(\pi^+\pi^-)/\epsilon_{\text{MC}}(\pi^+\pi^-)$	0.9569 ± 0.0306
$\epsilon_{\text{data}}^{\text{single}}/\epsilon_{\text{MC}}^{\text{single}}$	0.9782 ± 0.0153

5.4.3 Track finding

We study the charged tracking efficiency using $\eta \to \pi^+\pi^-\pi^0$ and $\eta \to \gamma\gamma$ decays [80]. The efficiency ratio between data and MC is obtained from

$$\frac{\epsilon_{\text{data}}(\pi^+\pi^-)}{\epsilon_{\text{MC}}(\pi^+\pi^-)} = \frac{N_{\text{data}}(\eta \to \pi^+\pi^-\pi^0)/N_{\text{MC}}(\eta \to \pi^+\pi^-\pi^0)}{N_{\text{data}}(\eta \to \gamma\gamma)/N_{\text{MC}}(\eta \to \gamma\gamma)}, \tag{5.19}$$

where N is the signal yield. Here, the systematics on photon detection is canceled out by taking the ratio. The single tracking efficiency ratio is determined by

$$\frac{\epsilon_{\text{data}}^{\text{single}}}{\epsilon_{\text{MC}}^{\text{single}}} = \sqrt{\frac{\epsilon_{\text{data}}(\pi^+\pi^-)}{\epsilon_{\text{MC}}(\pi^+\pi^-)}}. \tag{5.20}$$

In this study, we do not apply PID to the pions.

To obtain the signal yield, we perform a fit on the η mass distribution. We require the CM momentum of η to be between 2 GeV/c and 2.5 GeV/c, and the photon energy to be greater than 100 MeV. For $\eta \to \pi^+\pi^-\pi^0$ decay, we model the distribution by a double Gaussian and a third order polynomial for signal and background, respectively. The ratio of the widths of the double Gaussian is fixed using MC true events.

For $\eta \to \gamma\gamma$ decay, we use a CBLS and a linear function. The η mass distributions and the fit results for data are shown in Fig. 5.14, and the resulting efficiency ratio are listed in Table 5.4.

The systematic error due to the photon detection is estimated by changing the energy threshold to 200 MeV from 100 MeV or by restricting the photon in the barrel ECL region. We assign 1% uncertainty for the photon detection efficiency. The systematics in the fitting procedure is evaluated by using a lower or higher order polynomial for the fit function, resulting 1% uncertainty. Including a 0.9% uncertainty from the branching ratio $\mathcal{B}(\eta \to \pi^+\pi^-\pi^0)/\mathcal{B}(\eta \to \gamma\gamma) = 0.585 \pm 0.011$ [67][9], we assign a total of 1.7% systematic error to the single track efficiency ratio. Combining this systematic error with the statistical error from the fitting, we obtain the single track efficiency ratio of

$$\epsilon_{\text{data}}^{\text{single}}/\epsilon_{\text{MC}}^{\text{single}} = 0.978 \pm 0.023. \tag{5.21}$$

5.4.4 π identification

The charged pion identification efficiency is checked using $\eta \to \pi^+\pi^-\pi^0$ decay, where the CM momentum of η is required to be greater than 2 GeV/c^2. We obtain the η yields for four cases: no PID is applied to $\pi^\pm$, PID is applied to π^+ only, π^- only, and both of π^+ and π^-. We fit the η mass distribution with a double Gaussian and a third order polynomial, where the ratio of the widths of the double Gaussian is fixed using MC true events.

---

[9]The η branching fractions are updated in PDG2002 [6], resulting the ratio of 0.573 ± 0.009. However, we use the old value, because the result here is the standard value for the Belle experiment.

(a) $\eta \to \pi^+\pi^-\pi^0$ (b) $\eta \to \gamma\gamma$
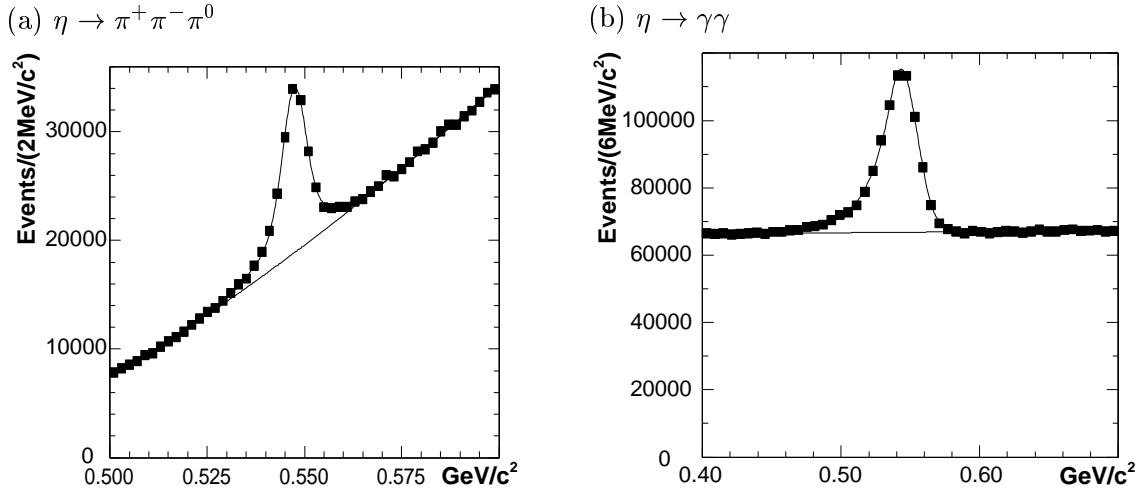
Figure 5.14: η mass distributions for data for (a) $\eta \to \pi^+\pi^-\pi^0$ and (b) $\eta \to \gamma\gamma$.

Table 5.5: Result of the study for charged pion efficiency.

	yield(data)	yield(MC)	data efficiency	ratio
no PID	47087 ± 569	24871 ± 411	—	—
PID +track	45822 ± 518	24350 ± 379	0.973 ± 0.006	0.994 ± 0.009
PID −track	45633 ± 520	24558 ± 381	0.969 ± 0.006	0.982 ± 0.009
PID both	44517 ± 482	24082 ± 361	0.945 ± 0.006	0.976 ± 0.010
combined			0.972 ± 0.003	0.988 ± 0.005

The η mass distributions with and without π identification are shown in Fig. 5.15. The yields and efficiencies are listed in Table 5.5. The error of the efficiency $\delta\epsilon$ is calculated by the formula

$$\delta\epsilon = \frac{1}{n}\left[\sqrt{m\left(1-\frac{n}{m}\right)} \oplus \sqrt{((\delta n)^2 - n)\left(1 - \frac{(\delta n)^2 - n}{(\delta m)^2 - m}\right)}\right], \tag{5.22}$$

where m (n) is the yield before (after) the selection, δm (δn) is its error, and $\oplus$ represents a quadratic sum [81].[10] We obtain three efficiencies ϵ^+, ϵ^- and ϵ^{both} corresponding to the cases with π^+ PID, π^- PID and both PID, respectively. Combining these efficiencies shown in the table, we obtain

$$\epsilon^{\pi\text{ID}}_{\text{data}}/\epsilon^{\pi\text{ID}}_{\text{MC}} = 0.988 \pm 0.005. \tag{5.23}$$

5.4.5 *K* identification

The charged kaon identification efficiency is checked using $\phi \to K^+K^-$ decay, where the CM momentum of ϕ is required to be greater than 3 GeV/c. We obtain the ϕ yield for four cases in the same way as the π identification efficiency. We fit the ϕ mass distribution with a non-relativistic Breit-Wigner function for signal and a third order polynomial for background.

---

[10]This formula can be derived as follows. If there is no background, the error can be written as $\delta\epsilon = \sqrt{n\epsilon(1-\epsilon)}/n$ with $\epsilon = m/n$ from the formula of the binomial distribution. In the case with background events, we can extend it to $\delta\epsilon = \left[\sqrt{n\epsilon(1-\epsilon)} \oplus \sqrt{N_b\epsilon_b(1-\epsilon_b)}\right]/n$, where N_b is the number of background events before the selection and ϵ_b is the efficiency of the selection for background. They can be determined by the relations $\delta n = \sqrt{n + N_b}$ and $\delta m = \sqrt{m + N_b\epsilon_b}$.

(a) data
(b) MC
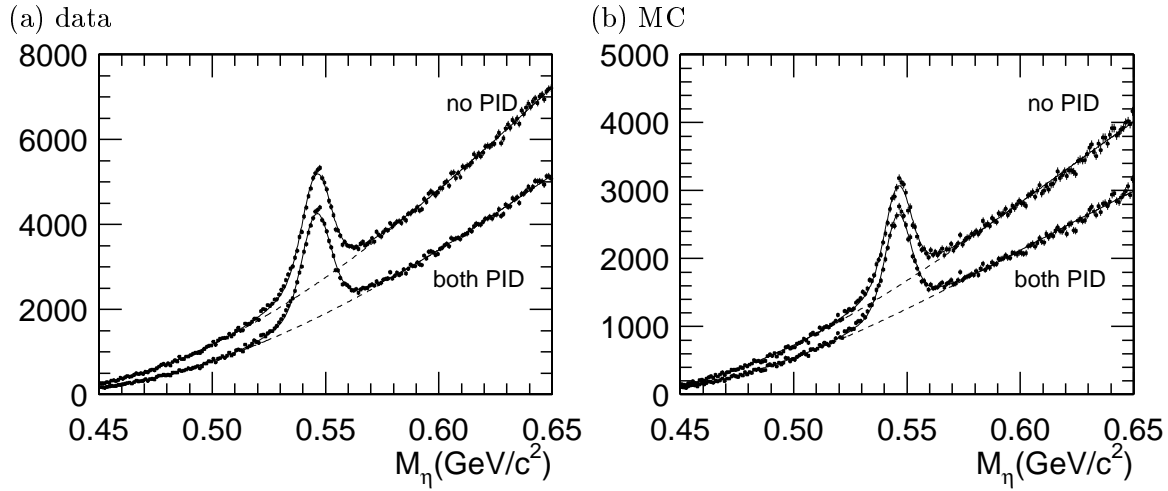
Figure 5.15: $\eta \to \pi^+\pi^-\pi^0$ mass distributions with and without pion identification.

(a) data
(b) MC
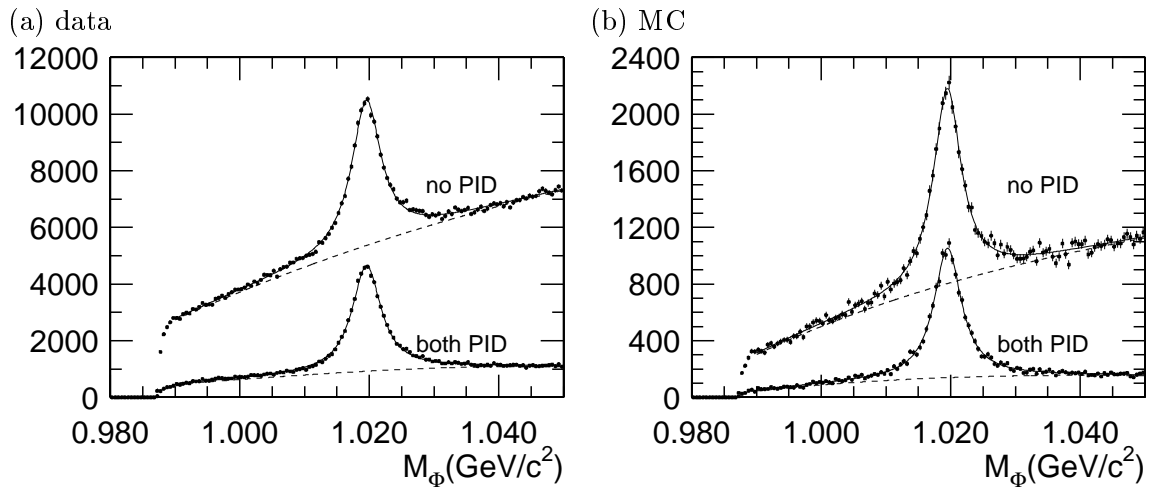
Figure 5.16: $\phi \to K^+K^-$ mass distributions with and without kaon identification.

The ϕ mass distributions with and without K identification are shown in Fig. 5.16. The data/MC ratios are listed in Table 5.6, where the ratios are calculated using the same method as in the π identification. From the table, we obtain

$$\epsilon_{\text{data}}^{\text{KID}}/\epsilon_{\text{MC}}^{\text{KID}} = 1.038 \pm 0.007. \tag{5.24}$$

Table 5.6: Result of the study for charged kaon efficiency.

	yield(data)	yield(MC)	data efficiency	ratio
no PID	31056 ± 459	7827 ± 176	—	—
PID +track	25771 ± 296	6240 ± 118	0.830 ± 0.007	1.041 ± 0.013
PID −track	25449 ± 291	6235 ± 117	0.820 ± 0.007	1.029 ± 0.013
PID both	22222 ± 231	5136 ± 94	0.716 ± 0.006	1.091 ± 0.012
combined			0.832 ± 0.004	1.038 ± 0.006

Table 5.7: Efficiencies (%) for the π^0/η veto, the likelihood ratio (LR) cut and the best candidate selection for the $B^0 \to K^+\pi^-\gamma$ analysis.

	$B^- \to D^0\pi^-$ data	$B^- \to D^0\pi^-$ MC	$B^0 \to K_2^*(1430)^0\gamma$ MC
yield without selections	2422	17028	4385
π^0/η veto	84.8 ± 0.7	85.5 ± 0.3	88.7 ± 0.5
π^0/η veto and LR	59.0 ± 1.0	57.8 ± 0.4	60.6 ± 0.7
all the three selections	55.2 ± 1.0	54.5 ± 0.4	54.0 ± 0.7
relative error (%)	± 1.83	± 0.70	± 1.40

5.4.6 π^0/η veto, likelihood ratio and best candidate selection

We use $B^- \to D^0\pi^- \to K^-\pi^+\pi^-$ decay to check the systematics of the π^0/η veto, the likelihood ratio selection and the best candidate selection efficiency. We reconstruct $B^- \to D^0\pi^-$ requiring the same mass window $M_{K\pi} < 2.4$ GeV/c^2, and apply all the selections (replacing γ to π) used in the $B^0 \to K^+\pi^-\gamma$ analysis except the π^0/η veto, the likelihood ratio selection and the best candidate selection, Then, we apply (a) no further selection, (b) only the π^0/η veto, (c) the π^0/η veto and the likelihood ratio cut, or (d) all the three selections. Here, when we apply the π^0/η veto to $B^- \to D^0\pi^-$, we regard the π^- as a primary photon. Finally, we apply a tight D^0 mass selection 1.84 GeV/$c^2 < M_{K\pi} < 1.89$ GeV/c^2, and estimate the yield.

We perform the procedure both for data and $B^- \to D^0\pi^-$ MC. The $M_{\rm bc}$ distributions are shown in Fig. 5.17. We also perform a similar procedure for $B^0 \to K_2^*(1430)^0\gamma$ MC. To estimate the yield, we fit the $M_{\rm bc}$ distributions with a sum of a Gaussian and an ARGUS function for data, and we count the events in the signal box for MC. The efficiencies for (b) – (d) against (a) are calculated and listed in Table 5.7.[11] We see good agreement between $B^- \to D^0\pi^-$ MC and data for the efficiencies of the three selections, so we do not correct the efficiency. We combine the relative error of $B^- \to D^0\pi^-$ MC and data, and regard it as a systematic error. We find

$$\delta(\epsilon_{\rm data}/\epsilon_{\rm MC}) = 0.020. \tag{5.25}$$

5.4.7 Other corrections

The $M_{K\pi}$ distributions of the signal MC for $B^0 \to K_2^*(1430)^0\gamma$ have a cutoff at 1.23 GeV/c^2 and 1.63 GeV/c^2. The cutoff for $K^*(1410)$ is at 1.04 GeV/c^2 and 1.77 GeV/c^2. However, the tails of the Breit-Wigner shape are expected to reach to $M_{K^+} + M_{\pi^+} = 0.63$ GeV/c^2 in the lower side and to the end-point of the M_{X_s} distribution in the $B \to X_s\gamma$ decay. Therefore, we calculate the correction factor for the cutoff in MC by integrating a Breit-Wigner function. We choose the M_{X_s} end-point to be 3.0 ± 0.5 GeV/c^2, where we regard the error as a systematic error. The correction factors are calculated to be

$$\epsilon_{\rm data}^{\rm BW}/\epsilon_{\rm MC}^{\rm BW} = 0.859 \pm 0.004 \qquad \text{(for } B^0 \to K_2^*(1430)^0\text{)}$$
$$\epsilon_{\rm data}^{\rm BW}/\epsilon_{\rm MC}^{\rm BW} = 0.908 \pm 0.008 \qquad \text{(for } B^0 \to K^*(1410)^0\text{).} \tag{5.26}$$

5.4.8 Summary

Summary of the efficiency corrections based on data and obtained reconstruction efficiencies including the sub-decay branching fractions are listed in Table 5.8.

---

[11]Because the $M_{K\pi}$ mass selection is applied to $B^0 \to K_2^*(1430)^0\gamma$ MC, the efficiency listed here is slightly different from that in Table 5.3.

(a) no selection

(b) π^0/η veto

(c) π^0/η veto and likelihood ratio

(d) all the selections
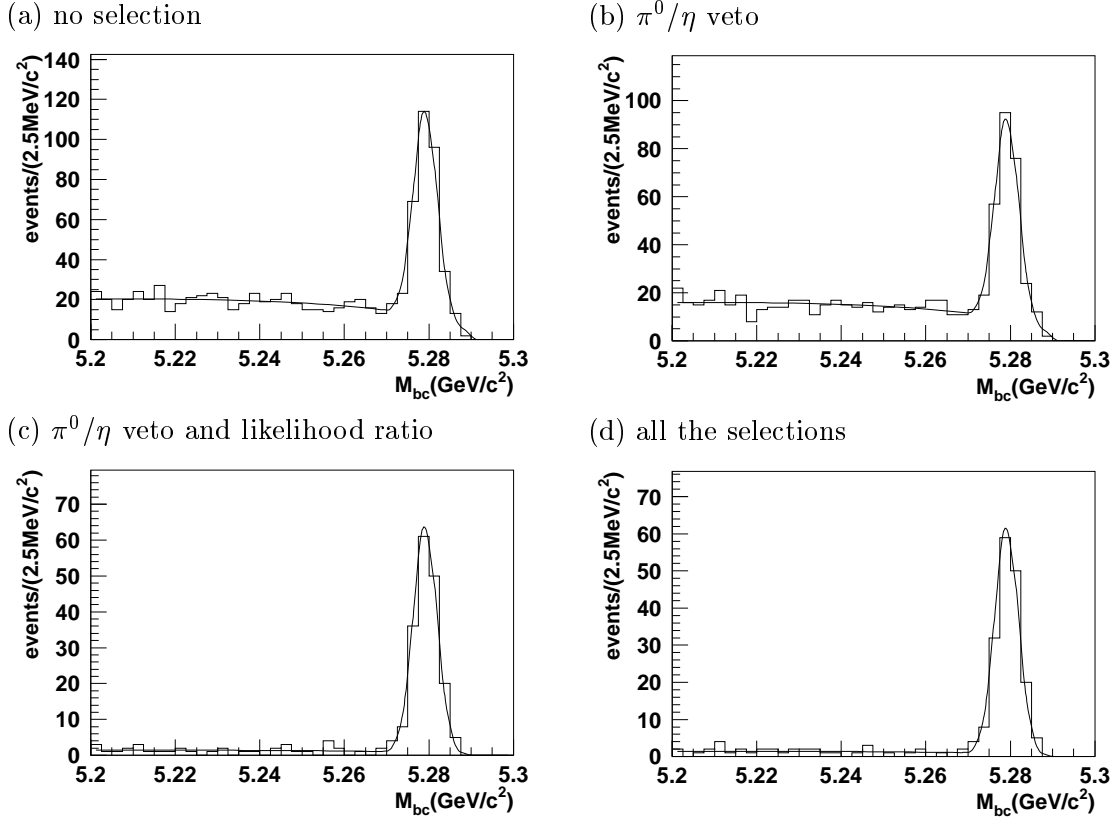
Figure 5.17: M_{bc} distributions for data for $B^- \to D^0\pi^- \to K^-\pi^+\pi^-$ with (a) no selection, (b) the π^0/η veto, (c) the likelihood ratio cut along with (b), and (d) the best candidate selection along with (c). Fit results are overlaid.

Table 5.8: Summary of the efficiency corrections and obtained efficiencies in the $B^0 \to K^+\pi^-\gamma$ analysis.

	$B^0 \to K_2^*(1430)^0\gamma$	$B^0 \to K^*(1410)^0\gamma$	$B^0 \to K^+\pi^-\gamma$ (N.R.)
photon detection	1.000 ± 0.028	1.000 ± 0.028	1.000 ± 0.028
tracking	0.957 ± 0.045	0.957 ± 0.045	0.957 ± 0.045
K identification	1.038 ± 0.007	1.038 ± 0.007	1.038 ± 0.007
π identification	0.988 ± 0.005	0.988 ± 0.005	0.988 ± 0.005
π^0/η, LR, best candidate	1.000 ± 0.020	1.000 ± 0.020	1.000 ± 0.020
Breit-Wigner shape	0.859 ± 0.004	0.908 ± 0.008	—
efficiency correction	0.843 ± 0.050	0.891 ± 0.053	0.981 ± 0.058
MC efficiency	$(11.8 \pm 0.2)\%$	$(9.8 \pm 0.2)\%$	$(18.9 \pm 0.5)\%$
sub-decay branching	0.499 ± 0.012	0.066 ± 0.013	—
efficiency	$(4.97 \pm 0.33)\%$	$(0.58 \pm 0.12)\%$	$(18.6 \pm 1.2)\%$

5.5 Branching Fractions

The branching fractions are obtained from the number of $B\bar{B}$ in Eq. (4.2), the signal yields in Eq. (5.16) and the efficiencies listed in Table 5.8. We obtain

$$\mathcal{B}(B^0 \to K_2^*(1430)^0\gamma) = (1.33\,^{+\,0.48\,+\,0.09}_{-\,0.45\,-\,0.11}) \times 10^{-5} \tag{5.27}$$

$$\mathcal{B}(B^0 \to K^*(1410)^0\gamma) < 13.2 \times 10^{-5} \qquad (90\%\ \text{C.L.}) \tag{5.28}$$

$$\mathcal{B}(B^0 \to K^+\pi^-\gamma(\text{N.R.})) < 0.26 \times 10^{-5} \qquad (90\%\ \text{C.L.}). \tag{5.29}$$

Here, in the calculation of the upper limit of the branching fractions, we conservatively reduce the efficiency and the number of $B\bar{B}$ by one standard deviation. We also calculate the total branching fraction of $B^0 \to K^+\pi^-\gamma$ at $1.25\ \text{GeV}/c^2 < M_{K\pi} < 1.6\ \text{GeV}/c^2$ for completeness. The efficiency is calculated to be $(18.4 \pm 1.7)\%$ by weighting the efficiency of the three components with measured yields. Using the signal yield from the M_{bc} fit, the total branching fraction is calculated to be $(0.46\,^{+\,0.13\,+\,0.05}_{-\,0.12\,-\,0.07}) \times 10^{-5}$.

The measured branching fraction of $B^0 \to K_2^*(1430)^0\gamma$ is consistent with recent predictions [20, 21]. This is also consistent with the measurement by CLEO (Eq. (2.13)).

Chapter 6

Analysis of $B^+ \to K^+\pi^-\pi^+\gamma$

6.1 $B^+ \to K^+\pi^-\pi^+\gamma$ signal

In the $B^+ \to K^+\pi^-\pi^+\gamma$ analysis, we reconstruct B mesons by combining a high energy photon with a K_X system which is formed from $K^+\pi^-\pi^+$ with $M_{K\pi\pi} < 2.4$ GeV/c^2. Backgrounds in this analysis are categorized as shown in Fig. 6.1. The biggest background comes from (A) the $q\bar{q}$ continuum. It is treated in the same way as for $B^0 \to K^+\pi^-\gamma$. The rest of the background stems from various B decays. As shown in the figure, they are further classified into 3 types: (B) the $B\bar{B}$ principal decay (which goes through the $b \to c$ decay) that are identified to have $K^+\pi^-\pi^+\gamma$ final states, (C) the $b \to s\gamma$ decay,[1] and (D) the rare B decays which goes through the $b \to u$ transition. Figure 6.2 shows the $M_{\rm bc}$ vs. ΔE scatter plot for data and MC of possible background sources. To estimate the $b \to s\gamma$ cross feed, events generated with $K^+\pi^-\pi^+\gamma$ final state are excluded beforehand from the inclusive $b \to s\gamma$ MC. Contrary to the $B^0 \to K^+\pi^-\gamma$ analysis, contributions from (B) $B\bar{B}$ decays and (C) $b \to s\gamma$ cross feed (including $B \to K^*(892)\gamma$)[2] are not negligible. The rare B decays (D) are negligible as in the $B^0 \to K^+\pi^-\gamma$ analysis.

The signal yield is extracted from the $M_{\rm bc}$ fit.[3] In addition to the signal and the $q\bar{q}$ back-

---

[1]It consists of (C-1) $B \to K^*(892)\gamma$ and (C-2) inclusive $b \to s\gamma$ decays in which $B \to K^*(892)\gamma$ is not included.

[2]Resonant decays $B \to K_X\gamma$ are not considered in the inclusive $b \to s\gamma$ MC. However, we can estimate the cross feed because most of the cross feed comes from decays with more than two pions such as $B^+ \to K^+\pi^-\pi^+\pi^0\gamma$ and $B^0 \to K^+\pi^-\pi^+\pi^-\gamma$ for which resonant decays do not contribute.

[3]We apply $M_{K\pi} < 1.7$ GeV/c^2 and $M_{\pi\pi} < 1.7$ GeV/c^2 for the consistency with the analysis afterwards. These requirements remove events only slightly.
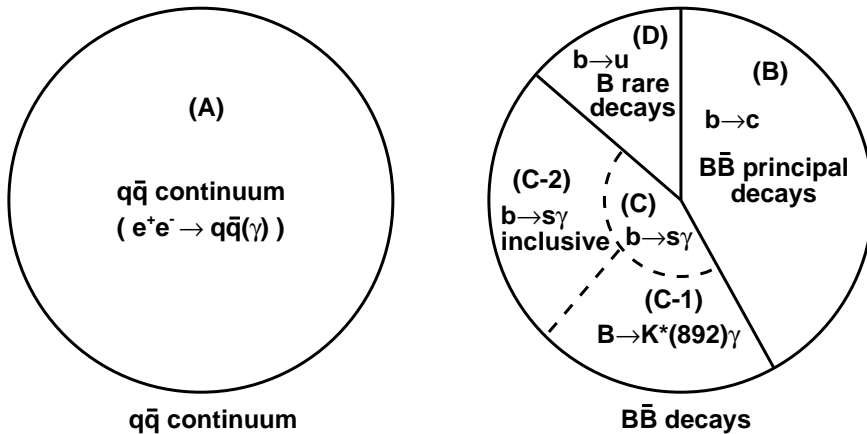
Figure 6.1: Category of backgrounds in $B^+ \to K^+\pi^-\pi^+\gamma$.
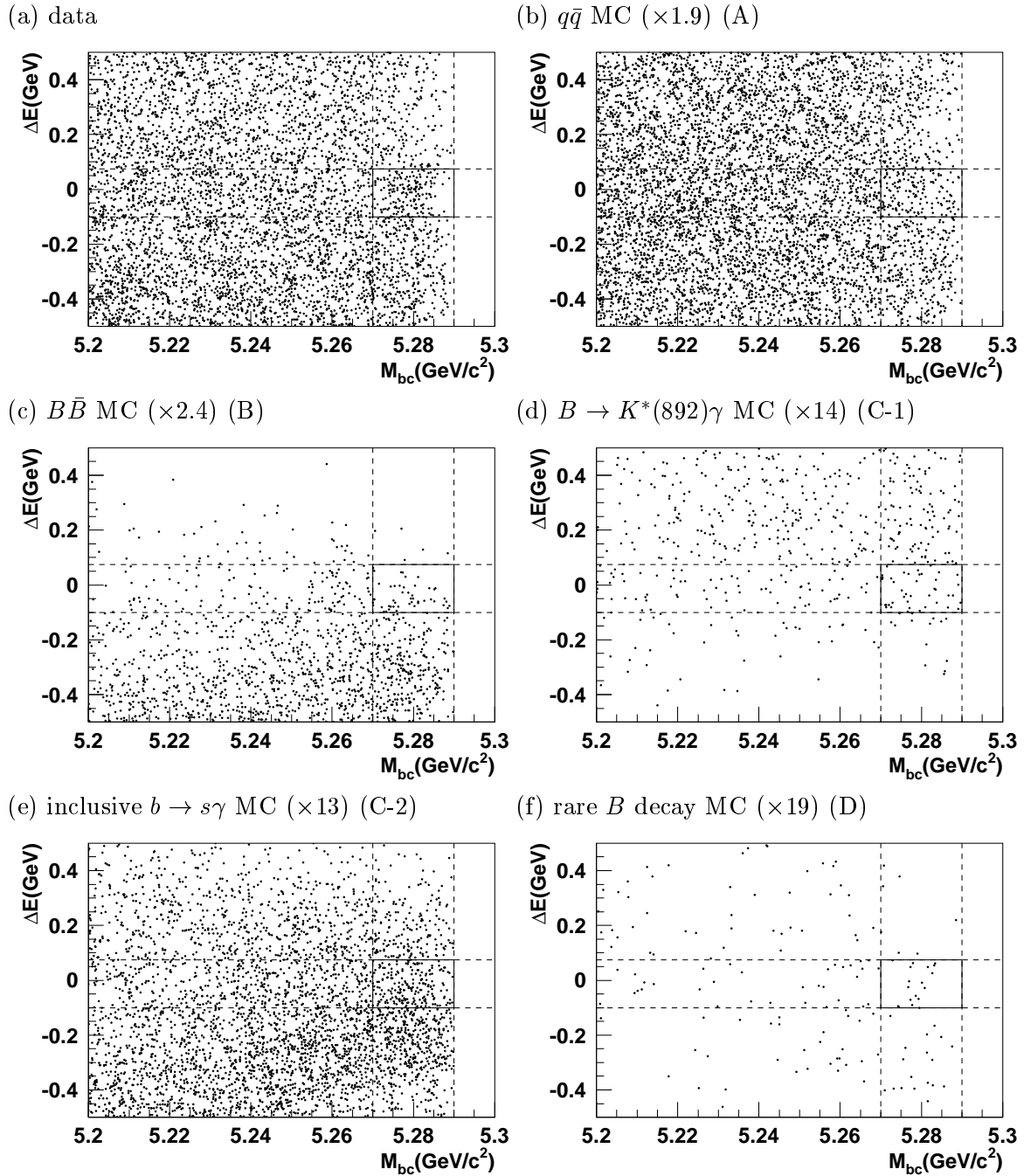
Figure 6.2: M_{bc} vs. ΔE scatter plots for (a) data, (b) $q\bar{q}$ MC, (c) $B\bar{B}$ MC, (d) $B \to K^*(892)\gamma$ MC (e) inclusive $b \to s\gamma$ MC except $B \to K^*(892)\gamma$ and (f) rare B decay MC in the $B^+ \to K^+\pi^-\pi^+\gamma$ analysis. (b) $-$ (f) correspond to 61×10^6, 78×10^6, $(4.5 \pm 0.7) \times 10^8$, $(4.1 \pm 1.1) \times 10^8$ and about 6×10^8 $B\bar{B}$ events respectively. In (d), events generated with the $K^+\pi^-\pi^+\gamma$ final state are excluded.
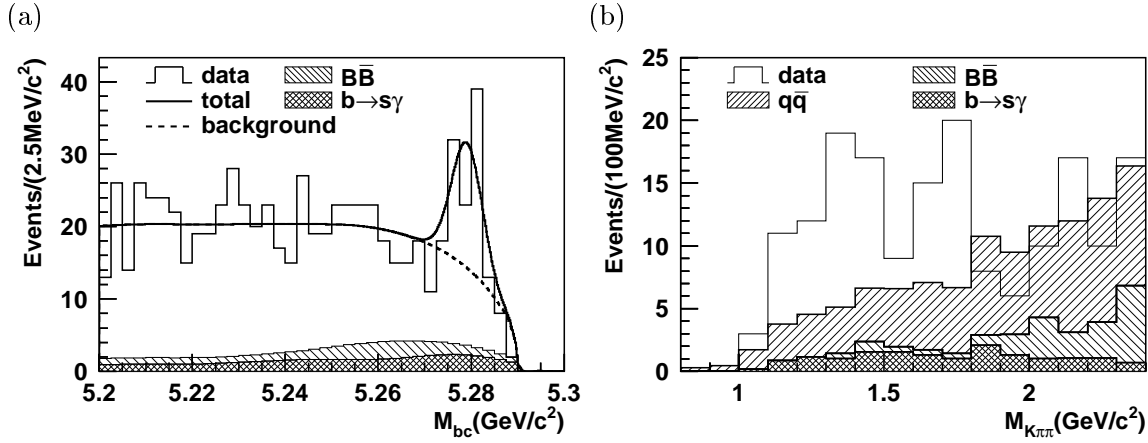
Figure 6.3: (a) M_{bc} and (b) $M_{K\pi\pi}$ distributions for data in the $B^+ \to K^+\pi^-\pi^+\gamma$ analysis. M_{bc} fit result is overlaid in (a). In (b), $M_{\mathrm{bc}} > 5.27$ GeV/c^2 is applied. The distribution for $q\bar{q}$ is obtained from the ΔE sideband data and is normalized to the number of $q\bar{q}$ events in the signal region obtained from the M_{bc} fit.

ground component (A), the $B\bar{B}$ background (B) and the $b \to s\gamma$ cross feed (C) are included in the fit with fixed normalizations scaled to the luminosity. We use smoothed MC to model M_{bc} shapes of the $B\bar{B}$ background and the $b \to s\gamma$ cross feed. The normalization of the $b \to s\gamma$ cross feed is determined based on the present world average of $\mathcal{B}(B \to X_s\gamma)$ (Eq. (2.12)). The signal M_{bc} distribution is modeled by a Gaussian (Eq. (5.2)). We use $\mu = 5279.1 \pm 0.3$ MeV/c^2, which is the same as in the $B^0 \to K^+\pi^-\gamma$ analysis, and $\sigma = 3.3 \pm 0.1$ MeV/c^2 which is obtained from $B^+ \to K^*(1680)^+\gamma \to K^*\pi\gamma$ signal MC and confirmed by $B^0 \to D^-\pi^+ \to K^+\pi^-\pi^-\pi^+$. The M_{bc} distribution for $q\bar{q}$ is modeled by an ARGUS function (Eq. (5.1)), where the shape variable a is determined in the same way as $B^0 \to K^+\pi^-\gamma$ (Sec. 5.2).[4]

The M_{bc} distribution for data is shown in Fig. 6.3 (a) together with the fit result. We find the signal yield of $57.2^{+11.8}_{-11.1}{}^{+6.4}_{-1.9}$ with a statistical significance of 5.9σ. This is the first observation of the radiative B decay to the $K^+\pi^-\pi^+\gamma$ final state. The method to obtain the systematic error in the fitting procedure is same as in the $B^0 \to K^+\pi^-\gamma$ analysis. We also test the fit result by varying the normalization of the $b \to s\gamma$ cross feed by 1σ, by using the inclusive $b \to s\gamma$ MC with different m_b, or by floating one of the fixed normalizations. The results of these evaluations are listed in Table 6.1.

The $M_{K\pi\pi}$ distribution for events in the signal region is shown in Fig. 6.3 (b). Here, the distribution for $q\bar{q}$ is obtained from the ΔE data sideband and normalized to the number of $q\bar{q}$ events in the signal region obtained from the M_{bc} fit. We observe no signal excess at $M_{K\pi\pi} > 1.8$ GeV/c^2. Considering that there are no kaonic resonance at $M_{KX} > 2.4$ GeV/c^2, and that the theoretical M_{X_s} distribution in $B \to X_s\gamma$ has broad structure around $M_{X_s} = 2$ GeV/c^2, we expect that the selection $M_{K\pi\pi} < 2.4$ GeV/c^2 does not remove a part of the signal.

---

[4]The contribution to the ΔE sideband data by the cross feed from the $b \to s\gamma$ decays is very small, because we do not apply the likelihood ratio selection to the ΔE sideband. The contamination of $B\bar{B}$ background to the ΔE sideband is negligible as shown in Fig. 6.2 (c).

Table 6.1: Breakdown of the yield systematic errors for $B^+ \to K^+\pi^-\pi^+\gamma$.

	yield	difference
standard ($a = -16.9$)	57.19	—
shape $a = -16.4$ ($+1\sigma$)	57.61	$+0.41$
shape $a = -26.7$ ($q\bar{q}$ MC)	56.78	-0.42
gaussian peak ($+\Delta\mu$)	56.80	-0.39
gaussian peak ($-\Delta\mu$)	57.27	$+0.08$
gaussian width ($+\Delta\sigma$)	57.38	$+0.19$
gaussian width ($-\Delta\sigma$)	56.94	-0.25
$b \to s\gamma$ MC normalization ($+1\sigma$)	55.43	-1.76
$b \to s\gamma$ MC normalization (-1σ)	59.00	$+1.81$
$b \to s\gamma$ MC ($m_b = 4.65$ GeV/c^2)	57.89	$+0.70$
$b \to s\gamma$ MC ($m_b = 4.85$ GeV/c^2)	56.09	-1.11
floating number of $b \to s\gamma$	63.55	$+6.35$
floating number of $B\bar{B}$	59.23	$+2.04$
total systematic error		$+6.37 - 1.85$

6.2 Decomposition of the signal

6.2.1 Overview

The observed signal may consist of a sum of radiative B decays through kaonic resonances such as $B^+ \to K_1(1270)^+\gamma$ and $B^+ \to K^*(1680)^+\gamma$. Non-resonant $B^+ \to K^{*0}\pi^+\gamma$, $B^+ \to K^+\rho^0\gamma$ and $B^+ \to K^+\pi^-\pi^+\gamma$ should also be considered. Due to the existence of too many kaonic resonances, it is difficult to decompose the resonant substructure with the current statistics. However, since kaonic resonances mostly decay to $K^+\pi^-\pi^+$ final state through $K^{*0}\pi$ and $K^+\rho$, we attempt to decompose the $B^+ \to K^+\pi^-\pi^+\gamma$ signal into $K^{*0}\pi\gamma$, $K^+\rho^0\gamma$ and non-resonant $K^+\pi^-\pi^+\gamma$ components.

Figure 6.4 shows $M_{K\pi}^2$ vs. $M_{\pi\pi}^2$ scatter plots of the $B^+ \to K^+\pi^-\pi^+\gamma$ candidate event in the signal region for data and $q\bar{q}$ MC. We define two selections for convenience:

- "K^* mass cut" is defined as

$$|M_{K\pi} - M_{K^{*0}}| < 75 \text{ MeV}/c^2 \tag{6.1}$$

- "ρ mass cut" is defined as

$$|M_{\pi\pi} - M_\rho| < 250 \text{ MeV}/c^2 \quad \text{and} \quad |M_{K\pi} - M_{K^{*0}}| > 125 \text{ MeV}/c^2, \tag{6.2}$$

with $M_{K^{*0}} = 892$ MeV/c^2 and $M_\rho = 771$ MeV/c^2. These are to select $B^+ \to K^{*0}\pi^+\gamma$ and $B^+ \to K^+\rho^0\gamma$ events. The allowed regions for the K^* and ρ mass cut are shown by the solid and dashed lines in Fig. 6.4. We can see that data events concentrate in these regions compared to $q\bar{q}$ MC events.

We perform an unbinned maximum likelihood fit to M_{bc}, $M_{K\pi}$ and $M_{\pi\pi}$ assuming that the signal events are composed of $K^{*0}\pi^+\gamma$, $K^+\rho^0\gamma$ and non-resonant $K^+\pi^-\pi^+\gamma$. Here, we make an approximation that the correlation between $M_{K\pi}$ and $M_{\pi\pi}$ is small.[5] In addition to the $q\bar{q}$ background component (A), we include the components from the $B\bar{B}$ background (B) and the

---

[5]As far as the signal and $q\bar{q}$ background MCs, the $M_{K\pi}$ and $M_{\pi\pi}$ distributions do not depend on each other.
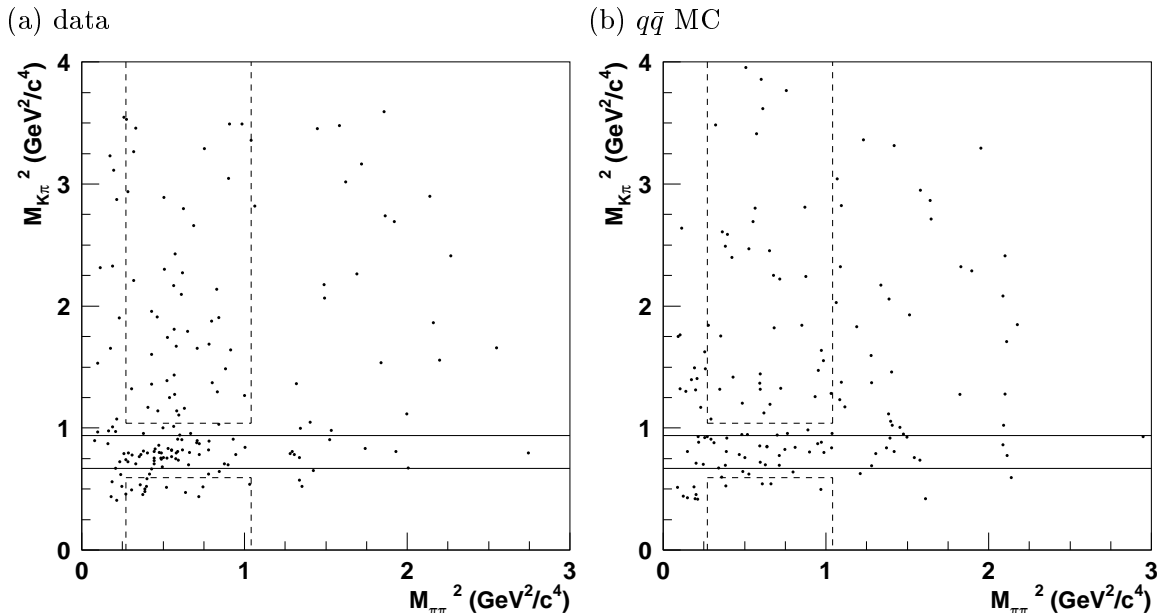
(a) data

(b) $q\bar{q}$ MC

Figure 6.4: $M_{K\pi}^2$ vs. $M_{\pi\pi}^2$ for (a) data and (b) $q\bar{q}$ MC in the $B^+ \to K^+\pi^-\pi^+\gamma$ analysis. Events in the signal region are plotted. In (a), $q\bar{q}$ background is not subtracted. The solid and dashed lines show the region for the K^* mass cut and the ρ mass cut, respectively.

$b \to s\gamma$ cross feed (C) in the fit. The normalization of the $q\bar{q}$ component is floated, but those of the $B\bar{B}$ and $b \to s\gamma$ components are fixed as in the $M_{\rm bc}$ fit. The fit is done in the region $M_{K\pi} < 1.7~{\rm GeV}/c^2$ and $M_{\pi\pi} < 1.7~{\rm GeV}/c^2$.

6.2.2   MC for $B^+ \to K^{*0}\pi^+\gamma$ and $B^+ \to K\rho^+\gamma$

To determine PDFs for $B^+ \to K^{*0}\pi^+\gamma$, we use an MC sample of decays through kaonic resonance $B^+ \to K_X^+\gamma \to K^*\pi\gamma$. However, the PDF for $M_{\pi\pi}$ slightly depends on the mass of the resonance. So, we choose two resonances with different mass, $K_1(1400)$ and $K^*(1680)$, and use a mixture of $B^+ \to K_1(1400)^+\gamma \to K^*\pi\gamma$ and $B^+ \to K^*(1680)^+\gamma \to K^*\pi\gamma$ MC to determine the PDFs of the $B^+ \to K^{*0}\pi^+\gamma$ component. We determine the ratio of the mixture of the two MC samples using the data M_{K_X} distribution after applying the K^* mass cut. The procedure of the determination is described in Appendix C. We set the the fraction of $B^+ \to K_1(1400)^+\gamma \to K^*\pi\gamma$ MC component to be 0.74 ± 0.14.

Likewise, we use a mixture of $B^+ \to K_1(1270)^+\gamma \to K\rho\gamma$ and $B^+ \to K^*(1680)^+\gamma \to K\rho\gamma$ MC for the determination of the PDFs of the $B^+ \to K\rho^-\gamma$ component. The ratio of the mixture is determined from the data M_{K_X} distribution after applying the ρ mass cut (Appendix C). We set the fraction of $B^+ \to K_1(1270)^+\gamma \to K\rho\gamma$ to be 0.68 ± 0.17.

The PDFs for the non-resonant $B^+ \to K^+\pi^-\pi^+\gamma$ component is determined from MC. We use $B^+ \to K_1(1650)^+\gamma \to K^+\pi^-\pi^+\gamma$ MC, where the sub-decay follows a phase space decay, to represent the non-resonant $B^+ \to K^+\pi^-\pi^+\gamma$ MC. A possible problem of this substitution is the difference of $M_{K\pi\pi}$ distribution. So, we also use an MC sample of $B^+ \to K_1(1400)^+\gamma \to K^+\pi^-\pi^+\gamma$ generated to follow a phase space decay as a cross check.

6.2.3   PDFs

The PDFs for $M_{\rm bc}$ are same as those used for the $M_{\rm bc}$ fit. We use an ARGUS function, a Gaussian and a smoothed MC histogram for $q\bar{q}$, signal, and $B\bar{B}$ or $b \to s\gamma$ cross feed, respectively.

(a) $M_{K\pi}$ (b) $M_{\pi\pi}$
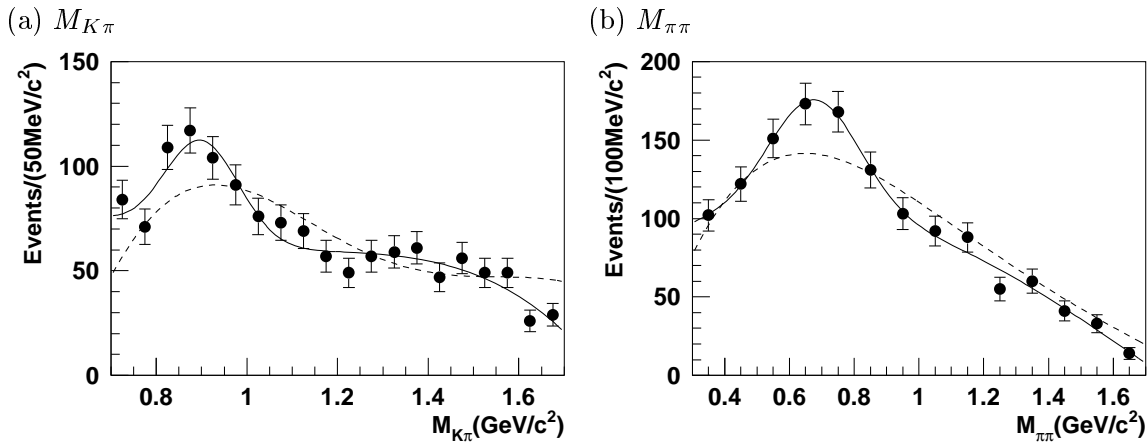
Figure 6.5: (a) $M_{K\pi}$ and (b) $M_{\pi\pi}$ distributions for the ΔE sideband data (point) and the obtained PDFs for the $q\bar{q}$ component (solid curves). Dashed curves show the fit results from $q\bar{q}$ MC.

The $M_{K\pi}$ and $M_{\pi\pi}$ PDFs for $q\bar{q}$ are obtained by fitting the ΔE sideband data with a sum of a fourth order polynomial and a Gaussian as shown in Fig. 6.5. As a cross check, we also use the $q\bar{q}$ MC to obtain the PDFs, which are overlaid in the figure.

The $M_{K\pi}$ and $M_{\pi\pi}$ PDFs for the other components are determined from the MC. Non-resonant Breit-Wigner functions are used to describe the $M_{K\pi}$ PDF for $B^+ \to K^{*0}\pi^+\gamma$ and the $M_{\pi\pi}$ PDF for $B^+ \to K^+\rho^0\gamma$, while sums of a fourth order polynomial and a Gaussian are used for the other $M_{K\pi}$ and $M_{\pi\pi}$ PDFs. The obtained PDFs are shown in Fig. 6.6. We also prepare several additional PDFs for cross checks. Details of the determination of the PDFs are shown in Appendix C.

6.2.4 Results

From the unbinned maximum likelihood fit, we obtain the signal yields and the statistical significances as listed in Table 6.2. The $M_{\rm bc}$, $M_{K\pi}$ and $M_{\pi\pi}$ distributions are shown in Fig. 6.7 (a) – (c) along with the fit results. Since the $B^+ \to K^+\rho^0\gamma$ and non-resonant $B^+ \to K^+\pi^-\pi^+\gamma$ components are not significant, we calculate the upper limits by Eq. (5.15). The distributions of the maximum likelihood $\mathcal{L}(n)$ is shown in Fig. 6.7 (d), and the resulting upper limits are listed in the table. The systematic errors of the yield due to the fitting procedure are evaluated using the same procedure as in the $B^0 \to K^+\pi^-\gamma$ analysis. We summarize their breakdown in Table 6.3.

We find that the $B^+ \to K^+\pi^-\pi^+\gamma$ signals are dominated by $B^+ \to K^{*0}\pi^+\gamma$ and $B^+ \to K^+\rho^0\gamma$. The statistical significance for the sum of the two components is calculated to be 6.2σ.

6.3 Search for the resonant decays

We also search for resonant decays by applying further kinematical requirements. Since $K_1(1270)$ has relatively large sub-decay branching fraction to $K\rho$, we apply the ρ mass cut (Eq. (6.2)) and $|M_{K\pi\pi} - M_{K_1(1270)}| < 100$ MeV/c^2 to search for $B^+ \to K_1(1270)^+\gamma$. These requirements exclude most of the $K^{*0}\pi^+\gamma$ decays, so the efficiency from other resonant decays is smaller by one order of magnitude. Hence, we can ignore the contributions from other resonant decays after applying these requirements. The $M_{\rm bc}$ distribution after applying these requirements are shown in Fig. 6.8 (a). Since contaminations from $B\bar{B}$ and $b \to s\gamma$ cross feed are negligible, we

(a) $M_{K\pi}$ PDF (signal)

(b) $M_{\pi\pi}$ PDF (signal)

(c) $M_{K\pi}$ PDF ($B\bar{B} + b \to s\gamma$)

(d) $M_{\pi\pi}$ PDF ($B\bar{B} + b \to s\gamma$)
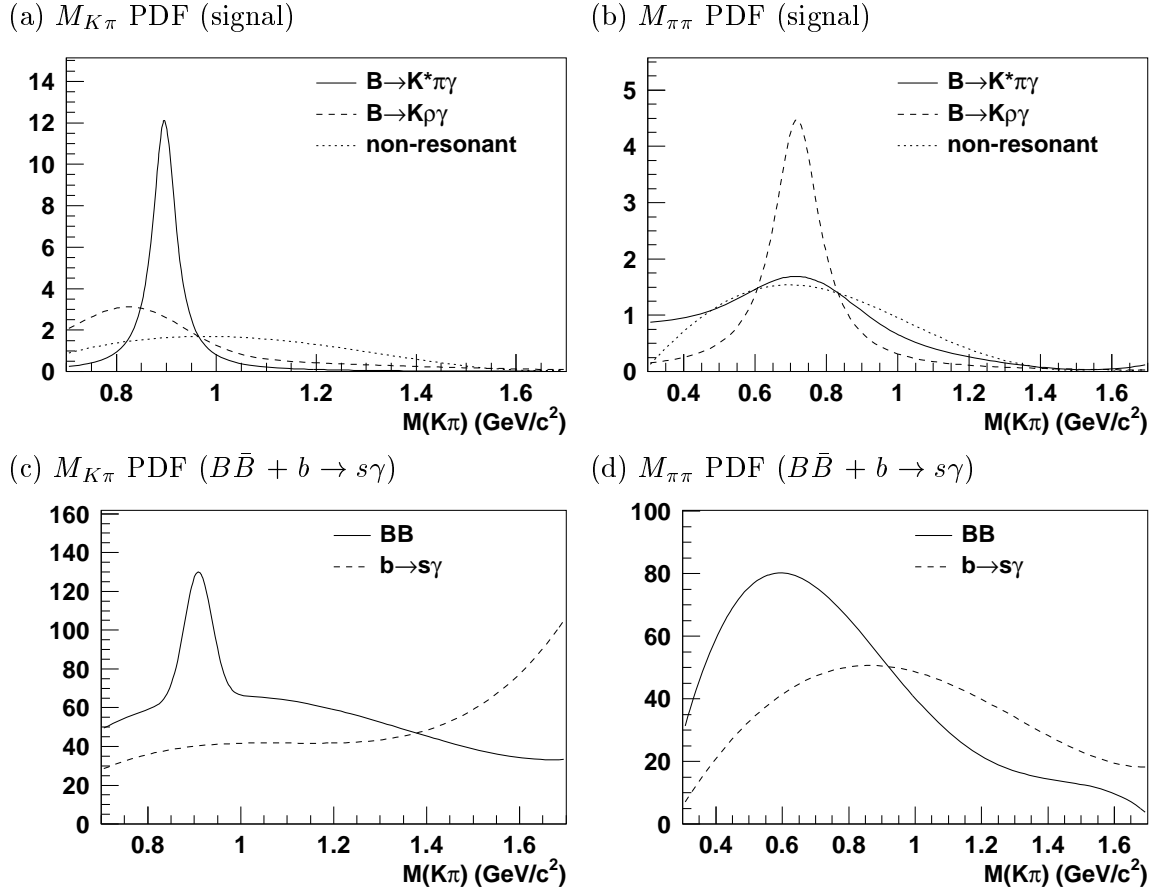
Figure 6.6: (a) $M_{K\pi}$ and (b) $M_{\pi\pi}$ PDFs for the $B^+ \to K^{*0}\pi^+\gamma$, $B^+ \to K^+\rho^0\gamma$ and non-resonant $B^+ \to K^+\pi^-\pi^+\gamma$ components, and (c) $M_{K\pi}$ and (d) $M_{\pi\pi}$ PDFs for the $B\bar{B}$ background and $b \to s\gamma$ cross feed. PDFs in (a) and (b) are normalized to 1, while the normalizations of PDFs in (c) and (d) are based on the luminosity.

Table 6.2: Signal yields, upper limits (UL) and statistical significances obtained from the unbinned maximum likelihood fit for $B^+ \to K^+\pi^-\pi^+\gamma$. ULs include the systematic error from the fitting procedure (the second error of the yield).

Component	Category	Yield	UL	Significance
$B^+ \to K^{*0}\pi^+\gamma$	signal	$32.6^{+10.8}_{-10.0}{}^{+1.9}_{-1.5}$	—	3.7
$B^+ \to K^+\rho^0\gamma$	signal	$23.8^{+11.5}_{-11.6}{}^{+3.5}_{-7.0}$	43.1	2.2
$B^+ \to K^+\pi^-\pi^+\gamma$ N.R.	signal	$0.0^{+10.6}_{-0.0} \pm 0.0$	20.0	—
$q\bar{q}$	(A)	$608.6^{+27.4}_{-27.0}$	—	—
$B\bar{B}$	(B)	57.4 (fixed)	—	—
$b \to s\gamma$	(C)	49.5 (fixed)	—	—

(a) M_{bc} (b) $M_{K\pi}$
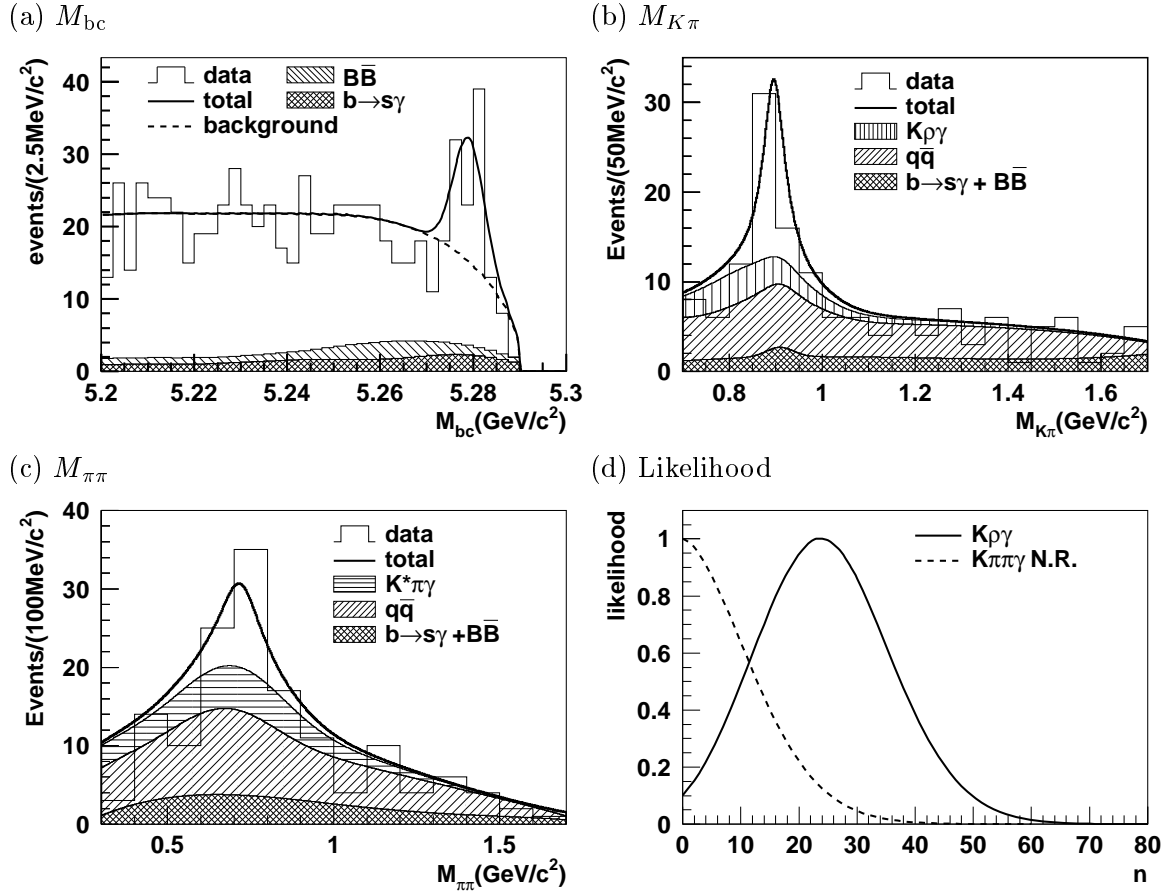
(c) $M_{\pi\pi}$ (d) Likelihood

Figure 6.7: (a) M_{bc}, (b) $M_{K\pi}$ and (c) $M_{\pi\pi}$ distributions and the unbinned maximum likelihood fit results. $M_{\mathrm{bc}} > 5.27$ GeV/c^2 is applied in (b) and (c). (d) Relation between the yield and the maximum likelihood for $B^+ \to K^+\rho^0\gamma$ and non-resonant $B^+ \to K^+\pi^-\pi^+\gamma$. The likelihood is normalized so that the maximum value gives 1.

fit the distribution with a sum of a Gaussian and an ARGUS function. The fit result is overlaid in the figure. The signal yield is obtained to be 3.1 ± 1.9 from the fit.

We use a method of Feldman and Cousins [82] to calculate the upper limit of the yield, since the number of events in the distribution is small. We find 6 events in the signal box, while the number of background estimated from the M_{bc} fit result is 2.0 ± 0.6 events, where the uncertainty of the shape of the ARGUS function is taken into account. From the Table V of the Ref. [82], we obtain the yield upper limit of 10.1 events.

The search for $B^+ \to K_1(1400)^+\gamma$ is done by applying the K^* mass cut and $|M_{K\pi\pi} - M_{K_1(1400)}| < 200$ MeV/c^2, because $K_1(1400)$ mainly decays to $K^*\pi$. The M_{bc} distribution is fitted with a sum of a Gaussian and an ARGUS function adding a smoothed MC for the $b \to s\gamma$ component with fixed normalization. The contamination for $B\bar{B}$ is negligible. The distribution and the fit result is shown in Fig. 6.8 (b). The signal yield is found to be $25.8\,^{+\,6.2\,+\,1.8}_{-\,5.6\,-\,0.4}$ events. However, there is contribution to the signal from resonant decays such as $B^+ \to K^*(1410)^+\gamma$, and we cannot distinguish them with the current statistics,[6] so we set an upper limit. From

---

[6]We can estimate the contribution of $B^+ \to K_2^*(1430)^+\gamma$ from Eq. (5.27), if we assume $\mathcal{B}(B^0 \to K_2^*(1430)^0\gamma) = \mathcal{B}(B^+ \to K_2^*(1430)^+\gamma)$. However, the error of the measured $B^0 \to K_2^*(1430)^0\gamma$ branching fraction is still very large, and it corresponds to only 3 ± 1 events out of the upper limit of 35.4 events. Since the result does not improve so much, we do not subtract the components for now.

Table 6.3: Breakdown of the yield systematic errors for $B^+ \to K^{*0}\pi^+\gamma$ and $B^+ \to K^+\rho^0\gamma$.

	$B^+ \to K^{*0}\pi^+\gamma$		$B^+ \to K^+\rho^0\gamma$	
	yield	deviation	yield	deviation
standard ($a = -16.9$)	32.6	—	23.8	—
shape $a = -16.4$ (+1σ)	32.7	+0.0	24.0	+0.2
shape $a = -26.7$ ($q\bar{q}$ MC)	32.6	−0.0	23.6	−0.2
gaussian peak (+$\Delta\mu$)	32.4	−0.3	24.0	+0.2
gaussian peak (−$\Delta\mu$)	32.8	+0.2	23.5	−0.3
gaussian width (+$\Delta\sigma$)	32.9	+0.2	23.8	+0.0
gaussian width (−$\Delta\sigma$)	32.4	−0.3	23.8	−0.0
M_{K^*} (+1σ)	32.3	−0.4	24.2	+0.4
M_{K^*} (−1σ)	33.0	+0.3	23.5	−0.3
Γ_{K^*} (+1σ)	33.4	+0.8	23.1	−0.7
Γ_{K^*} (−1σ)	31.7	−0.9	24.6	+0.8
M_ρ (+1σ)	32.4	−0.3	24.3	+0.5
M_ρ (−1σ)	33.0	+0.3	23.3	−0.5
Γ_ρ (+1σ)	32.7	+0.1	23.8	−0.0
Γ_ρ (−1σ)	32.6	+0.0	23.7	−0.1
Usage of $q\bar{q}$ MC	33.4	+0.8	27.1	+3.3
fraction in $K^*\pi\gamma$ MC (+1σ)	32.3	−0.4	22.9	−0.9
fraction in $K^*\pi\gamma$ MC (−1σ)	31.7	−0.9	25.4	+1.6
fraction in $K\rho\gamma$ MC (+1σ)	34.0	+1.3	16.9	−6.9
fraction in $K\rho\gamma$ MC (−1σ)	32.1	−0.5	27.0	+3.2
$M_{\pi\pi}$ PDF for $K\rho\gamma$ by Gaussian + polynomial	32.6	−0.0	24.0	+0.2
N.R. $K^+\pi^-\pi^+\gamma$ MC ($K_1(1400)$)	32.6	+0.0	23.8	+0.0
$b \to s\gamma$ MC ($m_b = 4.65$ GeV/c^2)	32.6	−0.1	24.3	+0.5
$b \to s\gamma$ MC ($m_b = 4.85$ GeV/c^2)	31.9	−0.7	23.6	−0.2
$b \to s\gamma$ MC normalization (+1σ)	32.3	−0.3	23.1	−0.7
$b \to s\gamma$ MC normalization (−1σ)	32.9	+0.3	24.4	+0.6
floating number of $b \to s\gamma$	33.6	+1.0	24.3	+0.5
floating number of $B\bar{B}$	32.5	−0.2	24.0	+0.2
total systematic error		+1.9 − 1.53		+3.5 − 7.0

Eq. (5.15), the upper limit is calculated to be 35.4 events.

6.4 Efficiency and systematic errors

6.4.1 MC Efficiency

We estimate the MC efficiencies using MC samples of resonant decays. The results are listed in Table 6.4. The MC samples contains not only $K^+\pi^-\pi^+\gamma$ final states but also other charge states such as $K^+\pi^0\pi^0\gamma$ and $K^0\pi^+\pi^0\gamma$. So, efficiencies are corrected by the factors calculated from the isospin relation.[7]

The efficiencies for $B^+ \to K^{*0}\pi^+\gamma$ and $B^+ \to K^+\rho^0\gamma$ are calculated from a weighted sum of the efficiencies of the resonant decays, where the choice of the resonances and the weight of the sum are the same as those used to obtain the PDFs (Sec. 6.2.2). The weighted sum of these two

---

[7]The correction factor for non-resonant decays is 0.466, which is used in the generation of MC.
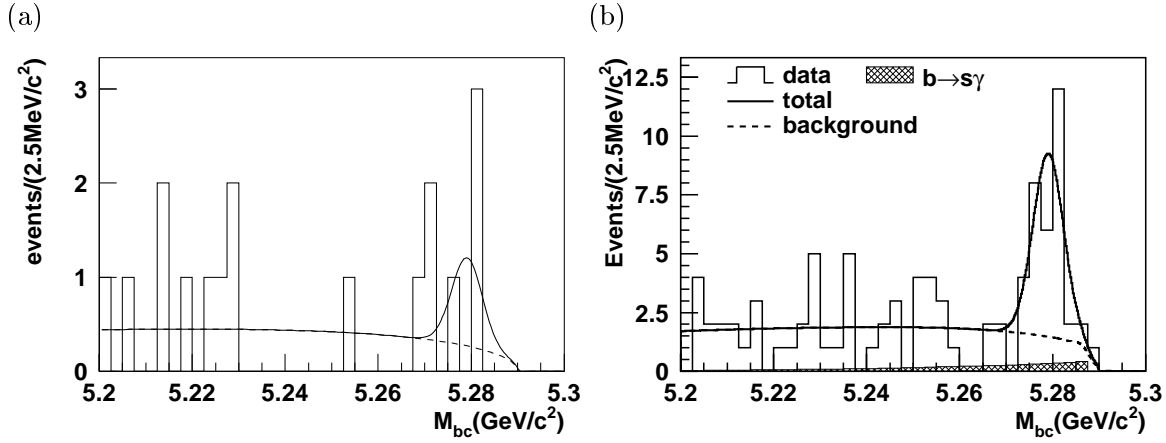
Figure 6.8: M_{bc} distributions after applying (a) the ρ mass cut and $|M_{K\pi\pi} - M_{K_1(1270)}| < 100$ MeV/c^2 and (b) the K^* mass cut and $|M_{K\pi\pi} - M_{K_1(1400)}| < 200$ MeV/c^2

efficiency is used as the efficiency for $B^+ \to K^+\pi^-\pi^+\gamma$, where the weight is determined from the result of the unbinned maximum likelihood fit. Then, the maximum difference between the obtained efficiency and the efficiencies for each resonant decay is considered as a systematic error. The efficiency for the non-resonant $B^+ \to K^+\pi^-\pi^+\gamma$ is obtained from the $B^+ \to K_1(1650)^+\gamma \to K^+\pi^-\pi^+\gamma$ MC and $B^+ \to K_1(1400)^+\gamma \to K^+\pi^-\pi^+\gamma$ MC. The obtained efficiencies are listed in Table 6.5.

The MC efficiencies in the search for the resonant decays are also calculated. Table 6.6 lists the efficiency for $B^+ \to K_1(1270)^+\gamma$ after applying the ρ mass cut and $|M_{K\pi\pi} - M_{K_1(1270)}| < 100$ MeV/c^2. The efficiencies after applying the K^* mass cut and $|M_{K\pi\pi} - M_{K_1(1400)}| < 200$ MeV/c^2 are listed in Table 6.7.

6.4.2 π^0/η veto, likelihood ratio and best candidate selection

We use $B^0 \to D^-\pi^+ \to K^+\pi^-\pi^-\pi^+$ decays to estimate the systematic errors for the π^0/η veto, the likelihood ratio selection and the best candidate selection efficiency. The procedure is the same as that used in the $B^0 \to K^+\pi^-\gamma$ analysis. The M_{bc} distributions for $B^0 \to D^-\pi^+$ data are shown in Fig. 6.9, and the efficiencies are listed in Table 6.8. We analyze $B^+ \to K^*(1680)^+\gamma \to K^{*0}\pi^+\gamma$ MC and $B^+ \to K^*(1680)^+\gamma \to K^+\rho^0\gamma$ MC for comparison. By combining the relative error of $B^0 \to D^-\pi^+$ MC and data, we obtain the systematic error of

$$\delta(\epsilon_{\mathrm{data}}/\epsilon_{\mathrm{MC}}) = 0.035. \tag{6.3}$$

6.4.3 Summary

The efficiency corrections and systematic errors in the $B^+ \to K^+\pi^-\pi^+\gamma$ are listed in Table 6.9. Systematics on photons, tracking and K/π identifications are common with the $B^0 \to K^+\pi^-\gamma$ analysis, except the difference of the number of pions in the final state. The efficiencies are calculated based on the MC efficiencies and the corrections, as listed in Table 6.10, The efficiency for $B^+ \to K_1(1270)^+\gamma$ and $B^+ \to K_1(1400)^+\gamma$ after applying the requirements for the search for the resonant decays are also listed in the table.

Table 6.4: MC efficiencies in the $B^+ \to K^+\pi^-\pi^+\gamma$ analysis. Efficiency for $q\bar{q}$ is also listed for comparison. "$K_1(1400)[K^*\pi]\gamma$" means $B^+ \to K_1(1400)^+\gamma \to K^*\pi\gamma$. "Total (isospin)" is the efficiency after correcting the isospin factor.

Selections	$K_1(1400)[K^*\pi]\gamma$	$K^*(1410)[K^*\pi]\gamma$	$K^*(1680)[K^*\pi]\gamma$
signal reconstruction	0.243 ± 0.003	0.260 ± 0.003	0.256 ± 0.003
dr, $|dz|$ selection	0.763 ± 0.006	0.733 ± 0.006	0.749 ± 0.006
$|\vec{p}^*|$ selection	0.873 ± 0.005	0.843 ± 0.006	0.861 ± 0.006
kaon probability	0.874 ± 0.006	0.873 ± 0.006	0.888 ± 0.005
$\cos\theta_\gamma$	0.914 ± 0.005	0.908 ± 0.005	0.899 ± 0.006
E_9/E_{25}	0.956 ± 0.004	0.959 ± 0.004	0.951 ± 0.004
π^0/η	0.870 ± 0.007	0.889 ± 0.006	0.873 ± 0.007
$K^*\gamma$ veto	0.999 ± 0.001	1.000 ± 0.000	0.999 ± 0.001
likelihood ratio	0.421 ± 0.011	0.413 ± 0.011	0.407 ± 0.011
best cand. selection	0.803 ± 0.013	0.807 ± 0.013	0.788 ± 0.014
$M_{K\pi}$, $M_{\pi\pi}$ cut	0.981 ± 0.005	0.982 ± 0.005	0.977 ± 0.006
Total	$(3.55 \pm 0.13) \times 10^{-2}$	$(3.55 \pm 0.13) \times 10^{-2}$	$(3.43 \pm 0.13) \times 10^{-2}$
Total (isospin)	$(7.99 \pm 0.29) \times 10^{-2}$	$(7.99 \pm 0.29) \times 10^{-2}$	$(7.71 \pm 0.29) \times 10^{-2}$

Selections	$K_1(1270)[K\rho]\gamma$	$K^*(1680)[K\rho]\gamma$	$K_1(1400)[K\pi\pi]\gamma$
signal reconstruction	0.184 ± 0.003	0.192 ± 0.003	0.273 ± 0.003
dr, $|dz|$ selection	0.771 ± 0.007	0.754 ± 0.007	0.740 ± 0.006
$|\vec{p}^*|$ selection	0.866 ± 0.006	0.881 ± 0.006	0.861 ± 0.005
kaon probability	0.859 ± 0.007	0.883 ± 0.006	0.888 ± 0.005
$\cos\theta_\gamma$	0.921 ± 0.006	0.891 ± 0.007	0.917 ± 0.005
E_9/E_{25}	0.953 ± 0.005	0.957 ± 0.005	0.949 ± 0.004
π^0/η	0.895 ± 0.007	0.860 ± 0.008	0.892 ± 0.006
$K^*\gamma$ veto	0.999 ± 0.001	0.999 ± 0.001	1.000 ± 0.000
likelihood ratio	0.408 ± 0.012	0.417 ± 0.012	0.396 ± 0.010
best cand. selection	0.827 ± 0.015	0.802 ± 0.015	0.815 ± 0.013
$M_{K\pi}$, $M_{\pi\pi}$ cut	0.934 ± 0.010	0.920 ± 0.012	0.926 ± 0.009
Total	$(2.62 \pm 0.11) \times 10^{-2}$	$(2.53 \pm 0.11) \times 10^{-2}$	$(3.58 \pm 0.13) \times 10^{-2}$
Total (isospin)	$(7.86 \pm 0.34) \times 10^{-2}$	$(7.59 \pm 0.33) \times 10^{-2}$	$(7.69 \pm 0.28) \times 10^{-2}$

Selections	$K_1(1650)[K\pi\pi]\gamma$	$q\bar{q}$
signal reconstruction	0.264 ± 0.003	$(8.34 \pm 0.02) \times 10^{-4}$
dr, $|dz|$ selection	0.756 ± 0.006	0.482 ± 0.001
$|\vec{p}^*|$ selection	0.868 ± 0.005	0.821 ± 0.001
kaon probability	0.885 ± 0.005	0.631 ± 0.002
$\cos\theta_\gamma$	0.909 ± 0.005	0.849 ± 0.002
E_9/E_{25}	0.951 ± 0.004	0.649 ± 0.003
π^0/η	0.883 ± 0.006	0.381 ± 0.003
$K^*\gamma$ veto	1.000 ± 0.000	0.998 ± 0.001
likelihood ratio	0.415 ± 0.010	$(2.28 \pm 0.17) \times 10^{-2}$
best cand. selection	0.795 ± 0.013	0.818 ± 0.029
$M_{K\pi}$, $M_{\pi\pi}$ cut	0.965 ± 0.007	0.865 ± 0.028
Total	$(3.73 \pm 0.13) \times 10^{-2}$	$(7.03 \pm 0.62) \times 10^{-7}$
Total (isospin)	$(8.00 \pm 0.29) \times 10^{-2}$	—

Table 6.5: Summary of MC efficiencies in the $B^+ \to K^+\pi^-\pi^+\gamma$ analysis. MC efficiencies obtained from weighted sums are also listed.

	Mode	MC efficiency	
(a)	$B^+ \to K_1(1400)^+\gamma \to K^*\pi\gamma$	$(7.99 \pm 0.29)\%$	
(b)	$B^+ \to K^*(1410)^+\gamma \to K^*\pi\gamma$	$(7.99 \pm 0.29)\%$	
(c)	$B^+ \to K^*(1680)^+\gamma \to K^*\pi\gamma$	$(7.71 \pm 0.29)\%$	
(d)	$B^+ \to K_1(1270)^+\gamma \to K\rho\gamma$	$(7.86 \pm 0.34)\%$	
(e)	$B^+ \to K^*(1680)^+\gamma \to K\rho\gamma$	$(7.59 \pm 0.33)\%$	
(f)	$B^+ \to K_1(1400)^+\gamma \to K\pi\pi\gamma$	$(7.69 \pm 0.28)\%$	
(g)	$B^+ \to K_1(1650)^+\gamma \to K\pi\pi\gamma$	$(8.00 \pm 0.29)\%$	
(h)	$B^+ \to K^{*0}\pi^+\gamma$	$(5.28 \pm 0.15 \pm 0.14)\%$	(a)+(c)
(i)	$B^+ \to K^+\rho^0\gamma$	$(7.77 \pm 0.25 \pm 0.18)\%$	(d)+(e)
(j)	$B^+ \to K^+\pi^-\pi^+\gamma$ (N.R.)	$(8.00 \pm 0.29 \pm 0.31)\%$	(g)
(k)	$B^+ \to K^+\pi^-\pi^+\gamma$	$(7.85 \pm 0.17 \pm 0.26)\%$	(h)+(i)

Table 6.6: MC efficiencies in the $B^+ \to K^+\pi^-\pi^+\gamma$ analysis with the ρ mass cut and the requirement $|M_{K\pi\pi} - M_{K_1(1270)}| < 100$ MeV/c^2. Efficiencies for $B^+ \to K_2^*(1430)^+\gamma$ and $q\bar{q}$ are also listed for comparison. Sub-decay branching fractions are included in the efficiencies.

Selections	$B^+ \to K_1(1270)^+\gamma$	$B^+ \to K_2^*(1430)^+\gamma$	$q\bar{q}$
signal reconstruction	0.208 ± 0.003	0.113 ± 0.002	$(8.34 \pm 0.02) \times 10^{-4}$
dr, $|dz|$ selection	0.763 ± 0.007	0.618 ± 0.010	0.482 ± 0.001
$|\vec{p}^*|$ selection	0.868 ± 0.006	0.791 ± 0.011	0.821 ± 0.001
kaon probability	0.875 ± 0.006	0.851 ± 0.011	0.631 ± 0.002
$\cos\theta_\gamma$	0.917 ± 0.006	0.914 ± 0.009	0.849 ± 0.002
E_9/E_{25}	0.956 ± 0.004	0.957 ± 0.007	0.649 ± 0.003
π^0/η	0.880 ± 0.007	0.891 ± 0.011	0.381 ± 0.003
$K^*\gamma$ veto	1.000 ± 0.000	0.999 ± 0.001	0.998 ± 0.001
likelihood ratio	0.400 ± 0.011	0.350 ± 0.018	$(2.28 \pm 0.17) \times 10^{-2}$
best cand. selection	0.806 ± 0.014	0.761 ± 0.027	0.818 ± 0.029
$M_{K\pi\pi}$ selection	0.825 ± 0.016	0.170 ± 0.027	$(8.78 \pm 2.33) \times 10^{-2}$
ρ mass cut	0.170 ± 0.017	$(9.09 \pm 5.00) \times 10^{-2}$	0.154 ± 0.100
Total	$(4.20 \pm 0.46) \times 10^{-3}$	$(1.50 \pm 0.87) \times 10^{-4}$	$(1.10 \pm 0.78) \times 10^{-8}$

6.5 Branching Fractions

From the number of $B\bar{B}$ in Eq. (4.2), the signal yields in Table 6.2 and the efficiencies in Table 6.10, the branching fractions are calculated to be

$$\mathcal{B}(B^+ \to K^+\pi^-\pi^+\gamma) = (2.41^{+0.50}_{-0.47}{}^{+0.40}_{-0.30}) \times 10^{-5} \tag{6.4}$$

$$\mathcal{B}(B^+ \to K^{*0}\pi^+\gamma) = (2.04^{+0.67}_{-0.62}{}^{+0.22}_{-0.21}) \times 10^{-5} \tag{6.5}$$

$$\mathcal{B}(B^+ \to K^+\rho^0\gamma) = (1.01 \pm 0.49^{+0.18}_{-0.31}) \times 10^{-5} \tag{6.6}$$

$$< 2.04 \times 10^{-5} \quad\quad (90\% \text{ C.L.}) \tag{6.7}$$

$$\mathcal{B}(B^+ \to K^+\pi^-\pi^+\gamma(\text{N.R.})) < 0.93 \times 10^{-5} \quad\quad (90\% \text{ C.L.}). \tag{6.8}$$

We find that the $B^+ \to K^+\pi^-\pi^+\gamma$ decay can be explained by $B^+ \to K^{*0}\pi^+\gamma$ and $B^+ \to K^+\rho^0\gamma$ (the branching fraction of $K^{*0} \to K^+\pi^-$ is 2/3). If we sum up the branching fraction for resonant

Table 6.7: MC efficiencies in the $B^+ \to K^+\pi^-\pi^+\gamma$ analysis with the K^* mass cut and the requirement $|M_{K\pi\pi} - M_{K_1(1400)}| < 200$ MeV/c^2. Efficiency for $q\bar{q}$ is also listed for comparison.

Selections	$B^+ \to K_1(1270)^+\gamma$	$B^+ \to K_1(1400)^+\gamma$	$B^+ \to K^*(1410)^+\gamma$
signal reconstruction	0.208 ± 0.003	0.247 ± 0.003	0.249 ± 0.003
dr, $|dz|$ selection	0.763 ± 0.007	0.763 ± 0.006	0.733 ± 0.006
$|\vec{p}^*|$ selection	0.868 ± 0.006	0.864 ± 0.006	0.846 ± 0.006
kaon probability	0.875 ± 0.006	0.887 ± 0.006	0.896 ± 0.005
$\cos\theta_\gamma$	0.917 ± 0.006	0.911 ± 0.005	0.912 ± 0.005
E_9/E_{25}	0.956 ± 0.004	0.951 ± 0.004	0.954 ± 0.004
π^0/η	0.880 ± 0.007	0.876 ± 0.007	0.880 ± 0.007
$K^*\gamma$ veto	1.000 ± 0.000	1.000 ± 0.000	1.000 ± 0.000
likelihood ratio	0.400 ± 0.011	0.428 ± 0.011	0.395 ± 0.011
best cand. selection	0.806 ± 0.014	0.823 ± 0.012	0.782 ± 0.014
$M_{K\pi\pi}$ selection	0.848 ± 0.015	0.854 ± 0.013	0.728 ± 0.017
K^* mass cut	0.444 ± 0.022	0.830 ± 0.015	0.853 ± 0.016
Total	$(1.13 \pm 0.07) \times 10^{-2}$	$(2.73 \pm 0.12) \times 10^{-2}$	$(2.04 \pm 0.10) \times 10^{-2}$

Selections	$B^+ \to K_2^*(1430)^+\gamma$	$q\bar{q}$
signal reconstruction	0.113 ± 0.002	7.593 ± 0.000
dr, $|dz|$ selection	0.618 ± 0.010	0.482 ± 0.001
$|\vec{p}^*|$ selection	0.791 ± 0.011	0.821 ± 0.001
kaon probability	0.851 ± 0.011	0.631 ± 0.002
$\cos\theta_\gamma$	0.914 ± 0.009	0.849 ± 0.002
E_9/E_{25}	0.957 ± 0.007	0.649 ± 0.003
π^0/η	0.891 ± 0.011	0.381 ± 0.003
$K^*\gamma$ veto	0.999 ± 0.001	0.998 ± 0.001
likelihood ratio	0.350 ± 0.018	$(2.28 \pm 0.17) \times 10^{-2}$
best cand. selection	0.761 ± 0.027	0.818 ± 0.029
$M_{K\pi\pi}$ selection	0.871 ± 0.024	0.243 ± 0.035
K^* mass cut	0.757 ± 0.033	0.306 ± 0.077
Total	$(6.40 \pm 0.56) \times 10^{-3}$	$(5.50 \pm 1.66) \times 10^{-4}$

Table 6.8: Efficiencies (%) for the π^0/η veto, the likelihood ratio (LR) selection and the best candidate selection for the $B^+ \to K^+\pi^-\pi^+\gamma$ analysis.

	$B^0 \to D^-\pi^+$ data	$B^0 \to D^-\pi^+$ MC	$K^*(1680)^+\gamma$ $\to K^{*0}\pi^+\gamma$ MC	$K^*(1680)^+\gamma$ $\to K^+\rho^0\gamma$ MC
yield without selections	2378	6170	2129	1614
π_0/η veto	84.4 ± 0.7	85.7 ± 0.4	87.0 ± 0.7	86.3 ± 0.9
π_0/η veto + LR	34.4 ± 1.0	34.3 ± 0.6	36.3 ± 1.0	35.7 ± 1.2
all the three selections	32.2 ± 1.0	32.1 ± 0.6	28.9 ± 1.0	28.9 ± 1.1
relative error (%)	± 2.98	± 1.85	± 3.40	± 3.90

(a) no selection

(b) π^0/η veto

(c) π^0/η veto and likelihood ratio

(d) all the selections
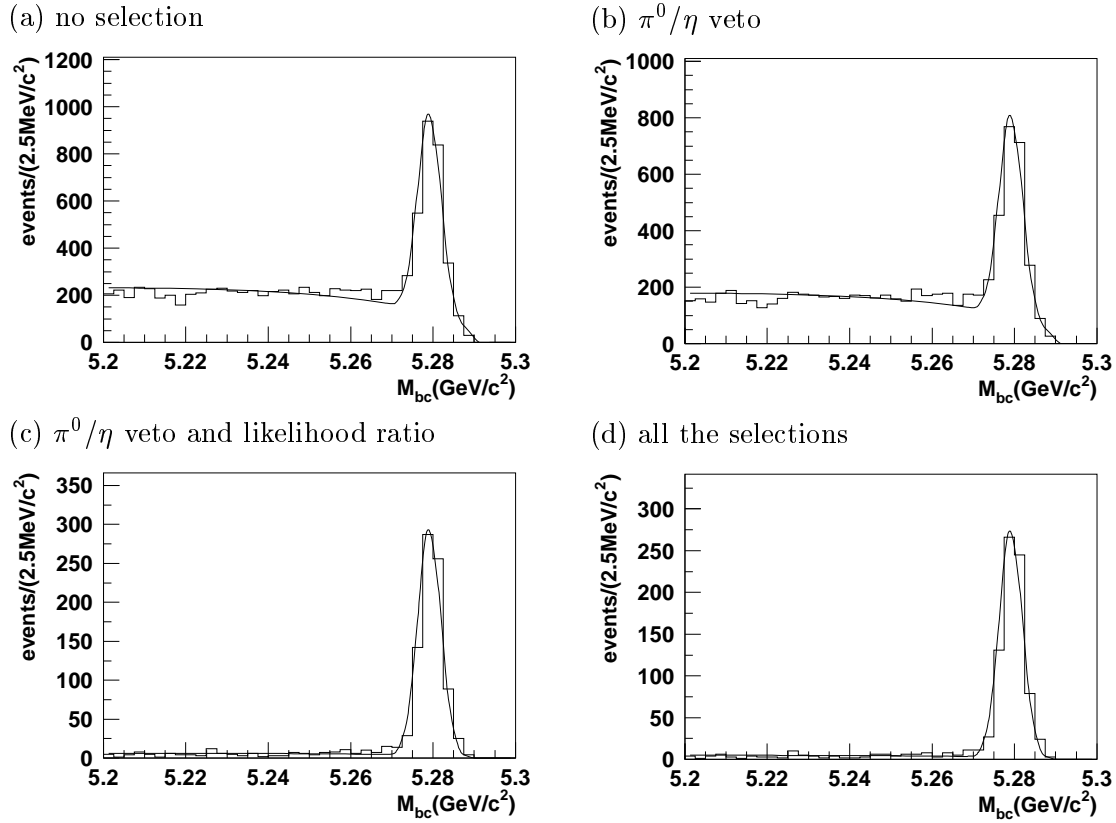
Figure 6.9: M_{bc} distributions for data for $B^0 \to D^-\pi^+ \to K^-\pi^-\pi^-\pi^+$ with (a) no selection, (b) the π^0/η veto, (c) the likelihood ratio selection along with (b), and (d) the best candidate selection along with (c). Fit results are overlaid.

Table 6.9: Summary of the efficiency corrections in the $B^+ \to K^+\pi^-\pi^+\gamma$ analysis.

photon detection	1.000 ± 0.028
tracking	0.936 ± 0.066
K identification	1.038 ± 0.006
π identification	0.976 ± 0.009
π^0/η veto, LR, best cand. selection	1.000 ± 0.035
efficiency correction factor	0.948 ± 0.080

Table 6.10: Efficiencies in the $B^+ \to K^+\pi^-\pi^+\gamma$ analysis. The ρ mass cut and K^* mass cut as well as the requirement for $M_{K\pi\pi}$ are considered for the efficiencies for $B^+ \to K_1(1270)^+\gamma$ and $B^+ \to K_1(1400)^+\gamma$, respectively.

	MC efficiency	Sub-decay BF uncertainty	Efficiency
$B^+ \to K^+\pi^-\pi^+\gamma$	$(7.85 \pm 0.17 \pm 0.26)\%$	—	$(7.45 \pm 0.91)\%$
$B^+ \to K^{*0}\pi^+\gamma$	$(5.28 \pm 0.15 \pm 0.14)\%$	—	$(5.00 \pm 0.46)\%$
$B^+ \to K^+\rho^0\gamma$	$(7.77 \pm 0.25 \pm 0.18)\%$	—	$(7.37 \pm 0.69)\%$
$B^+ \to K^+\pi^-\pi^+\gamma$ N.R.	$(8.00 \pm 0.29 \pm 0.31)\%$	—	$(7.59 \pm 0.75)\%$
$B^+ \to K_1(1270)^+\gamma$	$(0.42 \pm 0.05)\%$	14%	$(0.40 \pm 0.08)\%$
$B^+ \to K_1(1400)^+\gamma$	$(2.73 \pm 0.12)\%$	6.4%	$(2.59 \pm 0.29)\%$

decays predicted by Veseli and Olsson (Table 2.3), we find[8] $\mathcal{B}(B^+ \to K^{*0}\pi^+\gamma) = (1.6\pm0.6)\times10^{-5}$ and $\mathcal{B}(B^+ \to K^+\rho^0\gamma) = (0.3 \pm 0.1) \times 10^{-5}$. Therefore, our measurement is consistent with the prediction if we ignore the non-resonant $K^*\pi\gamma$ and $K\rho\gamma$ components.

We also obtain the upper limit for the branching fraction of the resonant decays

$$\mathcal{B}(B^+ \to K_1(1270)^+\gamma) < 9.94 \times 10^{-5} \qquad (90\% \text{ C.L.}) \qquad (6.9)$$

$$\mathcal{B}(B^+ \to K_1(1400)^+\gamma) < 5.01 \times 10^{-5} \qquad (90\% \text{ C.L.}). \qquad (6.10)$$

These results improve the present upper limit by ARGUS [25], but more improvement is necessary to test the prediction.

---

[8]We assume 100% correlation among the errors of the predicted branching fractions.

Chapter 7

Conclusion

7.1 Discussion

Table 7.1 lists the measured branching fractions for the $b \to s\gamma$ process for exclusive and inclusive modes. Here, we assume equal branching fractions for neutral and charged B decays. Using isospin, the branching fraction of $B^+ \to K^{*+}\pi^0\gamma$ ($K^0\rho^+\gamma$) is assumed to be half (twice) of that for $B^+ \to K^{*0}\pi^+\gamma$ ($K^+\rho^0\gamma$). Now, $(35 \pm 8)\%$ of the total $B \to X_s\gamma$ decay is accounted for by $B \to K^*\gamma$, $B \to K_2^*(1430)\gamma$ and $B \to K\pi\pi\gamma$ decays.

One of the motivation of this study is to understand the final states of the $b \to s\gamma$ process for the measurement of the inclusive branching fraction. We compare the result with the inclusive $b \to s\gamma$ MC used to estimate the cross feed. This MC is basically the same as that used in the measurement of the inclusive branching fraction at Belle [12]. Figure 7.1 shows the M_{X_s} distributions for data and the $b \to s\gamma$ MC which are reconstructed in the $K^+\pi^-\gamma$ and $K^+\pi^-\pi^+\gamma$ final state. The distributions for data are obtained by subtracting the background components in Figs. 5.12 (b) and 6.3 (b). The normalization of the distributions for $b \to s\gamma$ are based on the luminosity and the $b \to s\gamma$ branching fraction measured by Belle (Eq. (2.11)), and have around 25% uncertainty. In Fig. 7.1 (a), we can see significant discrepancy in the $M_{K\pi}$ distribution in $K^+\pi^-\gamma$ between data and the $b \to s\gamma$ MC; the $K^+\pi^-\gamma$ final state is overestimated in JETSET, which is responsible for the hadronization process in the MC. As for the $K^+\pi^-\pi^+\gamma$ final state, it seems that events distribute below 1.8 GeV/c^2 for data, while the distribution for the $b \to s\gamma$ MC extends up to more than 2.4 GeV/c^2

We also examine the generated modes of the $b \to s\gamma$ MC, where $B \to K^*\gamma$ components are not included. We find around 18% and 33% of events are generated as $K\pi\gamma$ and $K\pi\pi\gamma$ modes,

Table 7.1: Exclusive and inclusive branching fractions for the $b \to s\gamma$ process. Equal branching fractions are assumed for neutral and charged B decays.

Mode	Branching fraction ($\times 10^{-5}$)
$B \to K^*\gamma$	4.2 ± 0.4
$B \to K_2^*(1430)\gamma$ (excluding $K^*\pi\gamma$, $K\rho\gamma$)	0.9 ± 0.3
$B \to K^*\pi\gamma$	3.1 ± 1.0
$B \to K\rho\gamma$	3.0 ± 1.6
Sum of exclusive modes	11.2 ± 2.1
$B \to X_s\gamma$ (inclusive)	32.2 ± 4.0
exclusive ratio	$(35 \pm 8)\%$

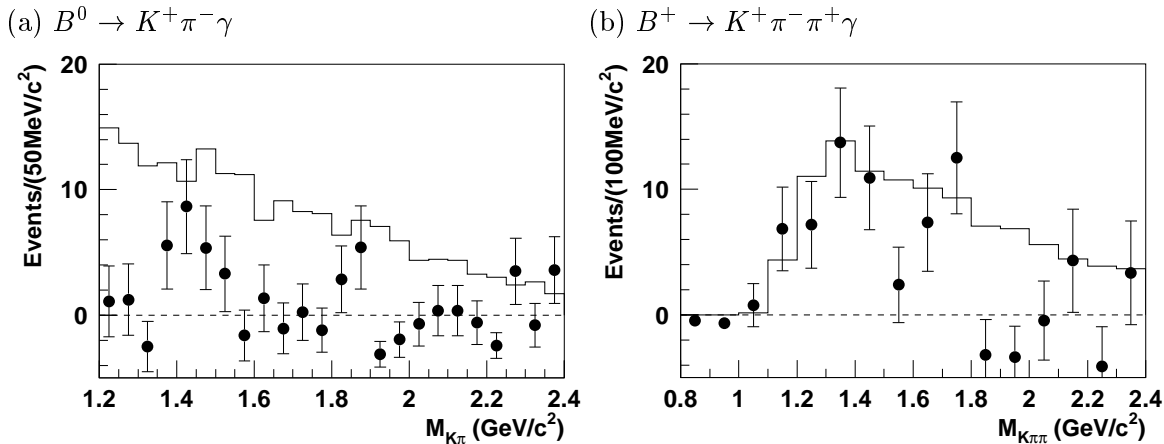(a) $B^0 \to K^+\pi^-\gamma$ (b) $B^+ \to K^+\pi^-\pi^+\gamma$

Figure 7.1: Comparison of data (points) and the $b \to s\gamma$ MC (histogram) by (a) $M_{K\pi}$ distribution in the $K^+\pi^-\gamma$ final state and (b) $M_{K\pi\pi}$ distribution in the $K^+\pi^-\pi^+\gamma$ final state. The histograms for the $b \to s\gamma$ MC are normalized based on the luminosity.

respectively. If we add the contribution from $B \to K^*\gamma$, the fraction of the $K\pi\gamma$ and $K\pi\pi\gamma$ final state in the $b \to s\gamma$ MC becomes around 57%, and this is considerably higher than our measured exclusive ratio $(35 \pm 8)\%$. So, there exists discrepancy between data and the inclusive $b \to s\gamma$ MC.

In the inclusive $b \to s\gamma$ analysis, all the $b \to s\gamma$ process except $B \to K^*\gamma$ is usually simulated by JETSET. However, because we find the non-resonant components are small both for $B^0 \to K^+\pi^-\gamma$ and $B^+ \to K^+\pi^-\pi^+\gamma$, it might be better to simulate $B \to K\pi\gamma$ and $B \to K\pi\pi\gamma$ as a sum of resonant decays. This can be one way to correct the discrepancy between data and the $b \to s\gamma$ MC for more precise measurement of inclusive $B \to X_s\gamma$, although we need more study.

As to the future prospect of the experiment, we like to comment on the photon helicity measurement. As discussed in Sec 2.3, the $K\pi\pi\gamma$ final state can be used for the measurement of the photon helicity. Therefore, the observation of the mode $B^+ \to K^+\pi^-\pi^+\gamma$ is an important step for the search for New Physics accessible by the photon helicity measurement. Actually, the final states that we really want are $B^0 \to K^0_S\pi^+\pi^-\gamma$ and $B^0 \to K^+\pi^-\pi^0\gamma$, but we can predict their branching fractions using isospin relation. We expect the observation is possible for these modes with twice or three times of data that used in this analysis, which is already available in Belle.

The next step is to understand the resonant structures in $B \to K_X\gamma \to K\pi\pi\gamma$. This is also important for the comparison with the theoretical calculation, as described in Sec 2.2. In order to perform it, we need to develop our method as well as to increase the statistic. Reconstruction of $K\omega\gamma$ and $K\eta\gamma$ final states may be helpful to identify resonances: among many kaonic resonances, only $K_1(1270)$ and $K_3^*(1780)$ have considerable branching fractions to $K\omega$ and $K\eta$, respectively. We can also use the information from the helicity angular distribution, which depends on the spin and parity of each resonance. These informations will improve the ability to disentangle the structures of resonant decays. When we reach this second step in the future, we can start the search for New Physics using the $B \to K\pi\pi\gamma$ mode.

7.2   Summary of the results

We have studied the radiative B decays with the $K^+\pi^-\gamma$ and $K^+\pi^-\pi^+\gamma$ final states using a data sample of 29.4 fb^{-1} taken by Belle. We summarize the results in Table 7.2.

Table 7.2: Measured signal yields, statistical significances (Snf.), reconstruction efficiencies, branching fractions ($\mathcal{B}$) and 90% confidence level upper limits (UL) including systematic errors. Efficiencies include the sub-decay branching fractions.

Mode	Signal yield	UL (yield)	Snf.	Efficiency (%)	$\mathcal{B}$ (10^{-5})	UL (10^{-5})
$K^+\pi^-\gamma^\dagger$	$27.0^{+7.5+0.8}_{-6.8-3.4}$	—	$5.0^\S$	18.4 ± 1.7	$0.46^{+0.13+0.05}_{-0.12-0.07}$	—
$K_2^*(1430)^0\gamma$	$21.2^{+7.6+0.5}_{-7.1-1.2}$	—	3.2	4.97 ± 0.33	$1.33^{+0.48+0.09}_{-0.45-0.11}$	—
$K^*(1410)^0\gamma$	$7.6^{+7.1+0.5}_{-5.7-1.3}$	19.3	—	0.58 ± 0.12	—	13.2
$K^+\pi^-\gamma$ N.R.†	$0.0^{+4.7+0.0}_{-0.0-0.0}$	15.3	—	18.6 ± 1.2	—	0.26
$K^+\pi^-\pi^+\gamma^\ddagger$	$57.2^{+11.8+6.4}_{-11.1-1.9}$	—	$5.9^\S$	7.45 ± 0.91	$2.41^{+0.50+0.40}_{-0.47-0.30}$	—
$K^{*0}\pi^+\gamma^\ddagger$	$32.6^{+10.8+1.9}_{-10.0-1.5}$	—	3.7	5.00 ± 0.46	$2.04^{+0.67+0.22}_{-0.62-0.21}$	—
$K^+\rho^0\gamma^\ddagger$	$23.8^{+11.5+3.5}_{-11.6-7.0}$	43.1	2.2	7.37 ± 0.69	$1.01\pm0.49^{+0.18}_{-0.31}$	2.04
$K^+\pi^-\pi^+\gamma$ N.R.‡	$0.0^{+10.6}_{-0.0}\pm0.0$	20.0	—	7.59 ± 0.75	—	0.93
$K_1(1270)^+\gamma$	$4.0\pm2.4\pm0.6$	10.1	—	0.40 ± 0.08	—	9.94
$K_1(1400)^+\gamma$	$25.8^{+6.2+1.8}_{-5.6-0.4}$	35.4	—	2.59 ± 0.29	—	5.01

$\dagger$ $1.25\ \mathrm{GeV}/c^2 < M_{K\pi} < 1.6\ \mathrm{GeV}/c^2$ $\qquad$ $\ddagger$ $M_{K\pi\pi} < 2.4\ \mathrm{GeV}/c^2$ $\qquad$ $\S$ M_{bc} fit result

For the $K^+\pi^-\gamma$ final state, we observe a signal around $M_{K\pi} = 1.4\ \mathrm{GeV}/c^2$. We extract the $B^0 \to K_2^*(1430)^0\gamma$ component taking into account the $B^0 \to K^*(1410)^0\gamma$ and non-resonant components, and find evidence for $B^0 \to K_2^*(1430)^0\gamma$. We measure the branching fraction to be

$$\mathcal{B}(B^0 \to K_2^*(1430)^0\gamma) = (1.33^{+0.48+0.09}_{-0.45-0.11}) \times 10^{-5}.$$

For $B^+ \to K^+\pi^-\pi^+\gamma$, we observe the decay mode and measure the branching fraction for the first time. We obtain

$$\mathcal{B}(B^+ \to K^+\pi^-\pi^+\gamma) = (2.41^{+0.50+0.40}_{-0.47-0.30}) \times 10^{-5}.$$

We find the decay is dominated by $B^+ \to K^{*0}\pi^+\gamma$ and $B^+ \to K^+\rho^0\gamma$. Assuming that a large part of $B^+ \to K^+\pi^-\pi^+\gamma$ decays is a resonant decays, the branching fraction is consistent with the theoretical calculation by Veseli and Olsson.

Appendix A

CKM Matrix and Unitarity Triangle

The Lagrangian of the charged current weak interaction is written as

$$\mathcal{L}_{cc} = -\frac{g_W}{\sqrt{2}} \sum_{j,k} \left[\bar{u}_{jL} \gamma^\mu V_{jk} d_{jL} W_\mu^+ + \bar{d}_{kL} \gamma^\mu V_{kj}^* u_{jL} W_\mu^- \right], \tag{A.1}$$

where g_W is the weak coupling constant, $(u_{1L}, u_{2L}, u_{3L}) = (u_L, c_L, t_L)$ and $(d_{1L}, d_{2L}, d_{3L}) = (d_L, s_L, b_L)$ are mass eigenstates of quarks. Here, $V = (V_{jk})$ is a 3×3 unitary matrix called Cabibbo-Kobayashi-Maskawa (CKM) matrix, which expresses the mixing between generations. If CP is conserved in the charged current weak interaction, V must be real except an overall phase and phases that can be absorbed by the re-definition of the quark fields.

The standard parameterization of the CKM matrix with three mixing angles θ_{12}, θ_{13} and θ_{23} and a phase δ is [83]

$$V = \begin{pmatrix} V_{ud} & V_{us} & V_{ub} \\ V_{cd} & V_{cs} & V_{cb} \\ V_{td} & V_{ts} & V_{tb} \end{pmatrix}$$

$$= \begin{pmatrix} c_{12}c_{13} & s_{12}c_{13} & s_{13}e^{-i\delta} \\ -s_{12}c_{23} - c_{12}s_{23}s_{13}e^{i\delta} & c_{12}c_{23} - s_{12}s_{23}s_{13}e^{i\delta} & s_{23}c_{13} \\ s_{12}s_{23} - c_{12}c_{23}s_{13}e^{i\delta} & -c_{12}s_{23} - s_{12}c_{23}s_{13}e^{i\delta} & c_{23}c_{13} \end{pmatrix}, \tag{A.2}$$

where $c_{ij} = \cos\theta_{ij}$ and $s_{ij} = \sin\theta_{ij}$. We approximate it by using the relation $|V_{us}| \gg |V_{cb}| \gg |V_{ub}|$. By making an expansion of V in power of $\lambda \equiv V_{us} = 0.22$, we obtain

$$V = \begin{pmatrix} 1 - \lambda^2/2 & \lambda & A\lambda^3(\rho - i\eta) \\ -\lambda & 1 - \lambda^2/2 & A\lambda^2 \\ A\lambda^3(1 - \rho - i\eta) & -A\lambda^2 & 1 \end{pmatrix} + \mathcal{O}(\lambda^4), \tag{A.3}$$

with $A \sim 0.8$. This parameterization is called Wolfenstein parameterization [84].

The unitarity of V leads sereral relations between matrix elements of the matrix. One of them is

$$V_{ud}V_{ub}^* + V_{cd}V_{cb}^* + V_{td}V_{tb}^* = 0. \tag{A.4}$$

Considering $V_{ud}V_{ub}^* = A\lambda^3(\rho - i\eta)$, $V_{cd}V_{cb}^* = -A\lambda^3$ and $V_{td}V_{tb}^* = A\lambda^3(1 - \rho - i\eta)$, we can write a so-called unitarity triangle on the complex plane as shown in Fig. A.1. The angles of the triangle are defined as

$$\phi_1 = \beta \equiv \arg\left(-\frac{V_{cd}V_{cb}^*}{V_{td}V_{tb}^*}\right) \tag{A.5}$$
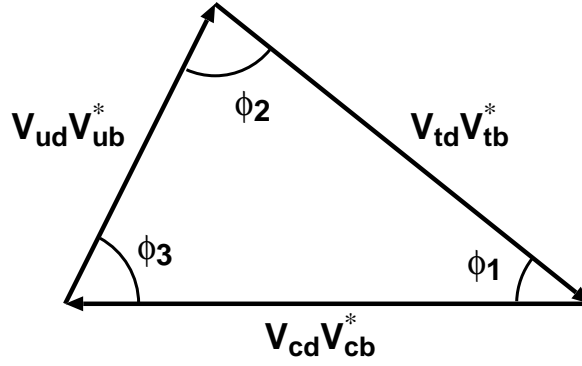
Figure A.1: Unitarity triangle.

$$\phi_2 = \alpha \equiv \arg\left(-\frac{V_{td}V_{tb}^*}{V_{ud}V_{ub}^*}\right) \tag{A.6}$$

$$\phi_3 = \gamma \equiv \arg\left(-\frac{V_{ud}V_{ub}^*}{V_{cd}V_{cb}^*}\right). \tag{A.7}$$

One of the main purposes of the Belle experiment is to determine the three angles of the unitarity triangle. $\sin 2\phi_1$ is measured using the time dependent asymmetry in the $b \to c\bar{c}s$ decays. The recent result from Belle [85] shows

$$\sin 2\phi_1 = 0.719 \pm 0.074 \pm 0.035. \tag{A.8}$$

The measurement of ϕ_2 and ϕ_3 is not easy, but is going on. If the sum of the three angles is not consistent with $180°$, it implies New Physics beyond the SM.

Appendix B

Global Decision Logic

We briefly describe the hardware of the GDL here. We also describe the trigger logic.

B.1   Hardware of the GDL

Figure B.1 shows the configuration of the GDL. It consists of four parts: Input Trigger Delay (ITD), Final Trigger Decision Logic (FTD or FTDL), Prescale and Mask (PSNM) and Timing Decision Logic (TMD or TMDL). The GDL receives up to 48 sub-trigger signals, generates 48 types of triggers by combining them,[1] and issues final triggers. Final trigger signals are issued 2.2 μs after the event crossing by using the TSC or ECL timing signal.
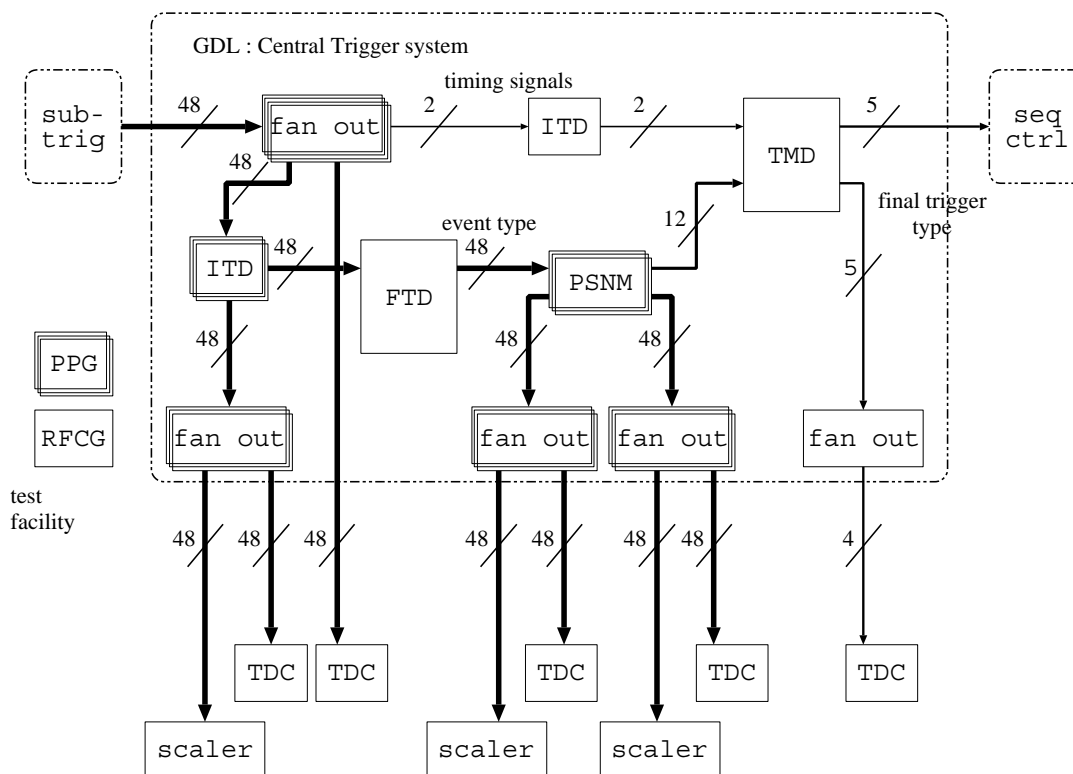

Figure B.1: Schematic design of the GDL.

---

[1]Since exp. 21, the number of the trigger types are increased from 48 to 64 by connecting two FTDL modules in parallel.

ITD receives sub-trigger signals and adjusts their timings. It consists of four ITD modules that are equipped with four Xilinx [86] FPGA (Field Programmable Gate Array) chips (XC3130PC68). They work with 32 MHz (64 MHz for timing signals) system clock made from the KEKB RF signals. Delays can be set from 0 to 31 in units of a clock cycle for each channel.

The outputs of ITD are fed into the FTDL module. The FTDL module performs logical arithmetics of the input signals in every 32 MHz clock cycle, and generates 48 types of trigger. The trigger logic is downloaded to a Xilinx CPLD (Complex Programmable Logic Device) chip (XC95108PQ160) on the module.

PSNM prescales or disables the outputs of the FTDL channel by channel. To implement PSNM logic, we used universal logic boards [87] with four Xilinx FPGA chips (XC3190APP175) developed for KEK PS E162 experiment [88]. One board can handle 16 channels, but we needed to connect two modules in series to provide a maximum prescale factor of 65025, due to the limitation of the logic resources. Therefore, since exp. 9, they have been replaced by similar universal logic boards developed for the readout electronics of ATLAS thin gap chamber [89]. This board have four Xilinx FPGA chips (XCS40PQ208) on it. Now one module can provide a maximum prescale factor of 262143. The 32 MHz system clock is used for PSNM modules.

TMDL decides the trigger timing. The TMDL module is operated with 64 MHz system clock to achieve better timing resolution. When TMDL receives a trigger signal from PSNM, it issues the final trigger 350 ns after the TSC timing signal. If the TSC timing signal is not available, the ECL timing signal is used. The TMDL logic is implemented in a Xilinx CPLD chip (XC95108PQ160).

B.2   Trigger Logic

Table B.1 lists the main trigger logics in the GDL. As described in Sec. 3.6.1, we prepare 4 kinds of triggers for hadronic events.

1. three-track trigger (`ffs_zt2` etc.),

2. energy trigger (`hie` etc.),

3. cluster trigger (`clst4` etc.),

4. combination of track, energy and cluster trigger (`hadron` etc.).

Because of the redundancy of the triggers, the L1 trigger is fully efficient for hadronic events. The redundancy is also useful to estimate the efficiency. For example, we can estimate the efficiency of the track trigger for hadronic events $\epsilon(\text{track})$ by

$$\epsilon(\text{track}) = \frac{N(\text{track \& energy})}{N(\text{energy})}, \tag{B.1}$$

where $N(\text{energy})$ is the number of hadronic events triggered by the energy trigger, and $N(\text{track \& energy})$ is the number of hadronic events triggered by both the track and energy trigger. We find that each hadron triggers provides more than 90% efficiency for $B\bar{B}$ events, and we expect more than 99% efficiency in total.

The hadron triggers are not always effective for τ and two-photon physics, because τ pair and two-photon events have less charged particles. These events are mostly triggered by two-track triggers. Tight conditions such as the opening angle are required in the two-track triggers to avoid the contribution of the background. Therefore, the L1 trigger is not fully efficient for the τ pair and two-photon events, so we usually need to estimate the L1 efficiency by MC.

Table B.1: Examples of the trigger logics in GDL. Main triggers for exp. 13 are listed with the definitions and prescale values (PSV). Logical "and", "or" and "not" are denoted by &, # and !, respectively.

Categories	Mnemonic	PSV	Definition
3-track	`ffs_zt2`	1	`(ncdr_short>2)&(ncdr_full>1)&(ntsc>1)` `&(ncdz>0)`
energy	`hie`	1	`e_high&!csi_bb&!csi_cosmic`
	`e_had`	1	`e_lum&!csi_bb`
cluster	`clst4`	1	`(nicl>3)&!csi_cosmic`
combination	`hadron`	1	`(ncdr_short>2)&e_low&(nicl>1)&(ntsc>0)`
2-track	`ff_zt2oc`	1	`(ncdr_full>1)&cdc_open&(ntsc>1)&(ncdz>0)` `&csi_timing&!csi_bb`
	`loe_fs_oz`	1	`e_low&(ncdr_short>1)&(ncdr_full>0)&cdc_open` `&(ncdz>0)&!csi_bb`
	`dimu_z`	40	`cdc_bb&(tsc_pat#(nicl>1))&(ncdz>0)`
	`clst2_oz`	2	`(nicl>1)&cdc_open&(ncdz>0)&!csi_bb`
muon	`klm_opn`	1	`cdc_open&(klm_brl#klm_fwd#klm_bwd)`
Bhabha	`csi_bhabha`	50	`csi_bb`
	`csi_lum_e`	50	`e_lum`
	`brl_bhabha`	10	`csi_brlbb`
2 photon	`two_photon`	1	`efc_tag&(ncdr_short>1)&(ncdr_full>0)`
	`efc`	3	`efc_tag&(nicl>1)`
$\gamma\phi$	`gphi`	2	`e_lum&(ncdr_short>1)&!cdc_open&!csi_fabbb`
$\gamma\gamma$	`brl_2gamma`	20	`csi_brlbb&!cdc_open`
random	`random`	42	`random`
	`revol`	200000	`revolution`

The other triggers mainly collect events such as Bhabha events, which are useful to the detector calibration and luminosity measurement. These triggers are often prescaled in order to reduce the trigger rate.

Appendix C

Supplements to the $B^+ \to K^+\pi^-\pi^+\gamma$ analysis

In this appendix, we describe the two topics that are omitted in Chapter 6. One is the determination of the ratio of the two MC used in the determination of the PDFs for $B^+ \to K^{*0}\pi^+\gamma$ and $B^+ \to K\rho^+\gamma$. The other is the determination of the $M_{K\pi}$ and $M_{\pi\pi}$ PDFs from MC.

C.1 MC for $B^+ \to K^{*0}\pi^+\gamma$ and $B^+ \to K\rho^+\gamma$

As described in Sec. 6.2.2, We use a mixture of $B^+ \to K_1(1400)^+\gamma \to K^*\pi\gamma$ MC and $B^+ \to K*(1680)^+\gamma \to K^*\pi\gamma$ MC for the determination of the PDFs of the $B^+ \to K^{*0}\pi^+\gamma$ component. The ratio of the mixture is determined from the data M_{K_X} distribution after applying the K^* mass cut.

   Figure C.1 (c) shows M_{K_X} distribution after applying the K^* mass cut. We estimate the M_{K_X} distribution for the $q\bar{q}$ background using the ΔE sideband and the distributions for the $B\bar{B}$ background and the $b \to s\gamma$ cross feed from MC. The normalization of the distribution for $q\bar{q}$ is calculated using the number of $q\bar{q}$ events in the signal region obtained from the M_{bc} fit shown in Fig. C.1 (a), where the signal yield is found to be $38.6^{+8.0}_{-7.3}{}^{+2.2}_{-0.5}$. The background-subtracted $M_{K\pi\pi}$ distribution are shown in Fig. C.1 (e). To determine the ratio of two MCs, we fit the distribution with a sum of MC histograms floating the total normalization and the ratio. The result is overlaid in the figure. We find that the data $M_{K\pi\pi}$ distribution is closest to a mixture of the two MC samples when we choose the fraction of $B^+ \to K_1(1400)^+\gamma \to K^*\pi\gamma$ MC component to be 0.74 ± 0.14.

   Likewise, we use a mixture of $B^+ \to K_1(1270)^+\gamma \to K\rho\gamma$ and $B^+ \to K^*(1680)^+\gamma \to K\rho\gamma$ MC for the determination of PDFs of the $B^+ \to K\rho^-\gamma$ component. The M_{bc} and M_{K_X} distributions after applying the ρ mass cut are shown in Fig. C.1 (b), (d) and (f). We find the signal yield to be $18.9^{+7.5}_{-6.9}{}^{+2.0}_{-0.5}$. By fitting the data $M_{K\pi\pi}$ distribution, we set the fraction of $B^+ \to K_1(1270)^+\gamma \to K\rho\gamma$ to be 0.68 ± 0.17.

C.2 Determination of the PDFs for $M_{K\pi}$ and $M_{\pi\pi}$

As described in Sec. 6.2.3, the $M_{K\pi}$ PDFs are determined from MC except for the $q\bar{q}$ component. The MC $M_{K\pi}$ distributions are shown in Fig. C.2. The distribution for $B^+ \to K^{*0}\pi^+\gamma$ is fitted with a non-relativistic Breit-Wigner function, where the fit result is overlaid in Fig. C.2 (a). As a cross check, we also fit distributions obtained from MC in which the fraction of the mixture of
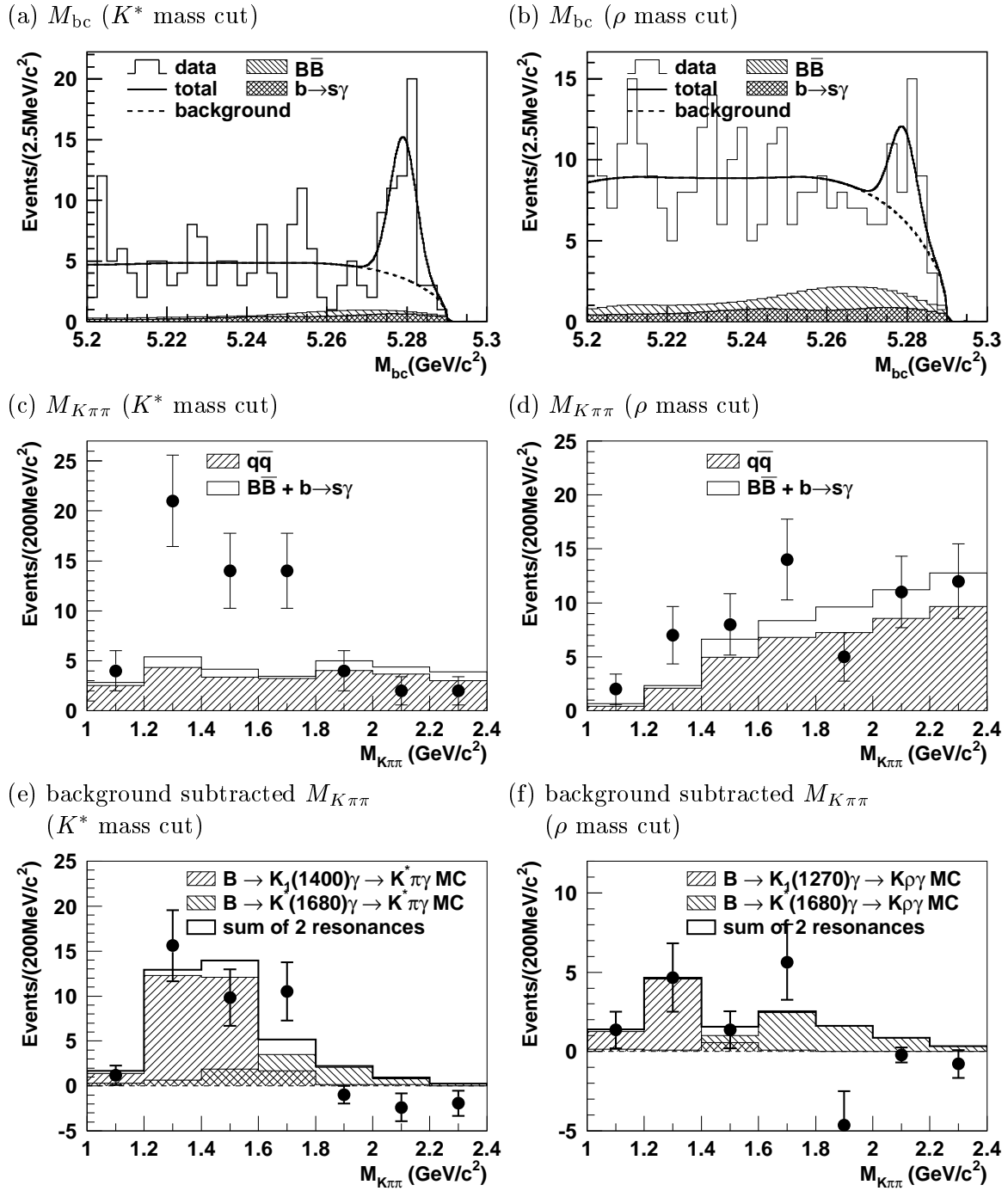
(a) M_{bc} (K^* mass cut)

(b) M_{bc} (ρ mass cut)

(c) $M_{K\pi\pi}$ (K^* mass cut)

(d) $M_{K\pi\pi}$ (ρ mass cut)

(e) background subtracted $M_{K\pi\pi}$
(K^* mass cut)

(f) background subtracted $M_{K\pi\pi}$
(ρ mass cut)

Figure C.1: (a) (b) M_{bc}, (c) (d) $M_{K\pi\pi}$ and (e) (f) background subtracted $M_{K\pi\pi}$ distributions after applying the K^* mass cut or the ρ mass cut. In (e) and (f), two MC histograms fitted to $M_{K\pi\pi}$ distributions are overlaid.

the two resonances in $B^+ \to K^{*0}\pi^+\gamma$ is varied by $\pm 1\sigma$, but the fit results are not shown because the differences from the original one is very small.

For the other components except the $B\bar{B}$ background component, we fit the distributions with a sum of a fourth order polynomial and a Gaussian (Fig. C.2). The Gaussian is added only to improve the fit. In the case of the $B^+ \to K^+\rho^0\gamma$ component, we fit the distributions from MC in which the fraction of the mixture of the two resonances is varied by $\pm 1\sigma$ as we do for the $B^+ \to K^{*0}\pi^+\gamma$ component. The fit results are overlaid in the figure by dashed and dotted curves. For the non-resonant $B^+ \to K^+\pi^-\pi^+\gamma$ component, the distribution from MC with phase space decay distribution of $K_1(1400)$ is used as a cross check, and the fit result is overlaid in the figure with a dashed curve. The dashed and dotted curves in Fig. C.2 (f) are the fit result from inclusive $b \to s\gamma$ MC with different m_b values. The distribution for $B\bar{B}$ is fitted to a simple fourth order polynomial.

The way to determine $M_{\pi\pi}$ PDFs are the same as that for $M_{K\pi}$ PDFs, except that the $M_{\pi\pi}$ distribution for $B^+ \to K^+\rho^0\gamma$ is fitted with a Breit-Wigner function and that the distribution for $B^+ \to K^{*0}\pi^+\gamma$ is fitted with a sum of a fourth order polynomial and a Gaussian. The distributions and fit results are shown in Fig. C.3.

In the distribution for $B^+ \to K^+\rho^0\gamma$, we can see a tail in the lower side of the ρ mass peak. This is due to the small phase space in the decay $K_1(1270) \to K\rho$ included in the MC. In order to evaluate possible contribution of the descripancy of the PDF in the tail part, the $M_{\pi\pi}$ distribution for $B^+ \to K^+\rho^0\gamma$ is also fitted with a sum of a fourth order polynomial and a Gaussian as shown in Fig. C.3 (b). This PDF is used as a cross check.
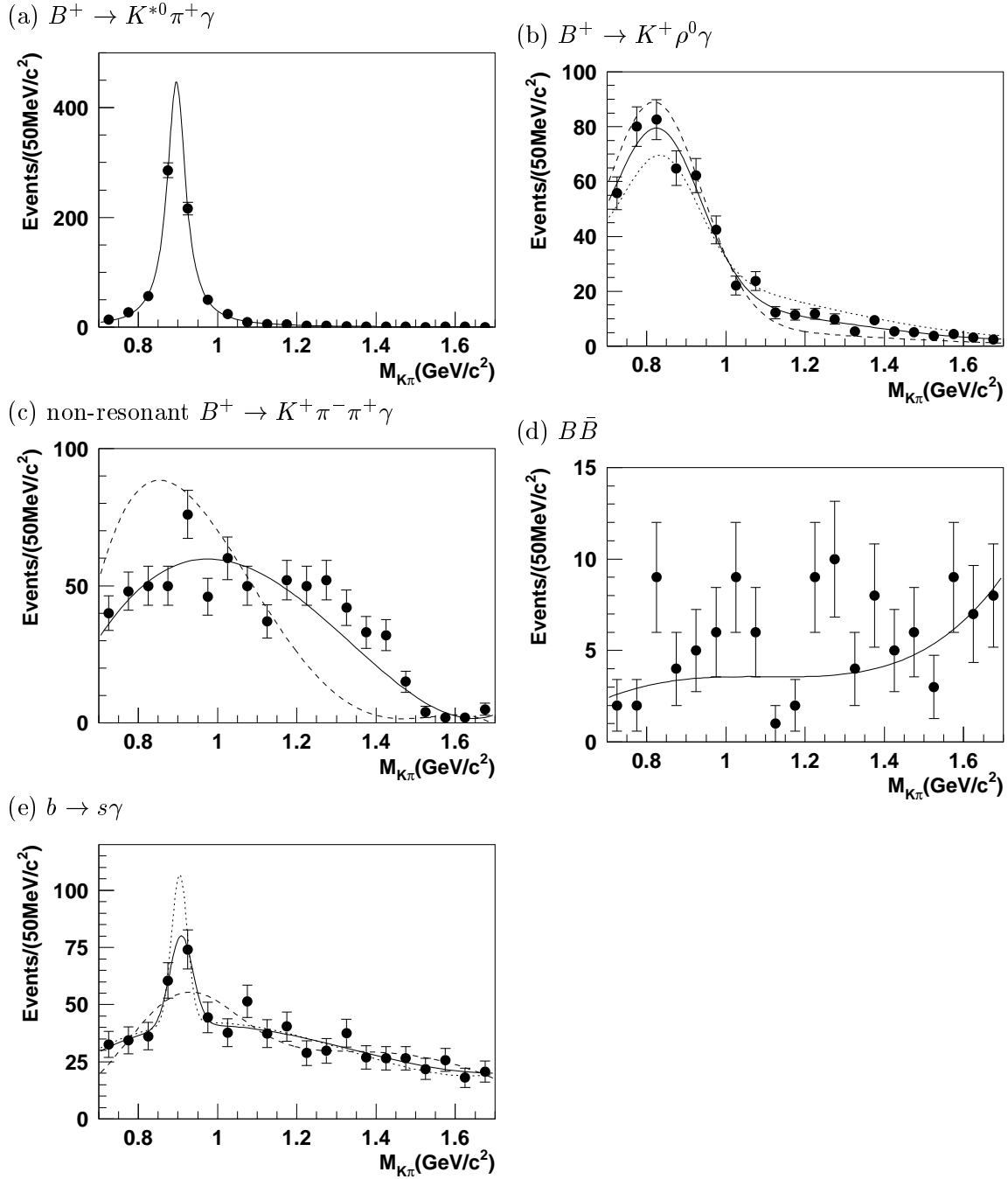
(a) $B^+ \to K^{*0}\pi^+\gamma$

(b) $B^+ \to K^+\rho^0\gamma$

(c) non-resonant $B^+ \to K^+\pi^-\pi^+\gamma$

(d) $B\bar{B}$

(e) $b \to s\gamma$

Figure C.2: $M_{K\pi}$ distributions (point) and fit results (solid curves) for (a) $B^+ \to K^{*0}\pi^+\gamma$ MC, (b) $B^+ \to K^+\rho^0\gamma$ MC, (c) non-resonant $B^+ \to K^+\pi^-\pi^+\gamma$ MC, (d) $B\bar{B}$ MC and (e) $b \to s\gamma$ cross feed. Dashed (dotted) curves show the fit results from different MC samples (see the text for details).
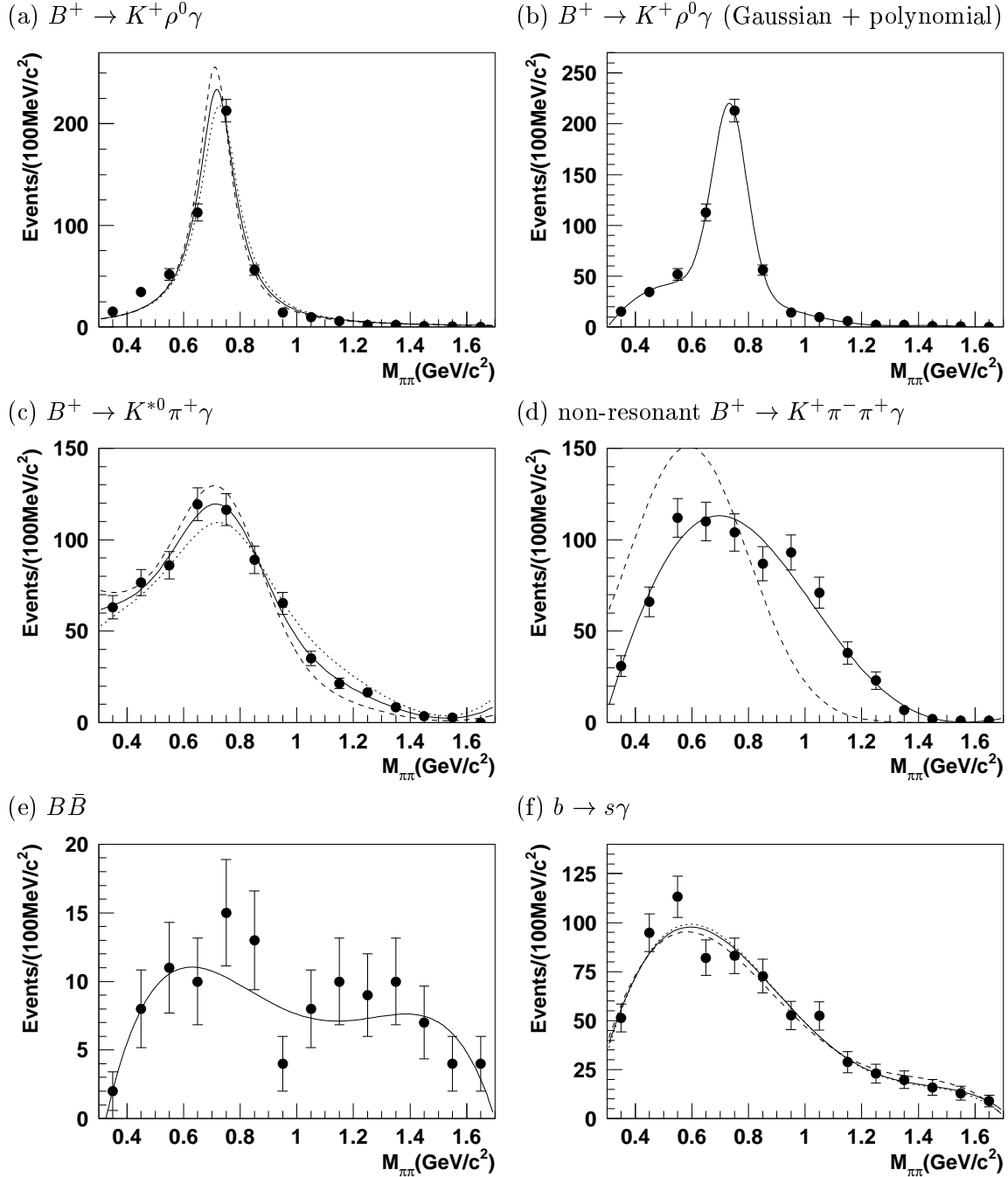
(a) $B^+ \to K^+\rho^0\gamma$

(b) $B^+ \to K^+\rho^0\gamma$ (Gaussian + polynomial)

(c) $B^+ \to K^{*0}\pi^+\gamma$

(d) non-resonant $B^+ \to K^+\pi^-\pi^+\gamma$

(e) $B\bar{B}$

(f) $b \to s\gamma$

Figure C.3: $M_{\pi\pi}$ distributions (point) and fit results (solid curves) for (a) (b) $B^+ \to K^+\rho^0\gamma$ MC, (c) $B^+ \to K^{*0}\pi^+\gamma$ MC, (d) $B^+ \to K^+\pi^-\pi^+\gamma$ N.R. MC, (e) $B\bar{B}$ MC and (f) $b \to s\gamma$ cross feed. In (a), the distribution is fitted to a Breit-Wigner function, while the distribution is fitted to a sum of a fourth order polynomial and a Gaussian in (b). Dashed (dotted) curves show the fit results from different MC samples (see the text for details).

Bibliography

[1] S. Nishida et al. (Belle Collaboration), Phys. Rev. Lett. **89**, 231801 (2002).

[2] M. Gronau and D. Pirjol, Phys. Rev. **D66**, 054008 (2002).

[3] A. J. Buras and R. Fleischer, Adv. Ser. Direct. High Energy Phys. **15**, 65 (1998).

[4] H. Albrecht et al. (ARGUS Collaboration), Phys. Lett. **B318**, 397 (1993).

[5] B. Barish et al. (CLEO Collaboration), Phys. Rev. Lett. **76**, 1570 (1996).

[6] K. Hagiwara et al. (Particle Data Group), Phys. Rev. **D66**, 010001 (2002).

[7] K. Abe et al. (Belle Collaboration), Phys. Lett. **B547**, 181 (2002).

[8] A. J. Buras, M. Misiak, M. Munz, and S. Pokorski, Nucl. Phys. **B424**, 374 (1994).

[9] A. J. Buras, A. Czarnecki, M. Misiak, and J. Urban, Nucl. Phys. **B631**, 219 (2002).

[10] S. Chen et al. (CLEO Collaboration), Phys. Rev. Lett. **87**, 251807 (2001).

[11] R. Barate et al. (ALEPH Collaboration), Phys. Lett. **B429**, 169 (1998).

[12] K. Abe et al. (Belle Collaboration), Phys. Lett. **B511**, 151 (2001).

[13] T. Sjöstrand, Comput. Phys. Commun. **82**, 74 (1994).

[14] R. Ammar et al. (CLEO Collaboration), Phys. Rev. Lett. **71**, 674 (1993).

[15] T. E. Coan et al. (CLEO Collaboration), Phys. Rev. Lett. **84**, 5283 (2000).

[16] B. Aubert et al. (BABAR Collaboration), Phys. Rev. Lett. **88**, 101805 (2002).

[17] Y. Ushiroda (Belle Collaboration), in *BCP4 2001 International Workshop on B physics and CP violation*, edited by T. Ohshima and A. I. Sanda (World Scientific, 2001), pp. 71–74, `hep-ex/0104045`.

[18] T. Altomari, Phys. Rev. **D37**, 677 (1988).

[19] A. Ali, T. Ohl, and T. Mannel, Phys. Lett. **B298**, 195 (1993).

[20] S. Veseli and M. G. Olsson, Phys. Lett. **B367**, 309 (1996).

[21] D. Ebert, R. N. Faustov, V. O. Galkin, and H. Toki, Phys. Rev. **D64**, 054001 (2001).

[22] A. S. Safir, Eur. Phys. J. direct **C15**, 1 (2001).

[23] S. Ahmad and Riazuddin, Phys. Rev. **D65**, 074018 (2002).

[24] H. Albrecht et al. (ARGUS Collaboration), Phys. Lett. **B210**, 258 (1988).

[25] H. Albrecht et al. (ARGUS Collaboration), Phys. Lett. **B229**, 304 (1989).

[26] D. Atwood, M. Gronau, and A. Soni, Phys. Rev. Lett. **79**, 185 (1997).

[27] D. Melikhov, N. Nikitin, and S. Simula, Phys. Lett. **B442**, 381 (1998).

[28] Y. Grossman and D. Pirjol, JHEP **06**, 029 (2000).

[29] J. H. Christenson, J. W. Cronin, V. L. Fitch, and R. Turlay, Phys. Rev. Lett. **13**, 138 (1964).

[30] M. Kobayashi and T. Maskawa, Prog. Theor. Phys. **49**, 652 (1973).

[31] A. B. Carter and A. I. Sanda, Phys. Rev. Lett. **45**, 952 (1980); A. B. Carter and A. I. Sanda, Phys. Rev. **D23**, 1567 (1981); I. I. Bigi and A. I. Sanda, Nucl. Phys. **B193**, 85 (1981).

[32] S. Kurokawa et al. (B-Factory Accelerator Task Force), *Accelerator design of the KEK B-Factory*, KEK Report 90-24 (1991).

[33] N. Toge et al., *KEKB B-Factory design report*, KEK Report 95-7 (1995).

[34] M. T. Cheng et al. (Belle Collaboration), *Letter of intent for a study of CP violation in B meson decays*, KEK Report 94-2 (1994).

[35] M. T. Cheng et al. (Belle Collaboration), *A study of CP violation in B meson decays: Technical design report*, KEK Report 95-1 (1995).

[36] A. Abashian et al. (Belle Collaboration), Nucl. Instrum. Meth. **A479**, 117 (2002).

[37] http://www.lns.cornell.edu/public/CLEO/.

[38] http://www.slac.stanford.edu/BFROOT/.

[39] http://belle.kek.jp/.

[40] http://www-hera-b.desy.de/.

[41] http://www-btev.fnal.gov/.

[42] http://lhcb.web.cern.ch/lhcb/.

[43] S. W. Herb et al., Phys. Rev. Lett. **39**, 252 (1977).

[44] J. P. Alexander et al. (CLEO Collaboration), Phys. Rev. Lett. **86**, 2737 (2001).

[45] K. Akai et al., *RF systems for the KEK B-Factory*, KEK Preprint 2001-157C (2001), to be appeared in Nucl. Instrum. Meth. A.

[46] K. Akai et al., *Commissioning of KEKB*, KEK Preprint 2001-157J (2001), to be appeared in Nucl. Instrum. Meth. A.

[47] G. Alimonti et al. (Belle Collaboration), Nucl. Instrum. Meth. **A453**, 71 (2000).

[48] H. Hirano et al., Nucl. Instrum. Meth. **A455**, 294 (2000).

[49] T. Iijima et al., Nucl. Instrum. Meth. **A453**, 321 (2000).

[50] H. Kichimi et al., Nucl. Instrum. Meth. **A453**, 315 (2000).

[51] O. Toker et al., Nucl. Instrum. Meth. **A340**, 572 (1994).

[52] M. Akatsu et al., Nucl. Instrum. Meth. **A454**, 322 (2000).

[53] H. Ikeda et al., Nucl. Instrum. Meth. **A441**, 401 (2000).

[54] K. Hanagaki et al., Nucl. Instrum. Meth. **A485**, 490 (2002).

[55] V. Zhilich et al., *Online luminosity measurements with CsI calorimeter at the Belle detector*, Belle Note 465 (2001).

[56] M. Z. Wang et al., Nucl. Instrum. Meth. **A455**, 319 (2000).

[57] Y. Ushiroda et al., Nucl. Instrum. Meth. **A438**, 460 (1999).

[58] M. Tomoto et al., Nucl. Instrum. Meth. **A447**, 416 (2000).

[59] H. O. Kim and B. G. Cheon, *Simulation study of new bhabha trigger schemes*, Belle Note 477 (2002).

[60] Trigger efficiencies are given in S. Nishida et al., Belle Note 350 (exp. 7); 381 (exp. 9); 423 (exp. 11); 459 (exp. 13); 504 (exp. 15); 520 (exp. 17); 548 (exp. 19); 584 (exp. 21 and 23).

[61] M. Nakao et al., IEEE Trans. Nucl. Sci. **47**, 56 (2000).

[62] S. Y. Suzuki et al., IEEE Trans. Nucl. Sci. **47**, 61 (2000).

[63] M. Nakao et al., IEEE Trans. Nucl. Sci. **48**, 2385 (2001).

[64] K. Hanagaki, M. Hazumi, and H. Kakuno, *Level 4 software trigger at BELLE*, Belle Note 299 (2000).

[65] QQ – The CLEO Event Generator, `http://www.lns.cornell.edu/public/CLEO/soft/QQ`.

[66] *GEANT – detector description and simulation tool* (1993), CERN Program Library Long Writeup W5013.

[67] D. E. Groom et al. (Particle Data Group), Eur. Phys. J. **C15** (2000).

[68] K. Abe et al. (Belle Collaboration), Phys. Rev. **D65**, 092005 (2002).

[69] A. L. Kagan and M. Neubert, Eur. Phys. J. **C7**, 5 (1999).

[70] B. Casey, *HadronB*, Belle Note 390 (2001).

[71] C. S. Park, *Measurement of inclusive production of neutral pions from $\Upsilon(4S)$ decays*, Belle Note 339 (2001).

[72] T. Matsumoto, *Measurement of $\sqrt{s}$ from full reconstructed B decays at $\Upsilon(4S)$ resonance*, Belle Note 418 (2001).

[73] G. C. Fox and S. Wolfram, Phys. Rev. Lett. **41**, 1581 (1978).

[74] R. A. Fisher, Annals Eugen. **7**, 179 (1936).

[75] K. Abe et al. (Belle Collaboration), Phys. Rev. Lett. **88**, 052002 (2002).

[76] E. D. Bloom and C. Peck, Ann. Rev. Nucl. Part. Sci. **33**, 143 (1983).

[77] S. Kopp et al. (CLEO Collaboration), Phys. Rev. **D63**, 092001 (2001).

[78] J. M. Blat and V. F. Weisskopf, *Theoretical Nuclear Physics* (New York Wiley, 1952).

[79] H. W. Kim et al., *Study of high energy photon detection efficiency using radiative bhabha*, Belle Note 499 (2001).

[80] J. W. Nam, *Track finding efficiency study using η sample*, Belle Note 434 (2001).

[81] M. Nakao et al., *Study of radiative decay $B \to K^* \gamma$ with Belle*, Belle Note 333 (2000).

[82] G. J. Feldman and R. D. Cousins, Phys. Rev. **D57**, 3873 (1998).

[83] L.-L. Chau and W.-Y. Keung, Phys. Rev. Lett. **53**, 1802 (1984).

[84] L. Wolfenstein, Phys. Rev. Lett. **51**, 1945 (1983).

[85] K. Abe et al. (Belle Collaboration), Phys. Rev. **D66**, 071102 (2002).

[86] `http://www.xilinx.com/`.

[87] M. Suehiro et al., in *Proceedings of the 2nd International Data Acquisition Workshop on Networked Data Acquisition Systems*, edited by M. Nomachi and S. Ajimura (World Scientific, 1997), pp. 281–286.

[88] T. Nomura et al., Phys. Lett. **B408**, 445 (1997).

[89] H. Sakamoto et al., Nucl. Instrum. Meth. **A453**, 430 (2000).